Chromospheric Macrospicules: Connection to the Solar Dynamo?

The University Of Sheffield.

Tamás Sándor Kiss

School of Mathematics and Statistics

University of Sheffield

Under the supervision of

Professor Robertus Erdélyi

This dissertation is submitted for the degree of

Doctor of Philosophy

2019

Declaration of Authorship

I hereby declare that except where specific reference is made to the work of others, the contents of this dissertation are original and have not been submitted in whole or in part for consideration for any other degree or qualification in this, or any other university. This dissertation is my own work and contains nothing which is the outcome of work done in collaboration with others, except as specified in the text and Acknowledgements. This dissertation contains fewer word than 80,000 words including appendices, bibliography, footnotes, tables and equations.

Abstract

Introduction: This study aims to provide further evidence for the potential influence of the global solar magnetic field on localized chromospheric jets, the macrospicules (MS). Macrospicules are localized small-scale jet-like phenomena in the solar atmosphere, which have the potential to transport a considerable amount of momentum and energy from the lower solar atmospheric regions to the transition region and the low corona.

Methods: Using state-of-the-art spatial and temporal resolution observations yielded by the *Atmospheric Imaging Assembly* of *Solar Dynamics Observatory*, we constructed a database covering a seven-year-long period, containing 358 macrospicules that occurred between June 2010 and June 2017, detected at 30.4 nm wavelength. The results are based on the long-term variation of the height, length, average speed, and width of MS in coronal holes [CH-MS] and in Quiet Sun [QS-MS] areas both in the northern and southern hemispheres of the Sun.

Results: Three of the five timesets of the investigated physical properties of MS show a clear long-term temporal variation. Wavelet analyses of the temporal variation of maximum length, maximum area, and average velocity reveal a strong pattern of periodicities at around 2 years. A comparison with solar activity proxies also uncovers that the minima and maxima of quasi-biennial oscillations [QBOs] of MS properties and solar activity proxies occur at around the same epoch. Spatially, the characteristic values of these parameters are found to be slightly greater for QS-MS than for CH-MS all around the solar disk. We have also discovered evidence towards supporting the hypothesis that there is a connection between the migration pattern of the formation cradle of MS and the nearly two-year-long oscillations. Furthermore, MS tend to exhibit parabolic motion, which indicates the strong effect of gravity. We have modelled this motion of MS in the atmosphere.

"So Say We All!"

- Battlestar Galactica

Acknowledgements

My publications

This Thesis based on the following referred publications:

1. **Kiss, T. S.**; Gyenge, N.; Erdélyi, R.; (2017); *Systematic Variations of Macrospicule Properties Observed by SDO/AIA over Half a Decade*; The Astrophysical Journal; Volume 835; Issue 1; Article ID 47; 10 pp.; ADS link

2. **Kiss, T. S.**; Gyenge, N.; Erdélyi, R.; (2018); *Quasi-biennial oscillations in the cross-correlation of properties of macrospicules*; Advances in Space Research; Volume 61; Issue 2; p 611 – 616; ADS link

3. **Kiss, T. S.**; Erdélyi, R.; (2018); *On Quasi-biennial Oscillations in Chromospheric Macrospicules and Their Potential Relation to the Global Solar Magnetic Field*; The Astrophysical Journal; Volume 857; Issue 2; Article ID 113; 9 pp.; ADS link

The following publication is not included on this Thesis:

1. Gyenge, N.; Singh, T.; **Kiss, T. S.**; Srivastava, A. K.; Erdélyi, R.; (2017); *Active Longitude and Coronal Mass Ejection Occurrences*; The Astrophysical Journal; Volume 838; Issue 1; Article ID 18; 10 pp.; ADS link

Contents

List of Figures

List of Tables

Chapter 1

Introduction

1.1 Structure of the Solar Corona

Even before the age of spacecraft, solar eclipses provided unique opportunities to look at the white and blurry structure around the covered solar disk, the solar atmosphere (Guillermier & Koutchmy, 1999). Regular observations of solar eclipses with dageuerrotypes, CCDs, or spectrographs led to the discovery of several unforeseen physical processes and features, such as the presence of helium in the spectra of the atmosphere of the Sun (Bray et al., 1991). The age of spacecraft led to the continuous observation of the Sun uninterrupted by the scattering of light inside the terrestrial atmosphere (Alexander & Acton, 2002).

The solar atmosphere could be divided into four domains: the photosphere, chromosphere, Transition Region and the corona. These domains, as a simplest assumption, form spherical layers with a horizontally quasi-homogeneous density distribution due to gravitational stratification. However, actual observations of the solar atmosphere indicate a multitude of inhomogeneities, which are driven dominantly by the magnetic field. A crucial parameter in the interpretation of physical processes in the solar atmosphere is the so-called plasma-β, which describes the ratio between the thermal pressure, p_{th}, and the magnetic pressure, p_{mag}:

$$\beta = \frac{p_{\text{th}}}{p_{\text{mag}}} = \frac{2\xi n_e k_B T_e}{B^2/8\pi} \approx 0.07 \xi n_9 T_6 / B_1^2, \tag{1.1}$$

where $\xi(=1)$ is the ionization fraction for the corona, $k_{\text{B}} = 1.38 \times$
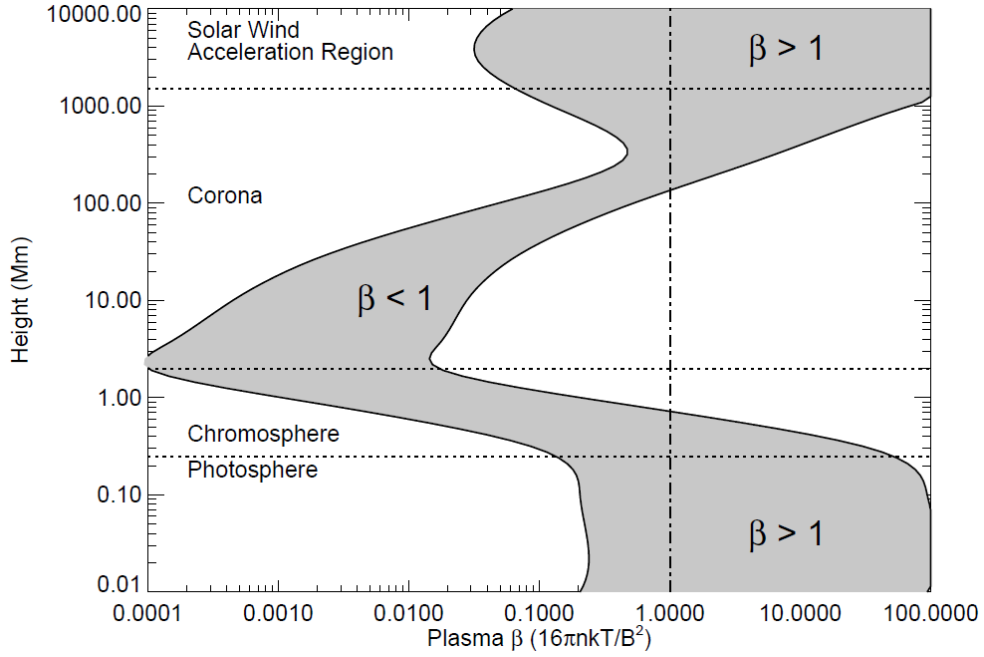
Figure 1.1: The distribution of plasma-β across the solar atmosphere. Image courtesy of Gary (2001).

10^{16} erg K^{-1} is the Boltzmann constant, $B_1 = B/10$ G is the magnetic field strength, $n_9 = n_e/10^9$ cm^3 is the electron density, and $T_6 = T/10^6$ K is the electron temperature.

The continuous variation of the plasma-β parameter across the solar atmosphere is illustrated in Figure 1.1. In the photosphere, which is considered as the surface of the Sun, the kinetic pressure of the plasma is higher than the magnetic pressure (i.e., $\beta \gg 1$). In the lower regions of the atmosphere, the magnetic field is more localised and often concentrated in flux tubes. Moving away radially from the solar surface, the kinetic pressure drops, which leads to the expansion of the magnetic flux tubes. In the upper corona, the magnetic field is relatively homogeneous and the plasma pressure is dominated by the magnetic pressure. Therefore, the plasma-β is less than unity. In resistive magnetohydrodynamics, the evolution of the magnetic field $\vec{B}$ is governed by the following equation:

$$\frac{\partial \vec{B}}{\partial t} = \nabla \times (\vec{v} \times \vec{B}) + \eta \nabla^2 \vec{B}, \tag{1.2}$$
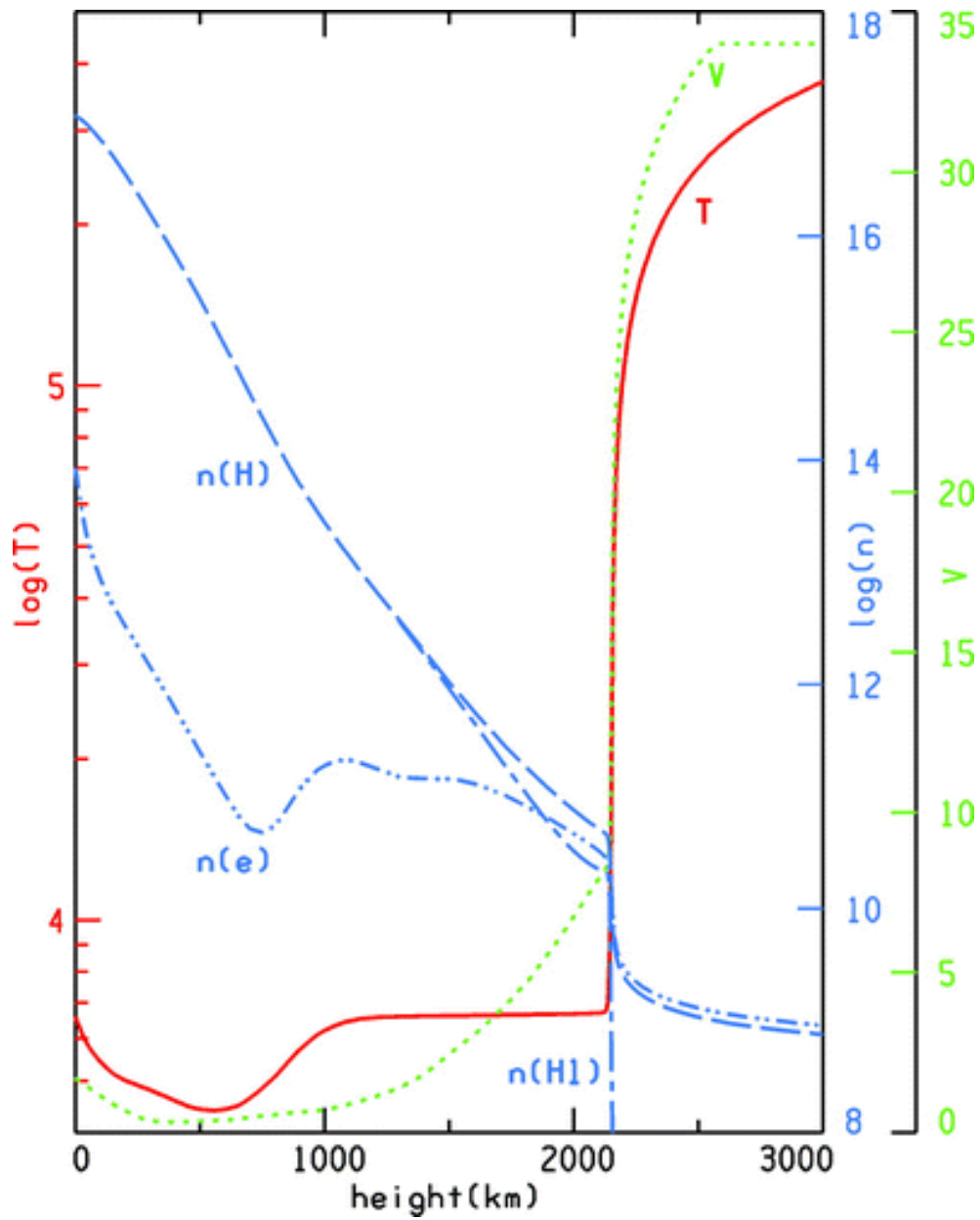
Figure 1.2: Model C7 variations with height of the temperature (in K) [red line], turbulent velocity (in km s^{-1}) [green dotted line], total hydrogen density [dashed blue line], neutral hydrogen density [blue dashed dotted line], and electron density (in cm^{-3}) [blue double dotted dashed line]. Image courtesy of Avrett & Loeser (2008).

where $\vec{v}$ is the velocity of the plasma and η is the magnetic diffusivity. The first term on the RHS determines the induction of the magnetic field, while the second term describes the diffusion. The dimensionless *magnetic Reynolds-number* R_m provides the ratio between the magnetic induction and the magnetic diffusion:

$$R_m = \frac{l_0 v_0}{\eta}, \tag{1.3}$$

where l_0 and v_0 are the typical length-scale and plasma speed, respectively. If $R_m \ll 1$, the coupling between the plasma flow and the magnetic field is weak, which is often the case for laboratory plasma. However, in the solar corona, the *magnetic Reynolds number* is much larger than unity ($R_m \approx 10^8 - 10^{12}$). Hence, according to *Alfvén's frozen-flux theorem*, the diffusion term is negligible in Equation 1.2. The plasma of the solar corona could be considered as a perfectly conducting medium, thus, it is referred to as the *ideal plasma* approximation. In ideal plasma flows: i) magnetic flux is conserved; and ii) magnetic field lines are conserved; and iii) magnetic topology is conserved. Hence, the plasma can only move alongside the *frozen-in* magnetic field line. If the flow is perpendicular to the *frozen-in* magnetic field, the field line pushes the plasma or the plasma drags the field lines. The structure of the magnetic field could be stretched and deformed by such flows, but its topology is not changed.

The density and the temperature are critical parameters in the description of the solar plasma. The distribution of these quantities in the atmosphere is also highly inhomogeneous due to magnetic field. Regarding the strength of the magnetic field, the electron density could vary in the range of $10^6 - 10^9$ cm^{-3} from high to low plasma-β regions in the upper atmosphere. The one-dimensional density and temperature structure of a gravitationally stratified vertical flux tube is displayed in Figure 1.2. The temperature slowly drops radially, and reaches a minimum value (called the temperature minimum) around a height of several hundred km above the solar surface. Above the temperature minimum, the temperature starts to increase inside the thin interface region of the Transition Region (TR) and reaches the magnitude of several million K in the solar corona. The density follows a similar trend: it decreases slowly in the lower atmosphere and undergoes a significant reduction in

the TR. In the chromosphere, the plasma is partially ionized, relatively cool and dense. Dynamic processes such as plasma flows, thermal conduction, and radiation heat up the chromosphere to temperatures higher than in the photosphere. The spectrum of this region is dominated by (mostly optically thick) absorption lines such as the Balmer series or Ca II H/K lines. In the corona, the plasma becomes fully ionzed, and the *plasma-β* becomes much smaller than unity. The spectrum of the solar corona is composed of optically thin ultraviolet and X-ray emission lines, such as the lines of the highly ionized iron. There is no sharp upper boundary for the solar corona, rather, it continuously fades into the solar wind and expands into the interplanetary space.

The question arises: how could the solar corona be heated to several million degrees, while the temperature of the solar surface is only 6000 K? What are the processes which drive up energy from the solar surface into the upper atmosphere to result in large temperatures? The so-called *coronal heating problem* is still an unresolved field of research. Assuming that the heating and the cooling processes present are only thermal conduction and radiative losses by ultraviolet emission, the solar corona should cool down within several hours (Aschwanden, 2004). Withbroe & Noyes (1977) calculated the energy requirement for heating several different magnetic, but spatially isolated structures: the required heating rate is proportional to the density squared. Furthermore, the assumption of hydrostatic equilibrium describes the height-dependence of the heating. This theory was underpinned by e.g. the analysis of 40 coronal loops observed by Aschwanden et al. (2000). Eruptive events, such as jets or flares, could transport a considerable amount of energy and momentum into the corona.

Coronal holes are the faintest regions of the solar corona, appearing as dark patches in the observations (Cranmer, 2009). In coronal holes, the low density, therefore collisionless, plasma flows along the open magnetic field lines and reaches the velocity of the fast solar wind (Saito 1958; Newkirk & Harvey 1968). In these regions, the temperature of the plasma is also lower (Zirin 1975; Centeno et al. 2008). The composition of coronal hole plasma is partially ionized, which shows more similarity to the photosphere rather than the corona (Feldman 1998; Feldman & Widing 2003). Coronal holes are observable both on-disk and on the limb. A

Figure 1.3: A schematic image showing the structure of the solar atmosphere. Image courtesy of Wedemeyer-Böhm et al. (2009).

precise estimate for the position of boundary of the coronal holes can be carried out using the He I 1083 nm absorption line triplet (Harvey et al. 1975; Harvey & Recely 2002). On-disk measurements of the magnetic field of coronal holes indicated a significant imbalance between the two polarities. Hence, coronal holes are relatively unipolar regions (Levine, 1982). Additionally, the rate of new magnetic flux emergence is lower inside the coronal holes, which also contributes to their lower emission compared to the surrounding solar environment (Rosner et al., 1978). The possible roots of coronal holes could be the so-called G-band bright points, which are signatures of concentrated, several hundred km wide, $1-2$ kG magnetic flux tubes between the photospheric granulation cells (Tsuneta et al., 2008a). These flux tubes start to expand in the lower chromosphere and merge with each other. The result is a nearly homogeneous network of magnetic field lines with a strength of approximately 100 G.

1.2   Solar Activity

Since the discovery of the variability of sunspots (for detailed information about sunspots and other solar activity proxies, see Section 2.4) by Schwabe (2004), solar activity is one of the most spectacular manifestations of the solar magnetism. The generation and evolution of the large-scale magnetic field of the Sun is the driving mechanism of solar activity. The evolution and effects of solar activity are still amongst the greatest questions of solar physics.

According to Waldmeier (1935), each solar cycle should be considered as an individual flare-up of several different polar activity proxies (such as sunspot number, sunspot area, etc.), which could temporally overlap with each other. For this reason, each cycle could be characterised separately. The simplest descriptors of the solar cycles are their amplitude and the epoch of their minima and their maxima (Waldmeier 1961; McKinnon & Waldmeier 1987). However, these parameters could be highly influenced by the input dataset, detection methods and the sometimes quiet stochastic variation of the solar activity. Furthermore, a minimum in solar activity does not represent the exact boundary between two solar cycles due to possibility of the presence of overlaps. Furthermore, overlapping turns the estimation of the length of the cycles into a challenging task (Eddy 1977; Wilson 1987). The mean length of solar cycles is around 131 months ($\approx$ 10.9 years) with a standard deviation of 14 months (Hathaway, 2012). The amplitude of the cycle strongly depends on the investigated solar activity proxy. A significant asymmetry was found by Waldmeier (1935, 1939) between the amplitude of the cycle and the temporal length of the rising phase (the time span between the epochs of the minima and the maxima at the beginning of the cycle). Nevertheless, the so-called Waldmeier effect is not independent from the investigated solar proxy, as it was stated by Dikpati et al. (2008).

By studying the magnetism of sunspots (Hale, 1908), a cyclic pattern was discovered inside individual sunspot groups (Hale et al., 1919). The polarity of leading sunspots is opposite to that of the following sunspots inside the same sunspot group and to the leading sunspots on the other hemisphere. At the beginning of the following solar cycle, the polarities become reversed alongside the polar fields (Babcock & Livingston 1958;
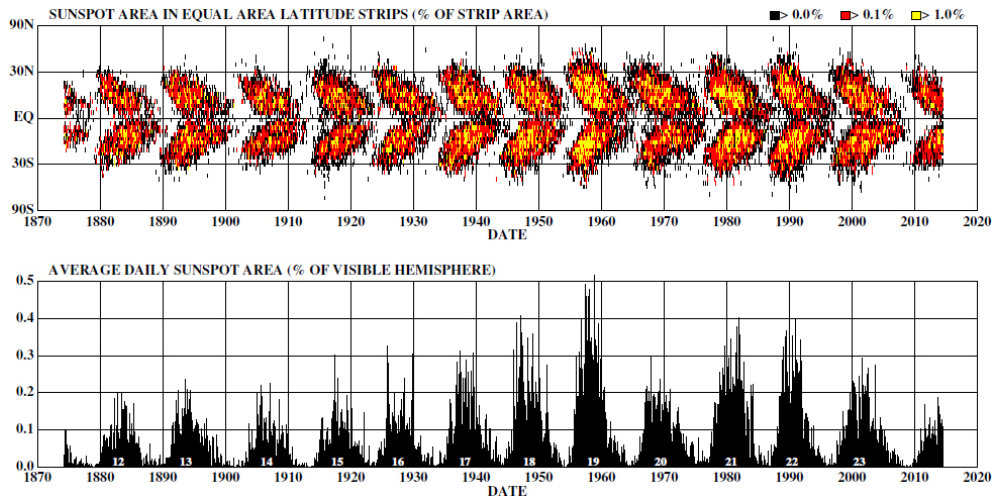
Figure 1.4: Top panel: temporal variation of the latitudinal appearance of sunspots since May 1874. The relative sunspot area within equal area latitude strips is illustrated with a colour coding in the top panel. Lower panel: the temporal variation of the sunspot area for the same time domain. Image courtesy of Hathaway (2012).

Babcock 1959). This behaviour is referred to "Hale's Polarity Law". The investigation of both the latitudinal and longitudinal positions of sunspots revealed their migration patterns throughout the solar cycle. Sunspots tend to appear nearly symmetrically in both hemispheres. In the early phase of each cycle, sunspots are formed at higher solar latitudes (over 30 deg). As the cycle progresses, the position of first appearance of sunspots drifts closer to the solar equator in both hemispheres. The appearance of sunspots on higher latitudes indicates the beginning of the new solar cycle. However, the epoch of the solar minimum and the start of the new solar cycle may not be the adjacent. This pattern of sunspot appearance, as seen in the top panel of Figure 1.4, is widely known as the "Butterfly Diagram" (Maunder, 1904) or "Spörer's Law of Zones" (Maunder, 1903).

Between the previous Solar Cycle 23 and the current Solar Cycle 24, as of writing, the minimum reached an unusually long duration in comparison to prior cycles with nearly 60 spotless days (Sunspot Index and Long-term Solar Observations (SILSO) data/image, Royal Observatory of Belgium, Brussels). The value of the 13-month smoothed sunspot number decreased to 1.7 in December 2008. Since the minimum, the am-

plitude of Solar Cycle 24 remained quite low with a maximum sunspot area value of 81.9. The current cycle is characterised by a double peak maximum: a greater one in February 2014, a minor one in January 2013. Presently, Solar Cycle 24 is in its decaying phase and possibly reaching the minimum between Solar Cycle 24 and 25 around 2019–2020 (Howe et al., 2018).

In order to model the complex problem of the observed nature of solar activity, the so-called solar dynamo model was constructed. The theoretical consideration is based on an often simplified description of the physical system, which could be more or less physically realistic. Charbonneau (2010) summarises the simpler dynamo models and compares them to the observations.

In a review paper, Hathaway (2015) discusses the topic of solar activity in more detail.

1.3   Discovery of Macrospicules

The observations and the modelling of macrospicules (MS) reaches back for years. The first suggestion for the existence of such ejecta was discussed by Tousey (1972). Bohlin et al. (1975) reported the first observation of MS. MS were considered, as a first approach, clumps of Hα spicules during the analysis of data gathered during rocket flights in 1969. However, the two arcsec spatial resolution of the He II 30.4 nm line channel of the Naval Research Laboratory (NRL) slitless spectrograph on-board the *Skylab* mission (Tousey et al., 1973) unveiled the individual behaviour of these jets. Figure 1.5 demonstrates some examples of MS. The denomination "macrospicules" is rooted in the physical properties of the ejecta: MS could reach sizes several times longer than the observed height of Hα spicules. Furthermore, based on the spectral domain of observations, these jets could be separated into two classes: Hα macrospicules and Extreme UltraViolet (EUV) macrospicules.

During the *Skylab* observation campaign lasting 21 hours and 46 minutes, approximately 25 MS were identified in the polar coronal hole in the southern hemisphere. The sizes of these ejecta varied between 8 arcsec to 25 arcsec with the diameter of 5 – 15 arcsec. Therefore, the volume of an average MS could be 100 times larger than that of a typical Hα spicule. The lifetime of MS was around 30 ± 10 minutes, which is multiple times larger than the 3–7 minutes long existence of spicules (de Pontieu et al., 2007). Their velocity was estimated between 10 and 150 km s^{-1}, however, the error for this estimation was high due to the 4 ± 1 minutes temporal cadence of the spectrograph. During their evolution, MS rose up and fell back along their axis (or just simply faded away). However, no parabolic or arching trajectory was followed which would indicate the dominant impact of gravity on their trajectory. By comparing the observations in the He II line with other Transition Region (Ne VIII 46.5 nm) or coronal (Mg IX 36.8 nm) lines, MS do not tend to appear regularly in higher temperature lines. Therefore, the detected MS were possibly formed from plasma in the K temperature range of $5 - 12 \times 10^4$. This temperature domain is typical mainly in the upper chromosphere and the Transition Region. According to Kjeldseth Moe et al. (1975), MS had no counterparts in the Hα images. It is also important to note that no

correlations were found between the lifetime and the height of MS.

In order to study the similarities between the two phenomena, Moore et al. (1977) compared Hα MS in the measurements of the Big Bear Solar Observatory (BBSO) and EUV MS in the He II spectroheliograms from the Naval Research Laboratory (NRL) experiment on Skylab (Tousey et al., 1973). In the Hα movies of the BBSO, 45 MS were detected with a lifetime of 5 - 15 mins and a maximum height of 7 - 20 arcsec. The latitudinal distribution of Hα jets was the following: 19 jets were found to be 30° or closer to the solar equator; and 10 MS were identified between 30° and 60°; and 16 MS higher than 60°. Out of the 29 non-polar MS, 20 were formed away from coronal hole regions. In the observations of NRL, 28 jets were classified. After the co-alignment of MS in both of the Hα and EUV images, 22 jets were formed with less than 1° separation. In the remaining six cases, more EUV MS could be associated with the Hα MS than the other way around. In conclusion, the authors claimed that Hα MS were the Hα components of the EUV MS.

Withbroe et al. (1976) found two macrospicules in a polar coronal hole in the northern hemisphere. The observations were collected in six different spectral lines with the NRL on-board *Skylab* (Huber et al., 1974) in order to gather sufficient data for a multi-temperature modeling of the jets. The heights of these MS were between 10 Mm and 12 Mm with a density of 10^{10} cm^{-3}. The ballistics of the jets were investigated in the contour maps of the C III 97.7 nm line (with a formation temperature of 8×10^4 K, which is in the agreement with the statement of Bohlin et al. (1975)). The authors also studied the temporal variation of the height of both jets: along their central axis, MS tend to rise and fall back in a parabolic pattern. This indicates the influence of gravity alongside a dominant magnetic force, which keeps the plasma of the jet along the central axis. A multi-thermal model was constructed in a cylindrical coordinate-system: MS had a cool core with a temperature of 10^4 K. The plasma heated up radially to the 10^6 K temperature of the solar corona at the 3.6 Mm boundary of the jet. Furthermore, the needed energy to lift the estimated mass of the MS was 3×10^{26} ergs, which is twice as much as the energy required by spicules (Beckers, 1972).

Labonte (1979) observed MS in the He I multiplet at 587.6 nm, in the so-called He I D$_3$ line (Ramsey et al., 1975), and a detailed comparison
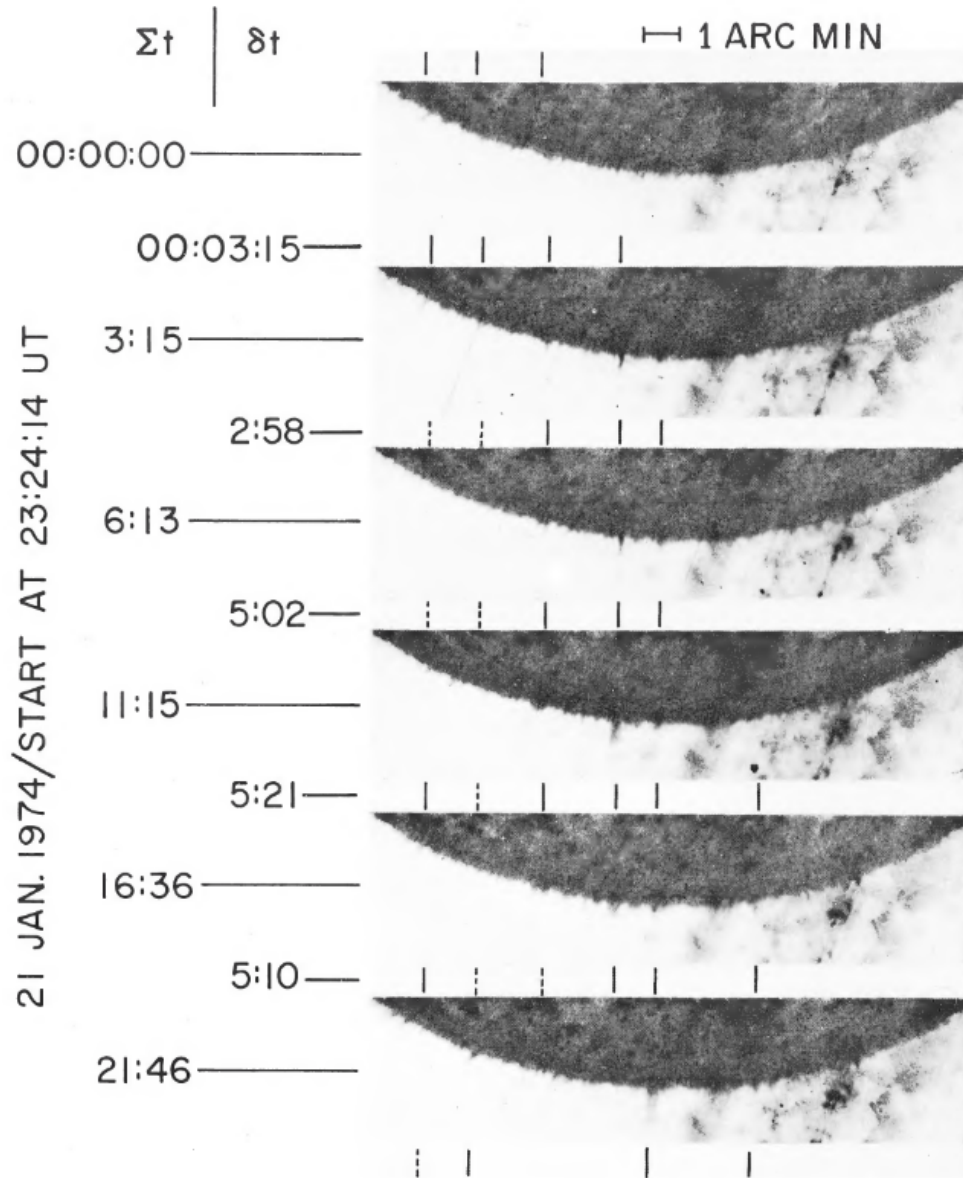
Figure 1.5: The first observation of macrospicules in the He II images inside a southern polar coronal hole. Vertical lines represent the position of the jets. Image courtesy of Bohlin et al. (1975).
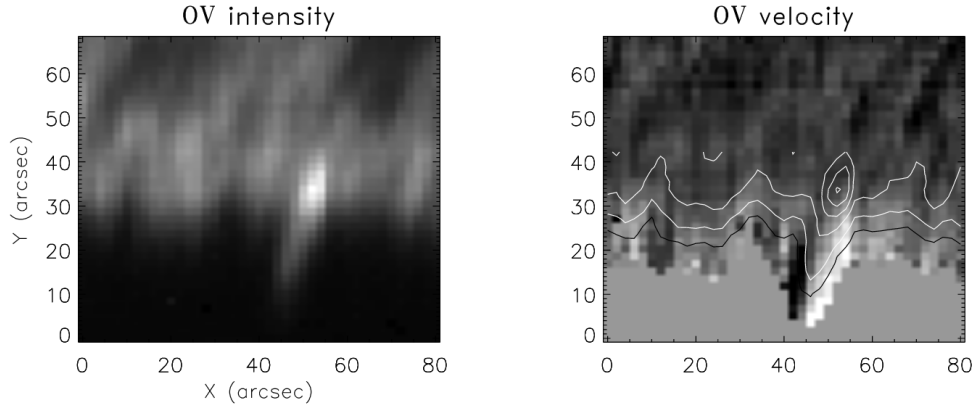
Figure 1.6: O V intensity (left-hand side) and velocity (right-hand side) maps about a macrospicule on the eastern solar equatorial limb on 09.06.1996. On the velocity map, black and white colour shading represents the pixels of blue- and red-shifted emission. Image courtesy of Pike & Mason (1998).

of Hα and D$_3$ MS was conducted. In the images of the 25 cm vacuum telescope at BBSO, 32 and 4 MS were identified in the Hα and D$_3$ lines, respectively. The D$_3$ jets seemed to have a somewhat larger height, width and lifetime: 20.7 arcsec, 3.3 arcsec and 16 minutes as compared to the 15.5 arcsec, 2.3 arcsec and 11 minutes, respectively. No significant correlation could be found between the physical distribution of the jets and their lifetime in the two spectral domains. Furthermore, the appearance rate of Hα MS was estimated according to their latitude as 4.9 ± 1.4 events per (hr 360°)$^{-1}$ for polar jets and 8.3 ± 2.0 events per (hr 360°)$^{-1}$ for ejecta close to the solar equator. Labonte (1979) suggested the source of this difference could be the larger number of active regions around the equator. Additionally, the author completed a study about the formation of MS on the solar disk and found an appearance rate of 2.8 ±0.9 events per hour.

Ten EUV macrospicules were classified in a polar coronal hole in the northern hemisphere by Dere et al. (1989). The observations were taken by the High Resolution Telescope and Spectrograph (HRTS) on-board the *Spacelab 2* mission. With the improved instrumentation, the entire evolution of the MS could now be detected in more detail in comparison with observations made by the previous *Skylab* mission. The raw observations were the convolution of the solar continuum formed mainly

between the temperature minimum and the Transition Region in the 0.2 nm spectral domain around the C IV 154.8 nm line. The length of these jets varied between 5 arcsec and 23 arcsec with an average of 12 arcsec, but no outstandingly large MS were detected, as Withbroe et al. (1976) reported. The measured width of the jets was around 6 ± 3 arcsec. Dere et al. (1989) detected an upflow speed of 20 - 50 km s^{-1}, which is lower than the speed found in the previous studies due to the lower temporal resolution of HRTS. However, the authors stated that the tilt-angles between the central axis of the jets and the solar limb were not constant.

The first radio observations of macrospicules were reported by Habbal & Gonzalez (1991) using detections of the Very Large Array (VLA). These jets were identified in groups in both the northern and southern polar coronal hole regions mainly at 4.8 GHz, and less significantly at 8.5 and 15 GHz. The physical extents of these ejecta corresponded to the previous observations in the literature: 15 - 45 arcsec of height and 10 - 25 arcsec width. The separation of the jets inside the groups was 30 to 60 arcsec, which indicates a common underlying physical source for their evolution (as was shown for Hα and EUV MS by Dere et al. (1989)). The position of the jets was found to be identical with the ones found in the EUV measurements when the radio measurements were overlayed with the observations of the Kitt Peak in He I 1083 nm line (it is important to note that this line is useful to map the structure of coronal holes (Andretta & Jones, 1997)). The radio measurements provided further evidence for the model of the multi-thermal nature of MS: they seemed to be composed of a denser (10^{10} cm^{-3}) but cooler ($4 - 8 \times 10^3$ K) central part and a thin, hotter (10^5 K) but less dense (10^9 cm^{-3}) sheath. These values were almost identical to those discussed by Withbroe et al. (1976). The authors provided a physical explanation for the evolution of MS: the ballooning and pinching-off effect. Macrospicules are driven by the released energy of reconnection between the predominantly existing open magnetic field of the coronal hole and the evolving magnetic bright point. The pinching-off leads to the acceleration of the plasma blob, which was observed in the 4.8 GHz images as macrospicules.

The entire evolution and formation mechanism of three MS were studied by Karovska & Habbal (1994). The jets were detected inside a northern polar coronal hole in the C III spectral line with the Harvard EUV
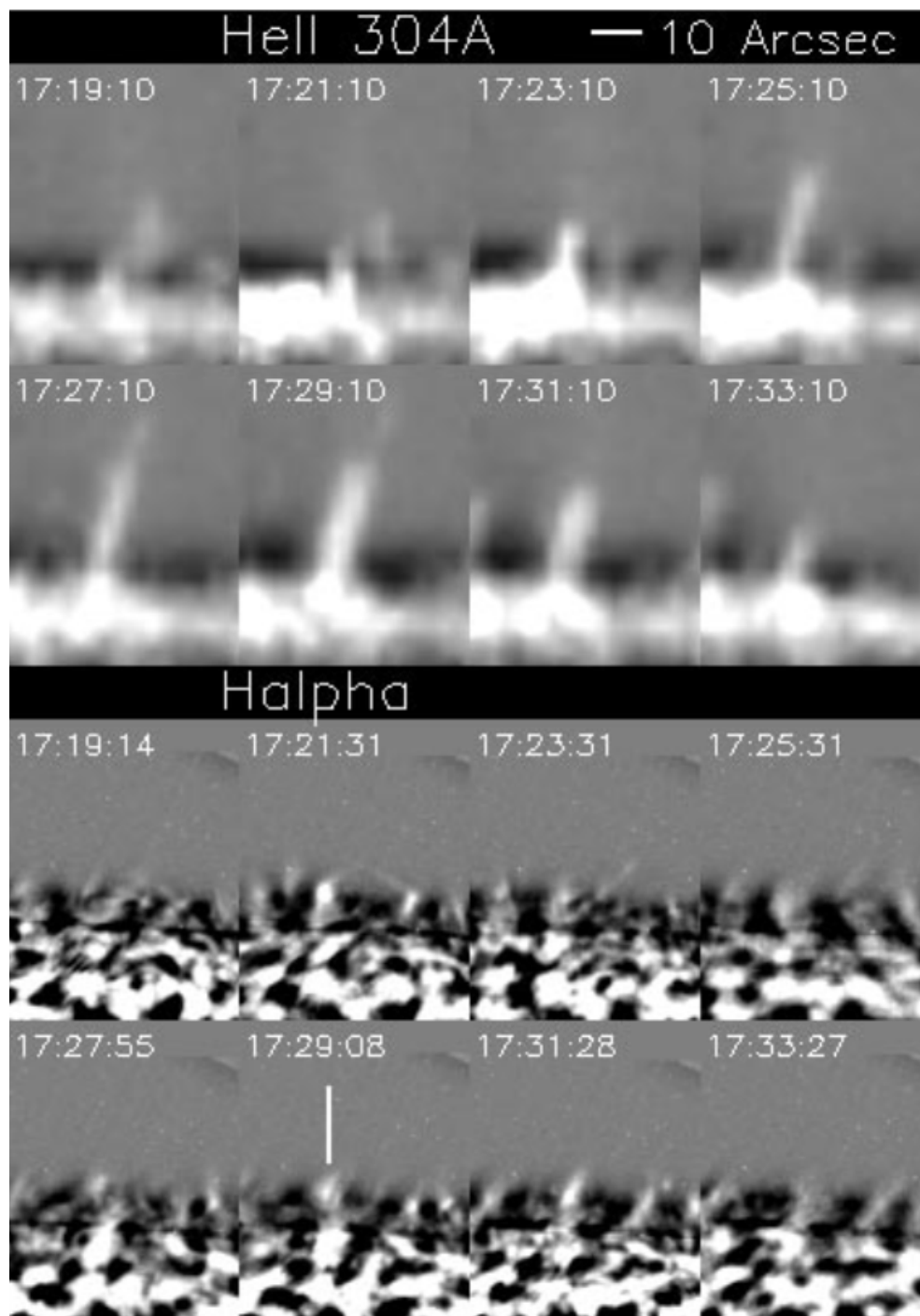
Figure 1.7: Comparison of the same northern coronal hole observation in Hα (middle panel) and its blue wing (top panel) and red wing (bottom panel). Image courtesy of Wang (1998).

spectroheliometer on *Skylab*. An image enhancement algorithm was applied (Koutchmy et al., 1988) to localise significant changes in the observations. The processed images displayed a vast collection of spicules (Karovska et al., 1994). Some spicules appeared to be longer than 10 arcsec and were considered MS. These ejecta seemed to be highly structured, twisted, arch-like phenomena in continuous interaction with the surrounding environment. One of the macrospicules originated at the top of a magnetic loop. The ejecta reached a maximal height of 50 arcsec after an eruptive evolution and extension. Due to the limited field of view, further plasma motion could not be confirmed in the decaying phase of the jet.

A new chapter opened in the history of MS observations when the *Solar and Heliospheric Observatory* (SOHO, Scherrer et al. 1995) was launched on 2 December 1995. During the still ongoing 23 year-long operation of the satellite, its Coronal Diagnostic Spectrometer (CDS, Harrison et al. 1995) provided continuous observation in the 10 - 80 nm spectral domain, which contains various emission lines from trace elements in the solar atmosphere.
Based on these improved detection techniques, Pike & Harrison (1997) identified a single MS in the southern polar region. The physical parameters of the MS were the following: 42 arcsec in height and 18 arcsec width. The jet was mapped simultaneously in three emission lines, and the observed nature was different in each raster: in the He I 58.43 nm emission line (2×10^4 K), two footpoints were detected, and the central part of the jet seemed to be less bright. In the O V 62.97 nm line (2.5×10^5 K), the fainter core was still visible, but only one footpoint appeared. However, the raster of the Mg IX 36.8 nm emission line (10^6 K) revealed a new behaviour of MS: high-temperature plasma rose up from the solar limb, where the MS was visible in the other images. This finding was contradictory to the 10^5 K upper of temperature limit determined by Bohlin et al. (1975). Furthermore, the velocity profiles of each raster were estimated with the examination of the line profiles. Due to the red-shifted nature of the emission originated from the western side of the MS, the material was quickly moving away from the observer with a maximal speed of $150-200$ km s^{-1}. The authors suspected that this was a concentrated plasma flow in the non-radial, open structure of the MS

based on the structure of the velocity profile. Consequently, MS could play a significant role in the acceleration of the solar wind.

Macrospicules were described as propagating solar tornadoes by Pike & Mason (1998). In the synoptic observations of *SOHO/CDS*, five jets were identified from the northern and one from the southern hemisphere in the following spectral lines: He I, O V, Mg IX, and Fe XVI (2×10^6 K). To obtain information about the radial velocity of these jets, the authors adapted a new technique: generating *Quick Velocity Maps (QVM)*. In the QVM, the shape of the jets was cylindrical with strongly red- and blue-shifted sides. These velocity distributions indicated a strong rotational motion of the plasma around the central axis of the jets as seen in the right-hand-side panel of Figure 1.6. Above a 30 arcsec of height from the footpoint of the jets, their radial velocity reached their maxima with ± 30km s^{-1}. No significant plasma movement was detected outwards (i.e., parallel with the central axis). Moreover, the cool core of the jets, which mainly emits in Hα, seemed to co-rotate with the EUV emitting sheath. Shibata & Uchida (1986), Kudoh & Shibata (1997), Shibata (1997) discussed a theoretical model for the tornado-like structure of MS: the footpoint of the jet was continuously twisted by plasma motions and convection under the photosphere. This three-dimensional model described the properties of Alfvén waves which were generated by the reconnection of the ambient magnetic field and a plasmoid or helically twisted region. These Alfvén waves could play a dual role in the motion of the jets: they excite large transversal motions which are observed as spinning and cause further acceleration of the jet by exerting a non-linear magnetic pressure force. The O V measurements of Pike & Mason (1998) appeared to be consistent with the theoretical models.

Similarly to the work of Moore et al. (1977), a detailed comparison between Hα and EUV MS was carried out by Wang (1998). Simultaneous observations were performed in Hα by BBSO and in He II line by the *Extreme Ultraviolet Imaging Telescope* on-board *SOHO* (*SoHO/EIT*, Delaboudinière et al. 1995). The structure of both phenomena was utterly different as seen in Figure 1.7: EUV MS reached higher into the solar corona, while Hα jets were evolving from a loop-like structure and their maximal length was significantly shorter. In the case of 57 potential EUV MS, all of these phenomena had counterparts in Hα. On the
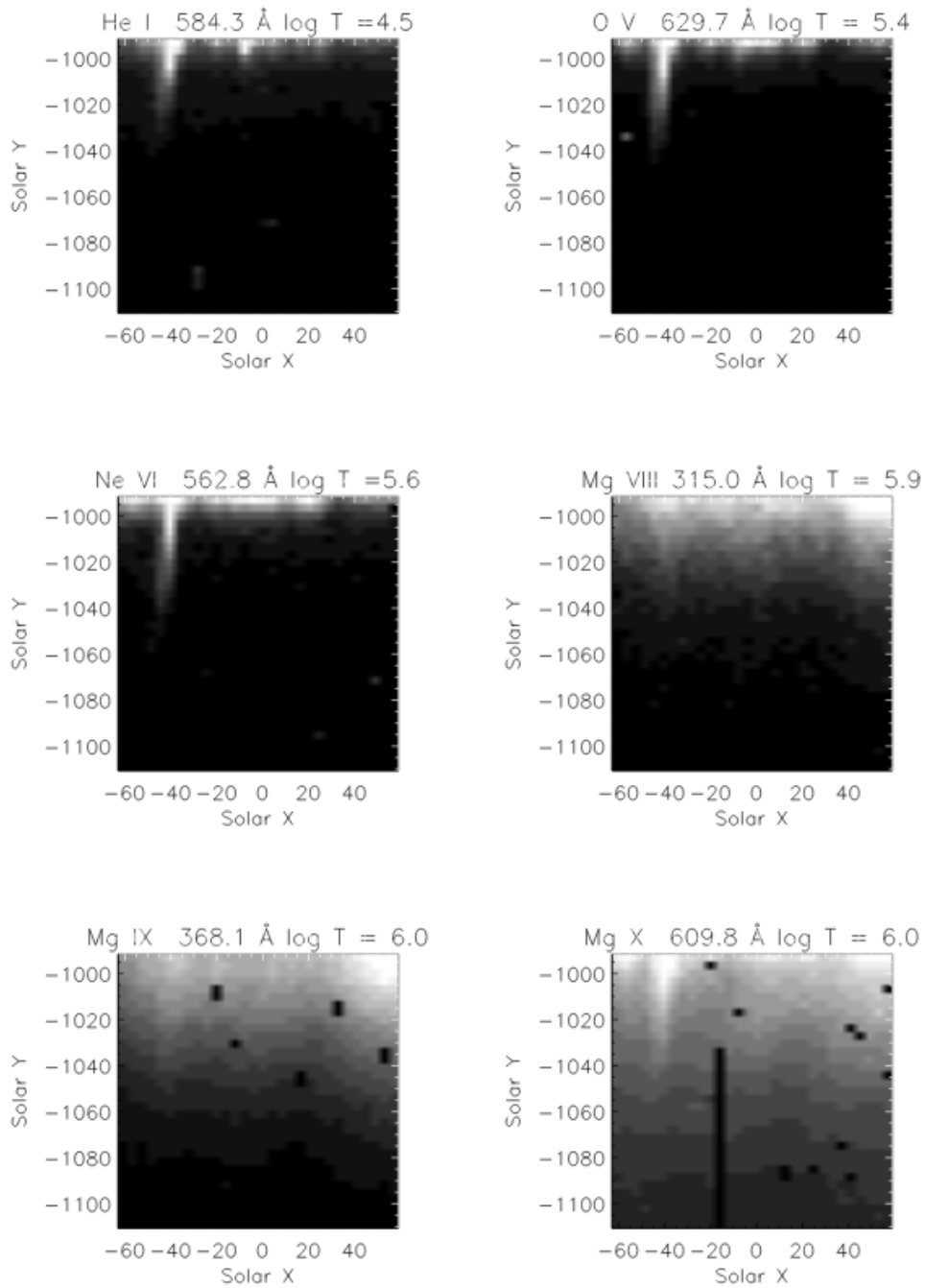
Figure 1.8: Macrospicule detections in several different EUV emission lines within a southern polar coronal hole. The jet is clearly visible in chromospheric and Transition Region lines. Image courtesy of Parenti et al. (2002).

other hand, out of the 108 Hα candidates, only 55 had no counterpart in EUV (that is more than 50%). This separation could be rooted in two reasons: i) Hα MS appeared in those magnetic reconnection sites, where the magnetic field did not have a strong vertical component; or ii) the temperature of the plasma was not high enough to reach bright emission in He II (10^4 K for Hα and $5-8 \times 10^4$ K for He II). The estimate of the birth-rate of the two classes revealed a strong asymmetry: Hα jets appeared with the same rate independently from their latitudinal position (0.5 events s^{-1}), but their morphology varied: around the poles, 57% of them were evolving from loop-like structures, while this fraction could reach 90% around the solar equator. For EUV MS, these jets tended to form closer to the solar poles (2.7 events s^{-1} for the poles and 0.2 events s^{-1} for areas around the solar equator). The authors suggested that magnetic reconnections drove MS at network-ephemeral regions or network-intranetwork interaction zones (Chae et al. 1998; Wang 1998). However, no relationship was found between the generation and evolution of spicules and macrospicules.

During the decades of MS observations, several suggestions arose about the definition of MS and how to differentiate them from other ejecta and eruptive events in the chromosphere. Georgakilas et al. (1999) aimed to distinguish macrospicules (or giant spicules, as the authors called them) from polar surges by comparing the Hα images of the Vacuum Tower Telescope at Sacramento Peak Observatory and the He II images of *SOHO/EIT*. Polar surges appeared simultaneously in the observations of both instruments and reached 58 arcsec height in EUV (with the lifetime of 43 minutes) and 10 arcsec in Hα (30 minutes lifetime) and had a complex structure. Giant spicules were much shorter (17.4 ± 2 arcsec), with less complicated structure, and they were also less eruptive and hardly detectable on Hα. The reason for this elusive nature could be a projection effect, the low resolution of the instruments or the low density of macrospicules. The results supported the multi-thermal model of MS. The authors found a strong agreement between physical distributions of their observations and the ones in the literature alongside with the MS counting of Johannesson & Zirin (1996).

Banerjee et al. (2000) observed and analysed a macrospicule in a polar coronal hole in the northern hemisphere by *SOHO/CDS* in the Mg IX and
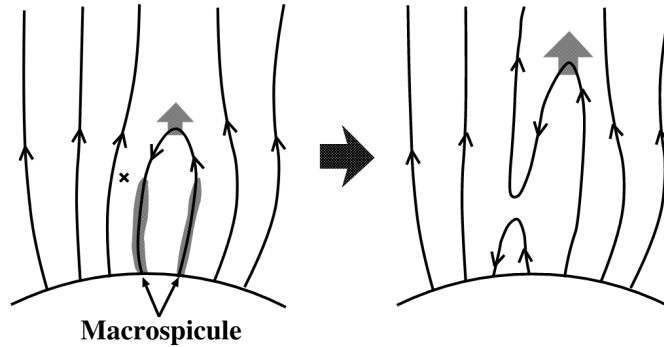
Figure 1.9: Schematic figure illustrates the driving mechanism of an eruptive-loop macrospicule. Image courtesy of Yamauchi et al. (2004).

O V emission lines. According to the classification of Loucif (1994), the discussed ejecta were a plasmoid-releasing phenomenon. On the velocity map, which was constructed based on contrast-enhanced maps (Doyle et al., 1999), the interpreted tornado-like behaviour was similar to the ones found by Pike & Mason (1998): one side of the MS was blue-, and the other side was red-shifted. After the investigation of space-time plots, evidence was obtained for fragmentation and ballooning (Habbal & Gonzalez, 1991). However, due to the lack of measurements along the central axis of the jets, the actual velocity of the jet (therefore, its possible contribution to the solar wind) could not be studied. The wavelet-analysis of the intensity variation at a given point of the observation showed a strong periodicity of 20 - 24 minutes, which could indicate the presence of slow-magnetoacoustic waves. Such waves were reported by Ofman et al. (1999), who investigated the propagation of magnetoacoustic waves in a gravitationally stratified, one-dimensional model of solar plume.

Parenti et al. (2002) applied a new noise removal algorithm to maximalise the signal-to-noise ratio during the observation campaign. The first detection contained the jet itself in a polar coronal hole region in the southern hemisphere, the other two measurements did not include the jet but served as a background for noise-reduction. The first goal was to study and then remove the spectra of the plume plasma: the possible bias of their emission needed to be reduced due to the similar temperatures of MS and plume plasma (Deforest et al. 1997; Young et al. 1999). The obtained, noise-removed images are presented in Figure 1.8. After the
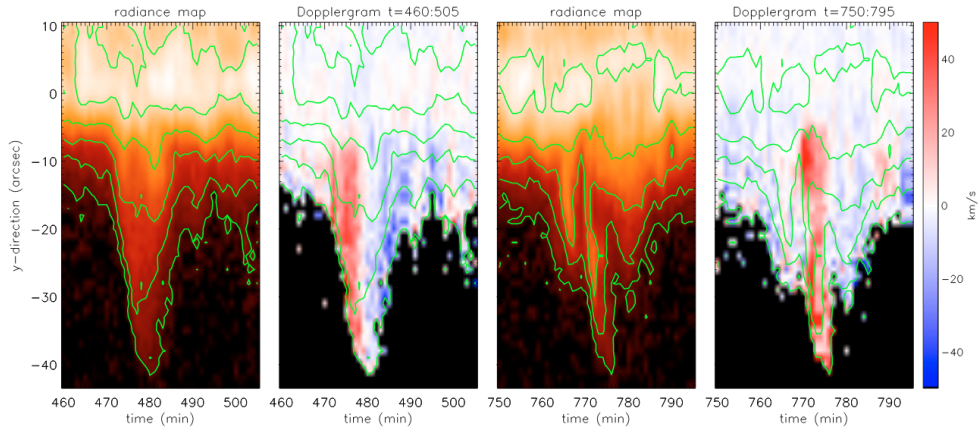
Figure 1.10: Time-distance diagrams of the N IV 76.5 nm intensity of two macrospicules (first and third panels), and their Dopplergrams (second and fourth panels). On the Dopplergrams: blue and red colour displays the radially approaching and receding plasma. Image courtesy of Xia et al. (2005).

correction, the entire evolution of the jet could be followed with a higher signal-to-noise ratio: in the first nine minutes, the structure of the MS expanded into the solar corona and reached a height of 33.5 arcsec. After the expansion, a plasma blob was formed and started to rise into the solar corona, while the remaining part of the MS descended to the limb. The velocity profile of the jet decreased as function of distance from the limb. After the second-order polynomial fitting to the mean values of velocities in each map, the initial velocity was found to be around 81.6 km s^{-1} with a deceleration of 0.204 km s^{-2}, which corresponds to the gravitational acceleration of 0.244 km s^{-2} at 40 Mm distance above the solar limb. However, this deceleration was not constant but decreased with the distance. Therefore, the speed of the released plasmoid could be around 26.3 km s^{-1} at a distance of 60 Mm.

Instead of the classification based on the spectral band of the observation or the surrounding environment, Yamauchi et al. (2004) suggested categorizing MS based on their behaviour: erupting loop MS or single-column spiked MS. Jets reported in their paper were observed in polar coronal holes using the Hα line of BBSO (Denker et al., 1999). In order to distinguish MS from other chromospheric ejecta, the authors constructed a system of four criteria: macrospicules must be i) located near the solar limb; and ii) bright structures over the limb; and iii) longer than 20
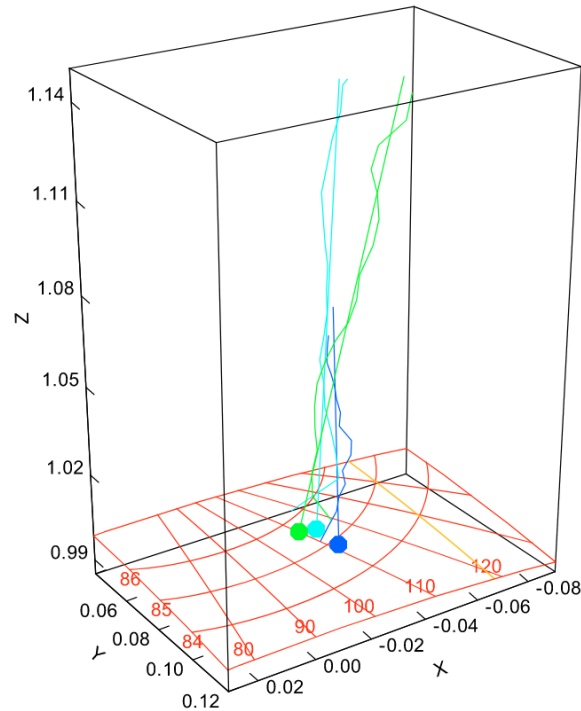
Figure 1.11: The 3D reconstruction of the movement of a macrospicule based on the observations of *STEREO/SECCHI*. Image courtesy of Kamio et al. (2010).

arcsec; and iv) uninterrupted by any other structures or observing biases during their entire lifetime. After the application of these criteria, 35 MS were discovered during the data collection campaign of six days. The ratio between erupting loop and single-columned spiked MS is 17 to 15 with three having uncertainty in their classifications. Erupting loop MS had a slightly greater physical extent in comparison to single-column spiked MS with a height of 20 arcsec compared to 16 arcsec and a width of 10.4 arcsec as opposed to 10 arcsec. For erupting loop MS, a small-scale magnetic loop was visible before the appearance of the jet. As the magnetic loop rose into the solar atmosphere, it reconnected with the ambient magnetic field, and the particle acceleration from the top of the loop to the bottom brightened up the loop (a sketch of this process is provided in Figure 1.9). This behaviour was apparently similar to the nature of Hα eruptive filaments (Hermans & Martin 1986; Wang et al. 2000). For this reason, Yamauchi et al. (2004) suggested that eruptive loop MS

are small-scale filaments. The evolution of single-column spiked MS was well-described by the Shibata reconnection model (e.g., Shibata et al. 1992; Yokoyama & Shibata 1995, 1996) in which reconnection happens between a network-scale closed dipole and the open field of the coronal hole. The reconnection between the two fields builds up new closed loops, hence, the parent loop becomes greater and brighter. On the top, the reconnection releases a slingshot-like dynamic open field, which is the driver for the upward motion of the body of the jet. The typical Y-shape of the MS is built up from these two components until the loop stops the expansion and the whole system collapses. As a conclusion, the authors discussed the possible contribution of such jets to the coronal heating and the solar wind acceleration.

During the observation and statistical analysis of EUV spicules in *Solar Ultraviolet Measurements of Emitted Radiation (SOHO/SUMER, Wilhelm et al. 1995)* images, Xia et al. (2005) identified several jets with more than 30 arcsec in height, which were classified as macrospicules. Their results revealed the complex structure of MS: several local maxima were reached before their collapse which would indicate the presence of other jets or returning plasma from the corona as demonstrated in Figure 1.10. The radial velocity increased with the distance along the central axis of the jet and reached its maxima between 20 and 30 arcsec from the footpoint: 40 ± 20 km s^{-1} redshift and -20 ± 10 km s^{-1} blueshift were measured in the Dopplergrams.

Kamio et al. (2010) mapped the 3D movement of an EUV macrospicule and an X-ray jet with the co-aligned observations of several instruments in the following lines: X-ray emission detection by the *X-Ray Telescope* (*XRT*, Golub et al. 2007), EUV observation (He II 30.4 nm) by the *Extreme ultraviolet Imaging Spectrometer* (*EIS*, Culhane et al. 2007) on-board the *Hinode*, and the *SECCHI* (Howard et al. 2008; Wuelser et al. 2004) instrument on STEREO (Kaiser et al., 2008) with the addition of the data of the *SOHO/SUMER* spectrometer. The central axis of the EUV jet was located between the two threads of X-ray jet. After the disappearance of the X-ray jet, the EUV MS was still in the rising phase with 130 ± 30 km s^{-1} radial and 25 ± 5 km s^{-1} horizontal velocity. Due to the fortunate positioning of the slits of the *SUMER* and *EIS* instruments, the radiance and Doppler velocities were measured for both edges
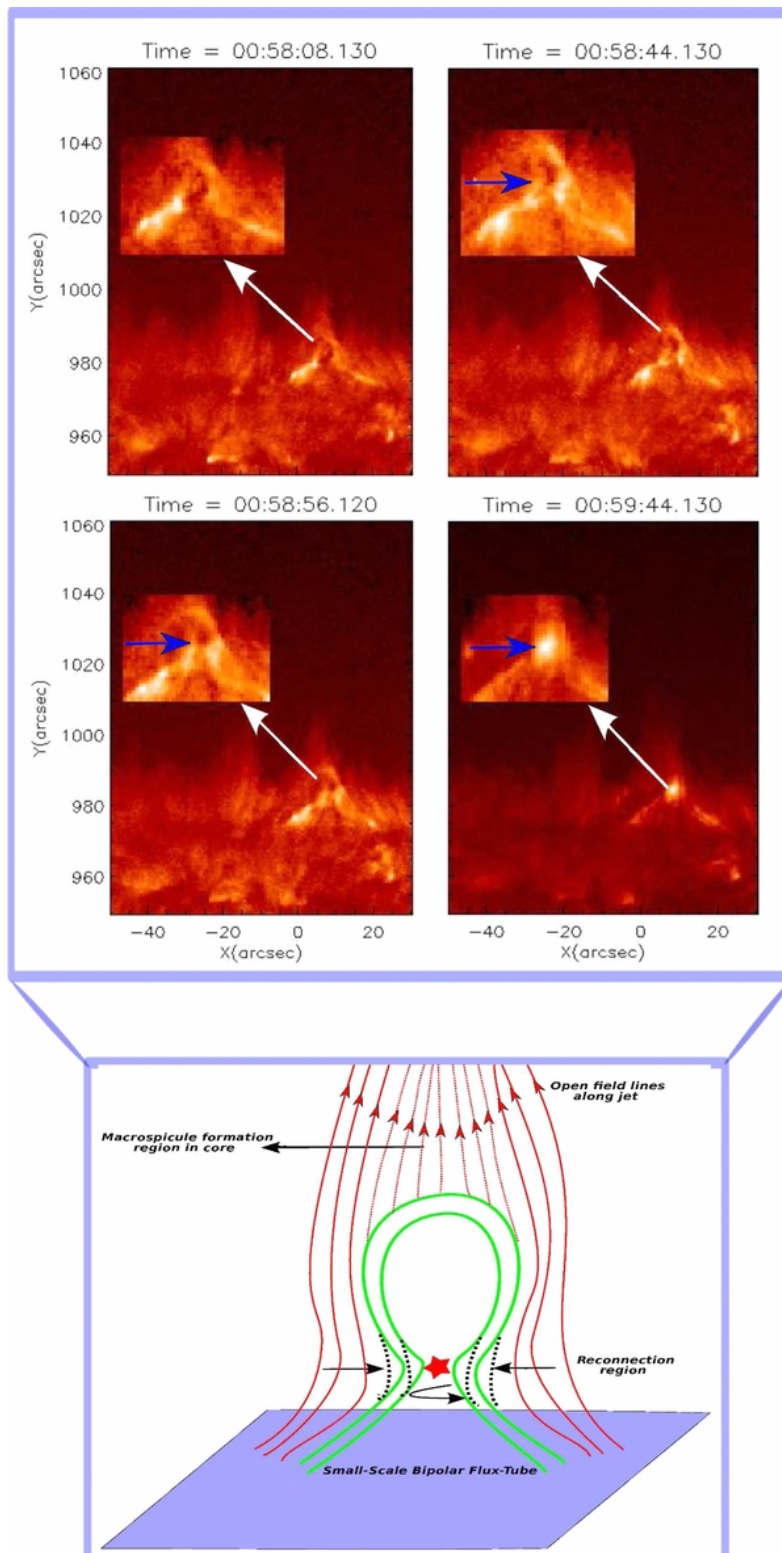
Figure 1.12: The top panel shows snapshots from the evolution of a macrospicule. The bottom panel illustrates the evolution of an omega-shaped magnetic loop, which emerges into the ambient open magnetic field. Image courtesy of Kayshap et al. (2013b).

of the jet. The measurements uncovered a significant difference between the MS and X-ray jets: the MS was composed of cool, rotating plasma, while hot outflowing plasma was identified as the X-ray jet. The authors were also able to reconstruct the helical upward motion of the MS in a Heliocentric Earth Equatorial (HEEQ) coordinate system based on the *SECCHI* observation from two different viewpoints as illustrated in Figure 1.11.

Off-limb and on-disk macrospicules and their possible relation to other mid-solar atmospheric structures were investigated by Scullion et al. (2010). The study focused on the parameter variation of the N IV 76.5 nm (1.4×10^5 K) Transition Region line and the Ne VIII 77 nm (6.3×10^5 K) coronal line. In both lines, high upflowing velocities were detected: 80 km s^{-1} and 145 km s^{-1}, respectively. The authors also suggested that MS could play a role in the problem of coronal heating and the acceleration of the solar wind.

Madjarska et al. (2011) analyzed three MS with aligned observations of several instruments in the following lines: Ca II H imaging with the *Solar Optical Telescope* (*Hinode/SOT*, Tsuneta et al. 2008b), EUV observation with the *Hinode/EIS*, X-ray emission detection with the *Hinode/XRT* and the *SOHO/SUMER* spectrometer. The two sides along the central axis of the investigated jets showed a blue- and red-shifted profiles in several Transition Region lines which corresponds to radial rotating motion (as reported by Pike & Mason 1998; Parenti et al. 2002). However, the co-aligned detection of SUMER and SOT also revealed a strong up- and downwards motion (50 to 250 km s^{-1}). Such a signal could be generated by an untwisting motion of a magnetic flux rope. By the study of iron lines between Fe VIII up to Fe XVI, the jets did not appear in the images, which indicates that the temperature of the plasma is lower than 3×10^5 K. This result contradicts to the study of Pike & Harrison (1997), but the different approach (or identification) of the MS could be the source of this deviation.

A direct comparison of MS observations and their numerical simulation was carried out by Kayshap et al. (2013b). Based on the high spatial resolution of *Atmospheric Imaging Assembly* (AIA) (Lemen et al., 2012) on-board the *Solar Dynamics Obervatory* (SDO) (Pesnell et al., 2012) (for more details, see Section 2.3), a single macrospicule was observed after

evolving from a small-scale flux tube in the northern polar coronal hole. The omega-shaped magnetic flux underwent a kink perturbation caused by apparent rotation and transverse bending. During the kink oscillation, the two halves came closer and reconnected, causing a brightening in the observation and the triggering of the jet itself. Both the observations and the corresponding sketch of the magnetic field line configuration are presented in Figure 1.12. The jet existed for 24 minutes and reached up to 52 arcsec into the solar corona. The authors constructed a two-dimensional numerical simulation with the FLASH code (Lee & Deane, 2009) and applied the VAL-C atmospheric conditions (Vernazza et al., 1981). According to their results, the plasma of jet followed a slow shock wave, which was excited by a velocity pulse (Shibata 1982; Murawski et al. 2011; Kayshap et al. 2013a).

A relationship was found by Gyenge et al. (2015) between the active longitudes (Gyenge et al., 2012, 2014), determined by sunspots, and the longitudinal distribution of MS in Carrington coordinate system. A strong asymmetry was discovered in the latitudinal distribution of the jets: 95% of MS were formed within 27° from the solar poles. Furthermore, the formation zones of MS likely tended towards the bands of active longitudes with an average separation of $\pm 36°$. The authors claimed that the northern hemisphere was more active both with respect to MS generation and sunspot formation, which could possibly be related to solar dynamo processes.

Bennett & Erdélyi (2015) identified and registered 101 MS by applying a clear system of criteria. Data were collected between June 2010 and December 2012 and the jets categorised based on the surrounding atmospheric environment. Several physical parameters of jets were estimated: maximum length (22 – 78 arcsec), maximum width (4 – 18 arcsec), maximum upflow velocity (55 - 250 km s^{-1}) and lifetime (6 – 25 mins). The tilt angle between the central axis of the jets and the limb seemed to be smaller for jets inside coronal holes. For the long-term variation of these properties, the authors found linear correlations temporally. The authors also estimated the formation energy of the jets based on their potential energy: $10^{13} - 10^{18}$ J energy is required to launch the mass of the ejecta to reach the observed heights taking into account the different scale-heights of the surrounding plasma environment.
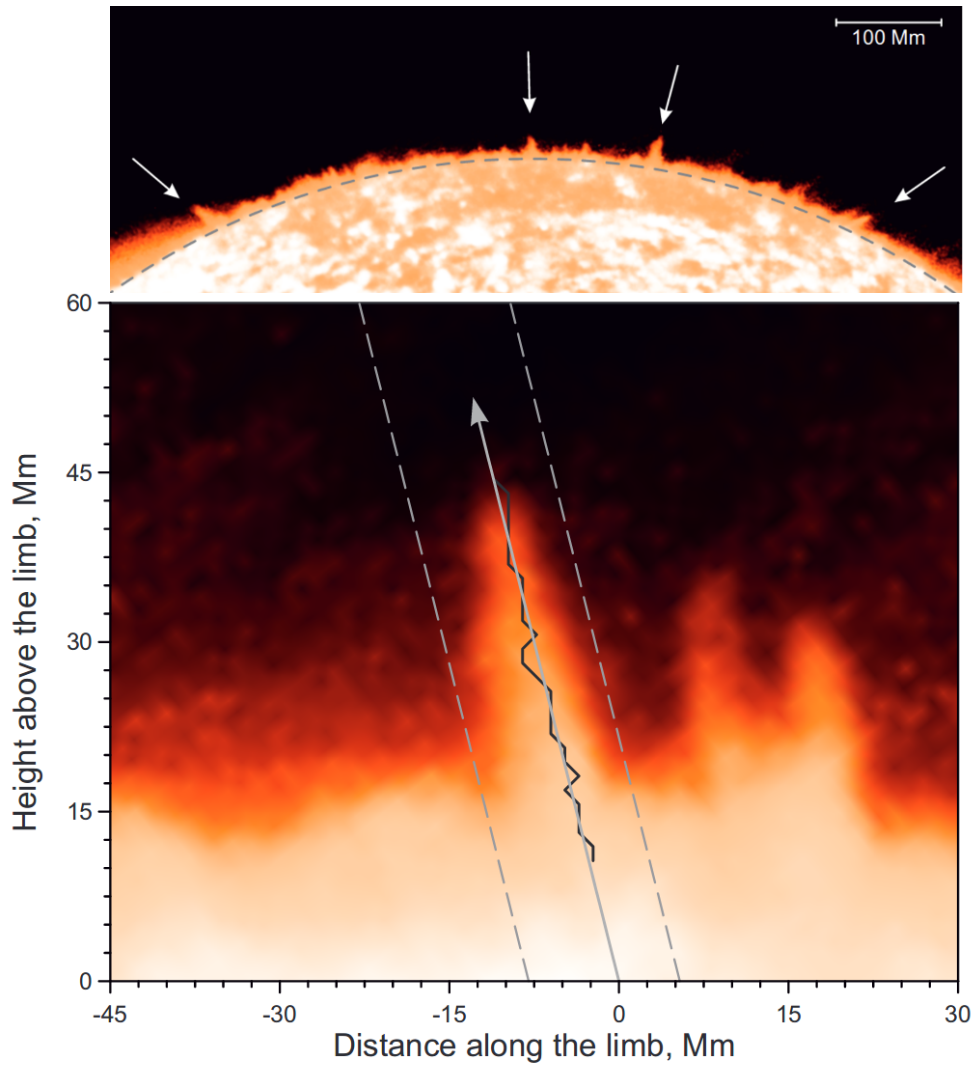
Figure 1.13: The top panel represents an example of a Telescope-Spectrometer for Imaging Solar Spectroscopy *TESIS* observation in the 30.4 nm line. Several jets are seen on the image inside the northern polar coronal hole. The bottom panel shows a maximum intensity map of a macrospicule, the blacks lines indicate the spine of the jet. Image courtesy of Loboda & Bogachev (2017).

Recently, Loboda & Bogachev (2017) found 36 He II jets using the observation of the *Full-disc EUV Telescope (FET)* mounted on *TESIS* (Kuzin et al., 2011) as illustrated in Figure 1.13. The height and lifetime range of the MS were around $40 - 60$ arcsec and $10 - 20$ minutes, respec-

tively. In order to obtain detailed information about the internal velocity field of the optically thick plasma base of the MS, a one-dimensional hydrodynamical approximation was applied with the addition of a simple radiative transfer model. The velocity maps of 18 jets were constructed with this method, and 12 of them were following a similar motion pattern: i) the plasma moved upwards until its maximum; and ii) the velocity began to drop, and vanished eventually at some point and then reversed; and iii) the jet fell back to the solar limb. The trajectory of 15 jets was found to be parabolic with a high accuracy. The deceleration of the jet was typically between 160 to 230 km s^{-2}, which is slightly less than the 240 km s^{-2} gravitational deceleration at the height of 40 Mm. Furthermore, the authors were able to detect three compressional waves on the body of an MS, based on velocity maps, and interpreted these as magneto-acoustic waves. Additionally, $10 - 30\%$ of the mass of the jets seemed to become lost according to the estimates made by the authors. By taking typical values of such ejecta, approximately 10^8 kg s^{-1} mass faded out from the images, and therefore, likely accelerated into the solar corona and possibly into the interplanetary space with the solar wind.

1.4   Outline of the Thesis

This Thesis contains 6 chapters. In this work, the author aimed to investigate the variation of local, short-scaled jets, the macrospicules over a several-year-long time domain. Collecting the characteristics of these jets and compare them to other solar activity proxies would unveil their possible connection to large-scale magnetic processes in the solar atmosphere. Chapter 1 provides the necessary background on the structure of the solar corona and solar activity. A comprehensive historical review of MS detection and simulation is also presented here.

In Chapter 2, the criteria for classifying a feature as MS is discussed along with the date selection method and the digitalization algorithm, the tetragon approximation. As the primary source of observations, the science programme of *Solar Dynamics Observatory* and its *Atmospheric Imaging Assembly* is detailed with the origin of solar activity proxy data and the applied statistical methods.

Chapter 3 focuses on the long-term variation of five physical parameters of MS. Each physical parameter is cross-correlated with each other to analyse to connection between them. Furthermore, the connection is investigated between the long-term variation of MS and the timesets of other solar activity proxies.

The spatial distribution of MS around the solar disk is discussed in Chapter 4. MS are mostly formed around the solar poles. However, the generation rate of MS is hugely asymmetric between the two hemispheres of the Sun. Chapter 4 also seeks to interpret the periodic migration of MS away from the solar poles.

The orbits of each MS in the dataset are analysed in Chapter 5. The collected height parameters are studied in order to understand the kinematics of these jets. Kinematic and dynamic modeling to simulate the motion of the jets are also discussed.

In Chapter 6, a summary of the results is provided with the conclusions of the potential findings. Our own theoretical conjecture is presented here about the possible double magnetic cycle and the structure of the double solar dynamo. Lastly, we outline a few breakout points in order to inspire scientists for further work in the research area of macrospicules and chromospheric jets.

Chapter 2

Database and Methodology

2.1 Definition of Macrospicules

In the literature summary it was already been discussed, that the majority of studies about Hα or EUV macrospicules mainly focus on a low number of jets. For this reason, the aim of these investigations is to compare the physical properties and evolution of a few jets to theories or numerical models. The longest time-span of such observations covers a few days. Several unanswered questions arise after the consideration of these studies: may the physical properties of MS vary on a long time-scale? If the generation of jets is strongly influenced by the evolution of the global magnetic-field, should we observe similarities between the properties of the solar cycle (i.e. solar activity proxies) and the parameters of MS?

To answer these questions, an extensive dataset of chromospheric MS is required to be constructed over multiple years of observations. By considering and examining several examples of datasets covering observations of a specific subject over several years or even longer time, the foundation for such projects is always a firm definition system. The relevant criteria must provide a straightforward and precise set of standards. Therefore, the observed phenomenon or feature has always been compared to this standard during the data collection phase of the research. If the studied phenomenon fits in or behaves similarly to the standard, the observed structure is registered into the dataset. This selection method

is recurrent. Thus, we intended to implement a sequence of criteria to select macrospicules from the diverse family of chromospheric ejecta.

Each MS definition was valid on its own in the past. Regardless of the fact that one could contradict the other, none are more valid or worse than the others. Observational technology and detection techniques are improving continuously. Consequently, the diversities between the various MS could grow. Hence, we aim to find the golden middle way between the different MS definitions. Our criteria to macrospicules were constructed after reviewing the literature. Our choice enables our research to be strongly analogous and comparable to the vast majority of the literature.

The definition of MS in this Thesis is summarised in the following five points:

- **Shape regulation:** Since MS are jets in the solar chromosphere, their lengths should be multiple times longer than their widths. There is no hard limit for the ratio between the height and the width of MS. By considering the previous studies, the maximal height of the jets should be at least twice as large as their maximal width (Bennett & Erdélyi, 2015). Their appearances must be similar to "spikes" or "cigars".

- **Area restriction:** To gain precise information about their upward motion, MS must be generated and evolve visibly on the solar limb (off-disk). Investigating EUV images, the solar limb could be separated into three segments based on the overall intensity of the segments: quiet Sun [QS], coronal holes [CH] and the active regions [AR]. ARs are high-intensity areas around the solar equator, where the magnetic flux is higher due to flux emergence from the convective zone (Hathaway, 2012). On the other hand, the intensity of CH is much lower due to the lower plasma density (Cranmer, 2009). The ARs are excluded from this analysis due to two main reasons: i) since MS are mostly observed in CH and QS in the literature, we intend to keep our criteria consistent with those studies; and ii) the large-scale magnetic field of an AR may be able to generate MS-like phenomena (Chandra et al. 2015; Sterling et al. 2016), which could be different in terms of physics from MS formed in CH or QS areas

(Kayshap et al., 2013b).

- **Size limitation:** This point serves as a filter which distinguishes macrospicules from all the other jets and ejecta in the solar atmosphere. In the vast compilation of chromospheric structures, jets could reach various sizes from the e.g. spicules (de Pontieu et al., 2007) to the giant size of surges (Foukal, 2004), which reach out into the interplanetary space. Criteria need to be constructed that distinguish MS from other phenomena. These limits are somewhat arbitrary, but build on the literature: MS are required to be between 10 and 70 Mm. Nevertheless, this threshold is not an exact limit. A jet could be registered as a macrospicule if it satisfies all the other criteria, but its length is slightly shorter than the threshold. However, in our experience, the requirement of a further brightening seems to limit the length of the MS more strongly.

- **Visibility principle:** If all the previous points are confirmed for a jet, we then need to make sure that its full evolution is visible during the observation campaign. If any other phenomena or structures cover some part of the jet, that would cause an error in the measurement of the physical dimensions of the jet. A similar difficulty also arises at the limb: the limb of the Sun could hide some part of the MS. The data, gathered from such ejecta, would be likewise biased. To avoid the effect of shielding, a simple rule is applied: the connection between the solar surface and MS must be apparent all the time during the lifetime of the MS. We refer to this feature as the observable footpoint of the MS. Such criteria were applied by e.g. Yamauchi et al. (2004).

- **Appearance of brightening:** A few minutes prior to the presence of the jet at the solar limb, a point-like brightening is required to be visible around the position of the footpoint of the MS, below the level of the limb. The existence of such bright point serves two purposes: i) the brightening confirms the visibility of the footpoint; and ii) the brightening indicates a possible heating mechanism, which could lead to the generation of the MS (Pike & Harrison, 1997).

If an observed structure satisfies these criteria listed above, the phenomenon is registered into the database as a macrospicule. Although, the definition is strict, smaller deviations are allowed based on the decision-making of the observer. The size of the jet could exceed the size limitation by approximately 10%. Also, there is no definitive description for the brightening at the footpoint of the MS. The actual intensity threshold that separates the brightening from the surrounding plasma environment depends on the point of view of the observer. However, together, the shape regulation, the area restriction, and the visibility principle are such pre-requisites that leave no room for subjectivity. Eventually, the gathering of MS has begun with these criteria and considerations. Figure 2.1 demonstrates the identification of the jets.
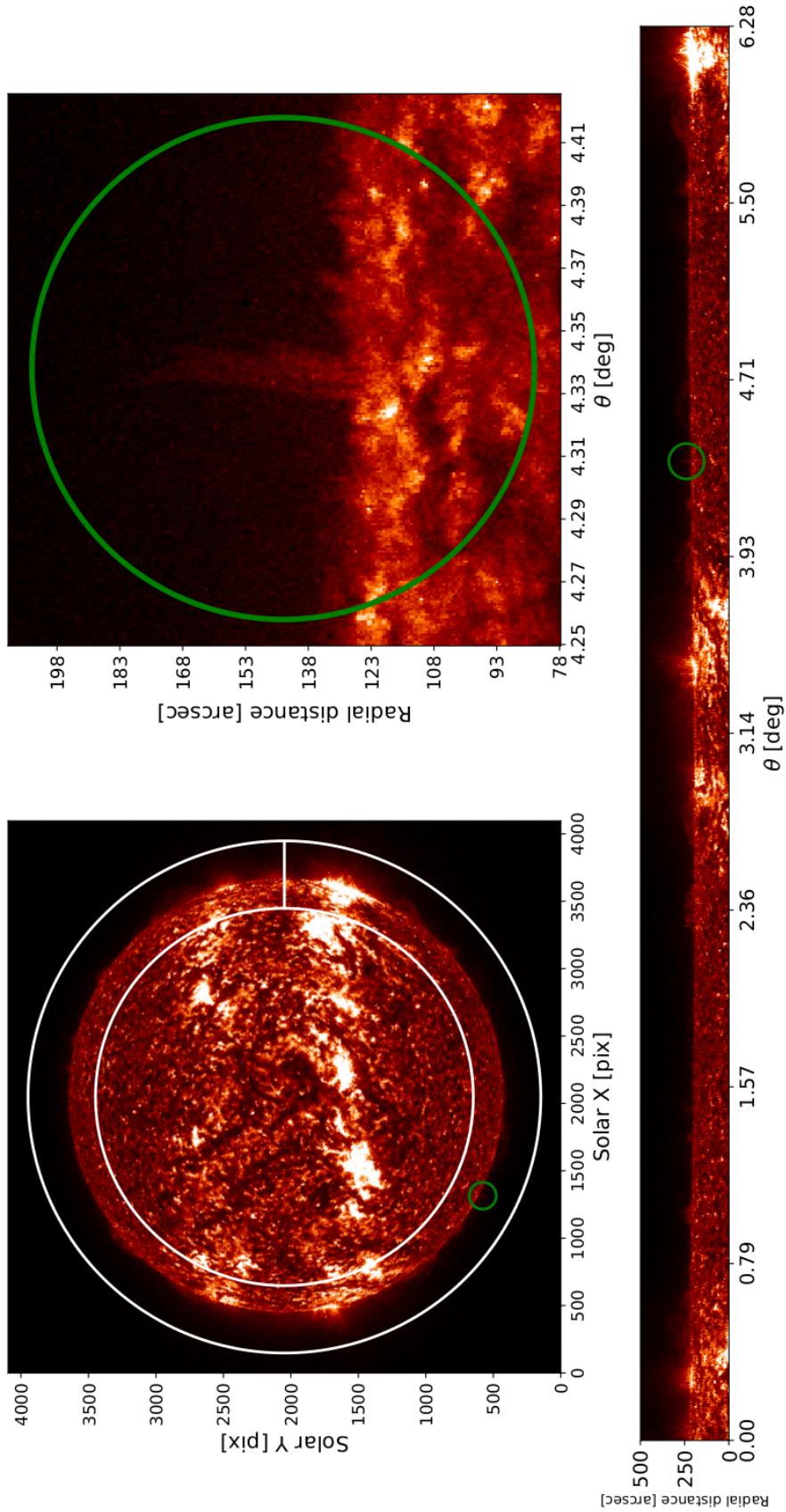
Figure 2.1: *Top-left panel:* Full-disk observation of the SDO/AIA 30.4 nm channel at the epoch of the maximum height of the investigated macrospicule. The two white circles demonstrate the boundaries used to cut out the limb. *Top-right:* MS on the solar limb. *Bottom panel:* The flattened solar limb. In all panels, green circles indicate the position of the macrospicule.

2.2   Digitalization of Macrospicules

Several statistical analyses was performed on the measured physical properties of MS during the research made for this Thesis. Such applications often require homogeneous sampling in time. If the sampling frequency of MS is inhomogeneous, a significant bias may appear during/while performing the analytical examination. To bypass this problem, MS were sought with an observational campaign selection mechanism. This method needs to be as homogeneous temporally as possible. Additionally, the process also requires to be relatively easy for both usage and later presentation.

According to the literature, the average lifetime of an MS is shorter than 30 - 35 minutes. For this reason, the length of one campaign window is set to be two hours. This time interval is long enough to observe several jets during the campaign. Furthermore, the amount of raw observation data is not going to reach a high level during the multiple-years long analysis and the storage requirement is manageable. A two-hour-long interval is chosen between 12:00 and 14:00 UTC on each given date of observation. Every 1st, 7th, 15th, and 24th of each month between July 2010 and July 2017 is chosen. This date selection is not entirely perfect, but it approximates closely a temporal homogeneity. The differences between the observing dates vary around 7$\pm$2 days. The deviation from homogeneity is not negligible on a short scale. However, the caused bias is going to be insignificant during the statistical investigation on a multiple-year-long dataset. This sampling method provides 772 hours of observation on 336 days.

During the data collection, covering an interval of 7 years of observations, MS were classified into two categories based on their surrounding plasma environment: quiet-Sun macrospicules [QS-MS] and coronal-hole macrospicules [CH-MS]. For those MS whose category was unclear or uncertain, a third class is created. These latter jets were called coronal hole boundary macrospicules [CHB-MS].

After employing these selection criteria and the system of definition described above to the raw images, 356 MS were identified and recorded into the database. The number of MS in each category are unequal: 180 CH-MS, 167 QS-MS, and 9 CHB-MS were registered during the data

gathering.

Figure 2.2: Evolution of a quiet-Sun macrospicule on the western limb on 24th April 2014. Yellow circles indicate the four points of the tetragon approximation. Cyan and white solid lines represent the actual height and width of the jet. The green tetragon indicates the actual area of the MS.

The population of CHB-MS is significantly smaller than the size of the

other two categories. Thus, the assembled information of CHB-MS is only utilized when the physical parameters of MS were investigated regardless of their classification. Therefore, only CH and QS are recognized as true and distinct classes of MS.

Nearly all the dynamic phenomena are morphologically irregular and sporadic in the chromosphere as can be seen in the raw observations. Their structure is complicated, and their evolution and movements are hard to predict. Jets, including MS, are not different from one another in this sense. However, a method is required to follow the evolution of jets regardless of their actual position and shape. The automated detection and investigation of MS are difficult due to several reasons. The recognition of shapes and structures requires the capability of the computer to store the parameter-space of several test-objects. Although, a method based on machine learning would provide information about the location of jets around the solar disk, difficulties would arise with respect to the fifth point of our criteria: finding the connection between the evolving jet over the limb and the previously existing brightening under the limb. Furthermore, after identification, the jets need to be tracked, and their physical properties have to be continuously monitored. A jet could be classified as MS in a given observation, but not in the next in step. This bias would generate non-continuous datasets. Therefore, the automated investigation of MS is undoubtedly outside of the scope of this research. An automated tracking of their movement and the recognition of their physical parameters would be excellent topics for future research.

Here, a more straightforward method was employed in the classification of MS: by "hand". Due to the cigar-like shape of the MS, we propose to parameterise these jets as tetragons. Unfortunately, the raw images do not provide any information about the line-of-sight (LoS) distribution or movement of the MS, as mentioned in Section 2.3. Therefore, these ejecta were considered as two-dimensional, plane objects. The geometric distributions of the tetragons (e.g., length, width, area) can be efficiently connected to their physical extents of an MS. In all the observations where MS are clearly recognisable, four points are fitted to the image of an MS. The first two points are the bottom and the top of the jet. The line which connects these points is the main axis. As the top and bottom points of the jets are determined first, the two side points are

placed along the small axis at those points, where the intensity fraction between the given point and the middle point of the MS (the intersection of the main and the small axis) is 0.8. Lowering this threshold was not preferable due to the noisy background over the limb. After testing several different thresholds on multiple jets, the 20% intensity drop proved to be the most ideal choice to characterise the boundary of the jet. This may sound somewhat arbitrary, but so would be any other employed definition as, strictly speaking, there is no sharp boundary between the macrospicule and its environment. Contouring the observations and find an intensity threshold as a boundary of the MS would have been a universal approach for analysing the physical extents of MS. However, we intended to keep the used methodology simple, so this method could be applied on as many MS as possible. However, this method would be an excellent project for a more general investigation of MS. The tetragon defined by these four points is the representation of the macrospicule in the given observation.

These four points are determined in a quasi-polar coordinate system. In the coordinate system of a Map object in Python, the origin is the center of the solar disk. However, a polar coordinate system is more beneficial to measure the position of MS on the solar limb. The distance of solar limb from the disk centre is around 1700 pixels ($\approx$ 1020 arcsec) on the raw images (for more information, see Section 2.3). Two arbitrary limits, i.e. distances from the centre of the disk have been defined in order to draw two concentric circles around the solar limb: 1400 pixels ($\approx$ 840 arcsec) and 1900 pixels ($\approx$ 1140 arcsec). For an easier visualisation, this circular strip has been transposed into a rectangle (Bennett & Erdélyi, 2015). The endpoints of the MS are estimated in this coordinate system. The advantage of this transformation are the easy image handling and shape recognition. Furthermore, these coordinates are easily converted into a heliographical coordinate-system in order to measure the actual position of the jet on the solar disk.

The physical properties of each MS are estimated by deriving the geometrical properties of its representative tetragon in each observation where the jet is clearly visible. The physical properties are measured as follows:
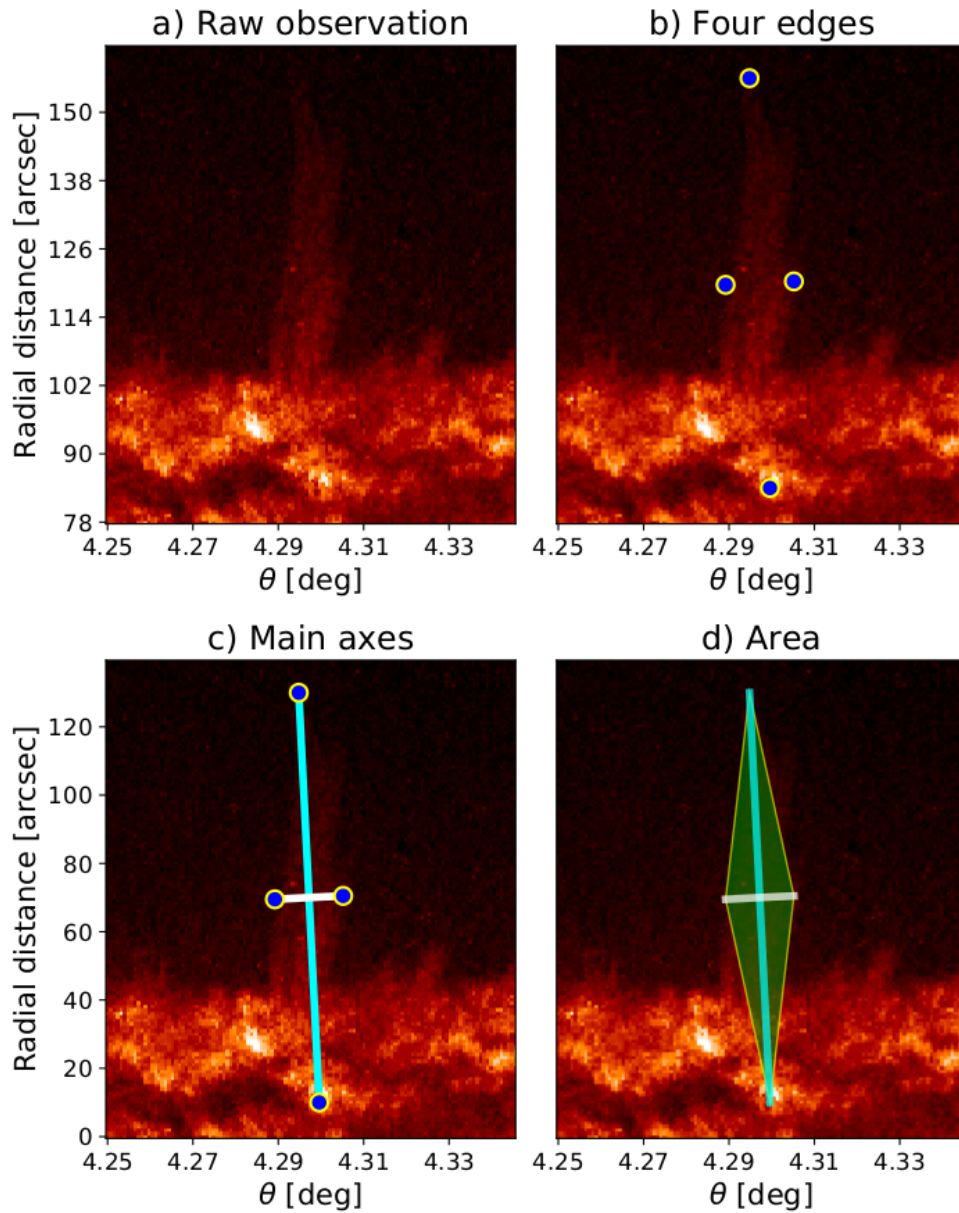
- **Length [Mm]:** The distance between the first and second points
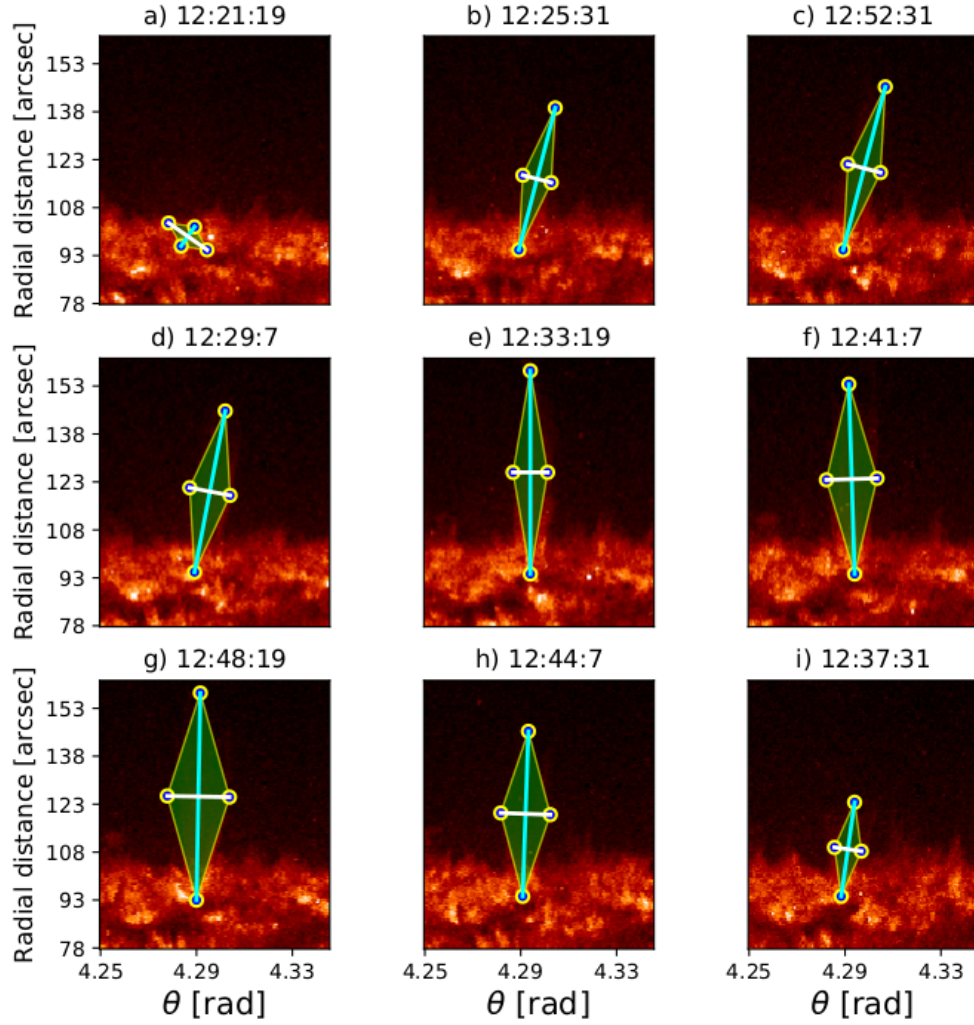
Figure 2.3: Evolution of a quiet-Sun macrospicule on 24th April 2014. Yellow circles indicate the four points of the tetragon approximation on the western limb. Cyan and white solid lines represent the actual height and width of the jet. The green tetragon indicates the actual area associated with the MS.

(alternatively, the length of the main axis).

- **Width [Mm]:** The distance between the third and fourth points (alternatively, the length of the small axis).

- **Area [Mm^2]:** The area of the representative tetragon.

- **Velocity [km s^{-1}]:** The fraction of the differences between the

length of two consecutive observations and the temporal deviation.

- **Lifetime [s]:**   The temporal difference between the first and the last observation of a given MS.

These characteristic physical parameters are displayed in Figure 2.2. According to the brightening criteria, the moment of appearance of the bright point was determined as the starting point for the MS observation rather than the presence of the ejecta itself. In the first few image frames of MS detection, the area of the brightening is becoming bigger, and the tetragon is following this evolution. Some uncertainties usually arise after this phase: the growth of the brightening stops, however, the jet has not appeared yet on the limb. This state lasts around 1 - 2 minutes. Thus, the top point of the MS is determined to become closer to the limb from one frame to another during this time. After the appearance of the ejecta, the top point will be located at the top of the jet, while the bottom point remains at the brightening. This detection method proceeds until the collapse of the MS. The jet reaches its final moment when the top point identifying the height of the jet, falls underneath the level of the limb. An example for demonstrating the entire evolution of a jet is in Figure 2.3.

The average number of MS in a given observational sequence is around 1.08. Therefore, the average rate of MS generation, based on our methods and criteria, is approximately 0.5 h^{-1}. However, the actual occurrences of MS vary between 0 and 5 during an observing sequence. The temporal inhomogeneity caused by this variation, must be limited to avoid any further errors in the statistical analysis. For this reason, we carried out a homogenisation process. This process is executed in two steps: i) if two or more MS are identified in one observational sequence, the average of all of their physical properties is estimated, and ii) if the number of MS in an observing block is zero, then an interpolation is applied in order to have the actual value of the physical properties for the given observing block. During the interpolation, the difference between the neighboring data points is divided by the temporal separation of the surrounding, non-zero, MS observational sequences ("the hole between the non-zero MS observations"). This fraction is multiplied by the actual temporal distance from the non-zero MS observation. Then, this value

is added to/removed from the known data accordingly to the increasing/decreasing trend as a final step. It is important to note that the homogenisation process does not change the long-term behaviour of the dataset, nonetheless, it significantly reduces the errors in the results of statistical applications. Only one single MS was observed in 146 observing blocks, hence, the data of these jets remain unchanged. The distribution of the previously described cases from the total observation is 99 (more than one MS) and 91 (no MS detection).

In summary, the following information has been gathered from the raw observations about each MS: the type of the MS, the four points of the tetragon approximation, and the actual moment time of all the observations when the MS is clearly visible.

It is also important to note that the current database was collected in three campaigns. During the first campaign, 301 MS were registered data taken between 1st June 2010 and 31st December 2015 (158 CH-MS, 134 QS-MS and 9 CHB-MS). Kiss et al. (2017) utilizied this original dataset. The first extension added 21 MS (7 CH-MS and 14 QS-MS) from 31st December 2015 to 01st June 2016 to the total of 322, and this extended database was studied by Kiss et al. (2018). For a more detailed temporal investigation, Kiss & Erdélyi (2018) investigated the final version of the dataset after the second extension with additional 34 new MS (15 CH-MS, 19 QS-MS) observed between 1st June 2016 and 1st June 2017.

2.3 Source of Data: *Solar Dynamics Observatory*

The source of the raw observations for our purpose in this Thesis needs to fullfil two basic requirements: i) the instrument has to provide continuous measurements on the basis of several-years in order to enable us to investigate the long-term variations of the MS, and ii) both the spatial (less than 1 arcsec) and temporal (less, then 1 minute) resolution should be adequately high as defined to be able to study the detailed evolution of the jets. The *Solar Dynamics Observatory (SDO)* satisfies both of these conditions. The satellite was launched in February 2010 as a ground-breaking mission of NASA's *Living With a Star* Program in order to provide a detailed, multiple-temperature investigation of the solar atmosphere during Solar Cycle 24. *SDO* started to return science observations on 1 May 2010. Three instruments were carried on-board this mission: the *Atmospheric Imaging Assembly* (AIA), the *Helioseismic and Magnetic Imager* (HMI), the *Extreme Ultraviolet Variability Experiment* (EVE).

The *Atmospheric Imaging Assembly* provides the raw observations for our research. The rapid, often less than a minute, appearance and disappearance of waves and ejecta phenomena are a challenging task to distinguish and monitor regularly. As the principal objective, *AIA* is continuously mapping the magnetic environment and the structural variations of several different layers through the entire thermal range of the solar corona from 1 MK to 20 MK. *AIA* also focuses on the local, small-scale conditions, which are connected to the topology of the global magnetic field. To accomplish these goals, *AIA* provides the following fundamental capabilities: i) a view of the entire solar disk and, ii) high signal-to-noise ratio to reach the best possible quality of observations and, iii) regular observations in every 10 - 12 s without any interrupting events or coverage. *AIA* is composed of four 20-cm, dual channel, f/20 Cassegrain telescopes. The charge-coupled devices (CCDs) of each telescope gather photons in ten different EUV/UV channels, including six channels in the lines of ionized iron. The 4096×4096 thinned, back-illuminated pixels correspond to a 41 arcmin circular field of view with 0.6 arcsec pixel resolution. To block any unnecessary radiation, entrance

filters are placed at the telescope aperture.

Each observation of *AIA* is guided with an additional telescope and the exposure time is limited to 3 ± 0.1 s. The instrument transmits the compressed observations to ground stations without any further data manipulation. The so-called Level 0 data are stored at the Joint SDO Operations Center (JSOC) science-data processing facility. Telemetry information is added into the header of the Level 0 data after its arrival from the satellite.

The Level 0 data is duplicated and stored. However, a two-step conversion is necessary to achieve a science-ready observation. First, the Level 0 data has dark current subtrackted, flat-field and bad-pixels corrected. Level 0 data is also rotated to place the solar North at the top of the image to reach co-alignment between the different channels. The details about this pipeline are further added to the header of the data and, hence, the observation becomes Level 1. Second, the Level 1 image is converted into Level 1.5 by the utilization of several image rotations. The fully-processed, Level 1.5 data is perfectly fit to serve as raw observations for our research due to their corrections and alignments.

Several studies in the literature, including the first ever MS detection of Bohlin et al. (1975), observed and investigated macrospicules at the He II 30.4 nm, optically thick, wavelength. This EUV line, formed in the chromosphere, is the most luminous EUV irradiance after the H II Ly-α. The source of He II radiation is the cool plasma ($T < 10^5$ K) of the quiet chromosphere, active network, and the plage regions (Worden et al. 1998; Andretta et al. 2012). The wavelength band around the He II 30.38 nm peak is observed by *AIA* Telescope 4. Furthermore, this wavelength band includes the nearby Si XI emission line at 30.33 nm. Due to this contribution, during AR observation, 20% of the total irradiance is detected from the Si XI line (Thompson & Brekke, 2000).

For more detailed information on instrumentation of both the *Solar Dynamics Observatory* and the *Atmospheric Imaging Assembly*, see Pesnell et al. (2012) and Lemen et al. (2012).

2.4 Other Solar Activity Proxies

In this section, we summarize all the long-term solar activity proxies that we are going to investigate in this study.

- **Sunspot number:** Traditionally, this number is widely considered to be the most important solar activity proxy due to the existance of nearly continuous 300 year-long observations. Wolf (1850) introduced the relative sunspot number as follows:

$$R = k(10 \times N_{\mathrm{G}} + N_{\mathrm{S}}), \qquad (2.1)$$

where N_{S} is the total number of sunspots, N_{G} is the number of sunspot groups, and k is a scaling coefficient which aims to equalize the individual observing differences between different observers. This R quantity, called the *Wolf relative sunspot number*, is an artificial, non-physical measure. For this reason, the sunspot number has been modified and corrected several times (Clette et al., 2015). For our research, we utilized the WDC-SILSO number from the Royal Observatory of Belgium. All the sunspot data used here in this Thesis are provided by the website of the Sunspot Index and Long-term Solar Observation, Royal Observatory, Belgium (http://sidc.be/silso/home).

- **Sunspot area [SA]:** SA estimates the physical quantity of area covered by sunspots. The outer boundary of a sunspot and the edge between the umbral and penumbral area are determined with respect to the solar irradiation (Krivova et al., 2007). A systematic sunspot area detection programme was built up between 1874 and 1976 by The Royal Greenwich Observatory (Willis et al., 2016). This series presented information on both the position and the area of sunspots on a daily basis from six observing stations. After 1976, the Debrecen Heliophysical Observatory maintained the detection of SA based on *SDO/HMI* measurements (Győri et al., 2017). The data is collected from the website of the late Debrecen Heliophysical Observatory (http://fenyi.solarobs.csfk.mta.hu/en/databases/SDO/).

- **10.7 cm radio flux:** A bright emission from the upper chromosphere and the lower corona (Tapping, 1987). Sources of this emission are the gyroresonance from thermal plasma trapped by the magnetic field, and the bremsstrahlung of thermal plasma over active regions (Kundu 1965; Krueger 1979). There is a widely known correlation between the 10.7 cm radio flux and the sunspot number. This emission is observed and integrated over the disk and the data are made available by the Dominion Radio Astrophysical Observatory, National Research Council of Canada (`http://www.spaceweather.gc.ca/solarflux/sx-en.php`).

- **global p - mode frequencies:** With six base stations all around our Globe, the Birmingham Solar Oscillations Network (BiSON) measures the line-of-sight velocity of the solar surface (Chaplin et al., 1996) (`http://bison.ph.bham.ac.uk/`). The observations are disc-integrated, so-called Sun-as-a-star observations, which are sensitive to low-ℓ p-mode oscillations, where ℓ is the degree of an eigenmode. The helioseismic data are divided into 182.5-day time intervals and the frequency shift of each individual global acoustic mode is calculated for $0 \leq \ell \leq 2$ and $2400 \leq \nu \leq 3500$ μHz.

- **SDO/AIA 9.4 nm radiation:** This is an optically thin, EUV intensity line. Emission is generated by the Fe XVIII ions at around 6 MK. The 94 Å channel of *SDO/AIA* maps these Fe XVIII ions in the solar corona at every 12 s with a cadence of 0.6 arcsec ($\approx$ 435 km) (Lemen et al., 2012).

2.5   Applied Methods

In this section, all of the tools and methods are listed, which were applied during the carried out research.

- **Python**: This high-level, general-purpose programming language was architectured with a dynamic type system and automatic memory management in favour of code readability in 1991. Due to its free and open-source design, the application of this language started to rise dynamically. The developer community rapidly increased the library of packages for scientific research. To store, manipulate and visualise the quickly expanding amount of data about the Sun, a small group of scientists began to develop the Python environment of *Sunpy* from 2011 (SunPy Community et al., 2015). The Python library is based on several core packages such as Numpy, SciPy, and Matplotlib.

- **Clusterisation**: Cluster analysis or clustering is the task of grouping a set of objects in such a way that objects in the same group (called a cluster) are more similar (in some sense) to each other, than to those in other groups (clusters). It is a main task of exploratory data mining, and a common technique for statistical data analysis, used in many fields, including machine learning, pattern recognition, image analysis, information retrieval, bioinformatics, data compression, and computer graphics. Cluster analysis itself is not one specific algorithm, but is a general task to be solved (Bailey, 1994). For the current research present in this Thesis, the clusterisation module of the *Scikit-Learning* library was applied (Pedregosa et al., 2011).

- **Wavelet analysis**: Wavelet analysis is an appropriate tool to find different periodicities with non-stationary power in the evolution of a given signal (Daubechies, 1990). The reason behind using wavelet analysis rather than Fourier analysis is to identify the temporal variation of dominant oscillation peaks. For more details on wavelet analysis relevant to the current context, see, Torrence & Compo (1998) providing a practical introduction and description of the application of wavelet analysis through meteorological examples.

Chapter 3

Long-term Variation of Macrospicules

Abstract

In this chapter, five physical properties of MS, such as maximum length, maximum width, maximum area, average velocity, and maximum area, were studied over the period of 7 years. The characteristic parameters of the physical properties were estimated with log-normal distribution fitting and the obtained information in histogram format was compared to the measurements of previous studies. The cross-correlations of the physical properties did not indicate any relevant correlation between them but, instead, revealed a strong oscillation pattern in the raw datasets. Strong evidences were found for nearly two-year-long oscillations in the long-term variation of the physical properties of MS. Furthermore, MS seemed to provide analogous behaviour to solar activity proxies after a direct examination.

3.1 Characteristics of the Individual Jets

In Section 2.2, we have discussed how several physical properties of MS have been measured during their entire lifetime. For analysis, four physical properties were estimated for each *SDO/AIA* observation during the lifetime of the jet. Examples for the temporal variation of all the physical properties during MS lifetime are provided in Figure 3.1 and Figure 3.2. The actual height and width of jets increase in their early phase of the lifetime then reach one or more local maxima and decrease. The end of the lifetime of a MS was considered when the top point of the jet fell beneath the limb. From this moment, no visible information could be collected about the jet anymore. Hence the plane of sky area was derived from the actual height and width. The maximum values of these parameters were chosen for further study: maximum length, maximum width and maximum area. Amongst all the physical parameters, the estimated velocity is the most uncertain as seen in Figures 3.1 and 3.2. The reason for this uncertainty is the "hand-picking mechanism" and the method of calculation of the velocity. In order to mitigate the effect of this uncertainty, the average of the absolute value of the all the actual velocities was calculated and utilized for further statistical investigation as average velocity.

3.2 Validation of the Database

Before digging deeper into the dataset to gather new information about the long-term evolution of macrospicules, the validation of the legitimacy of the current criteria system is inevitable. A practical way for accomplishing this goal is to compare the characteristic parameters of the present study to the ones already available in the literature. In Chapter 1.3 we have already described the methods of MS studies used in past studies that are wide-spread and sometimes contradict each other. Only those studies have been selected for comparison which investigated MS in the He II 30.4 nm absorption line or are presented with a full description of the extent of the examined jets.

For establishing a correlation, the histogram of each physical property of the current dataset is analysed by neglecting their temporal variations.

Table 3.1: Preferences of the Fitted Log-normal Distributions

	Mode[1]	Mean[2]	Median[3]	Distributions		
				$1\,\sigma$	$2\,\sigma$	$3\,\sigma$
Maximum length [Mm]	24.95	28.07	26.99	$20.39 - 35.72$	$15.41 - 47.27$	$11.64 - 62.56$
Lifetime [min]	15.27	16.93	16.36	$12.5 - 21$	$9.7 - 27.61$	$7.46 - 35.87$
Maximum width [Mm]	3.95	4.98	4.61	$3.11 - 6.83$	$2.1 - 10.1$	$1.41 - 6.83$
Average velocity [km s^{-1}]	59.62	73.25	68.39	$47.22 - 99.05$	$32.6 - 143.46$	$22.51 - 207.77$
Maximum area [Mm^2]	69.01	97.787	87.06	$53.77 - 140.97$	$33.2 - 228.26$	$20.5 - 369.61$

[1] **Mode** is the value, which is appearing most frequently in the probability density function (i.e. the global maximum of the fitted function).

[2] **Mean** is the arithmetical mean of the fitted function.

[3] **Median** is the value, which separates the lower half dataset from the higher half.

Table 3.2: Comparison of the Literature of the Macrospicules

	Bohlin et al. (1975)	Labonte (1979)	Dere et al. (1989)	Habbal & Gonzalez (1991)	Georgakilas et al. (1999)
Length [Mm]	6.24 − 19.45	6.24 − 25.67	3.9 − 17.9	11.5 − 38.5	12 − 15
Lifetime [min]	8 − 45	4 − 24	≥ 3	10 − 45	5 − 12
Upward velocity [km s⁻¹]	10 − 150	≤ 60	20 − 50	DNP[1]	50 ± 10
Width [Mm]	3.6 − 10.9	2.2 − 6.5	DNP[1]	8 − 20 arcsec	DNP[1]
Spectral domain	He II (30.4 nm)	Hα (656.2 nm)	C IV (154.8 nm)	4.8 GHz (6.24 cm)	He II (30.4 nm)
log of temperature [K]	4.9	4	5	3	4.9
Number of MS	~25	32	10	≤ 10	25
Spatial resolution [arcsec]	2	0.5	2	4	5
Temporal resolution [s]	≥ 180	~60	20, 60	240	12

	Kamio et al. (2010)	Kayshap et al. (2013b)	Bennett & Erdélyi (2015)	New Results
Length [Mm]	40	100	14 − 68.46	20.39 − 35.72
Lifetime [min]	30	≤ 10	2.7 − 30.6	12.5 − 21
Upward velocity [km s⁻¹]	130 ± 30	~95	54.1 − 335.5	47.22 − 99.05
Width [Mm]	26	3.6	3.1 − 16.1	2.1 − 10.1
Spectral domain	He II (25.63 nm)	He II (30.4 nm)	He II (30.4 nm)	He II (30.4 nm)
log of temperature [K]	4	4.9	4.9	4
Number of MS	1	1	101	301*
Spatial resolution [arcsec]	5	1.5	1.5	1.5
Temporal resolution [s]	6000	12	12	12

[1] **DNP:** data not provided.

* Size of the dataset at the time of the publication of Kiss et al. (2017).
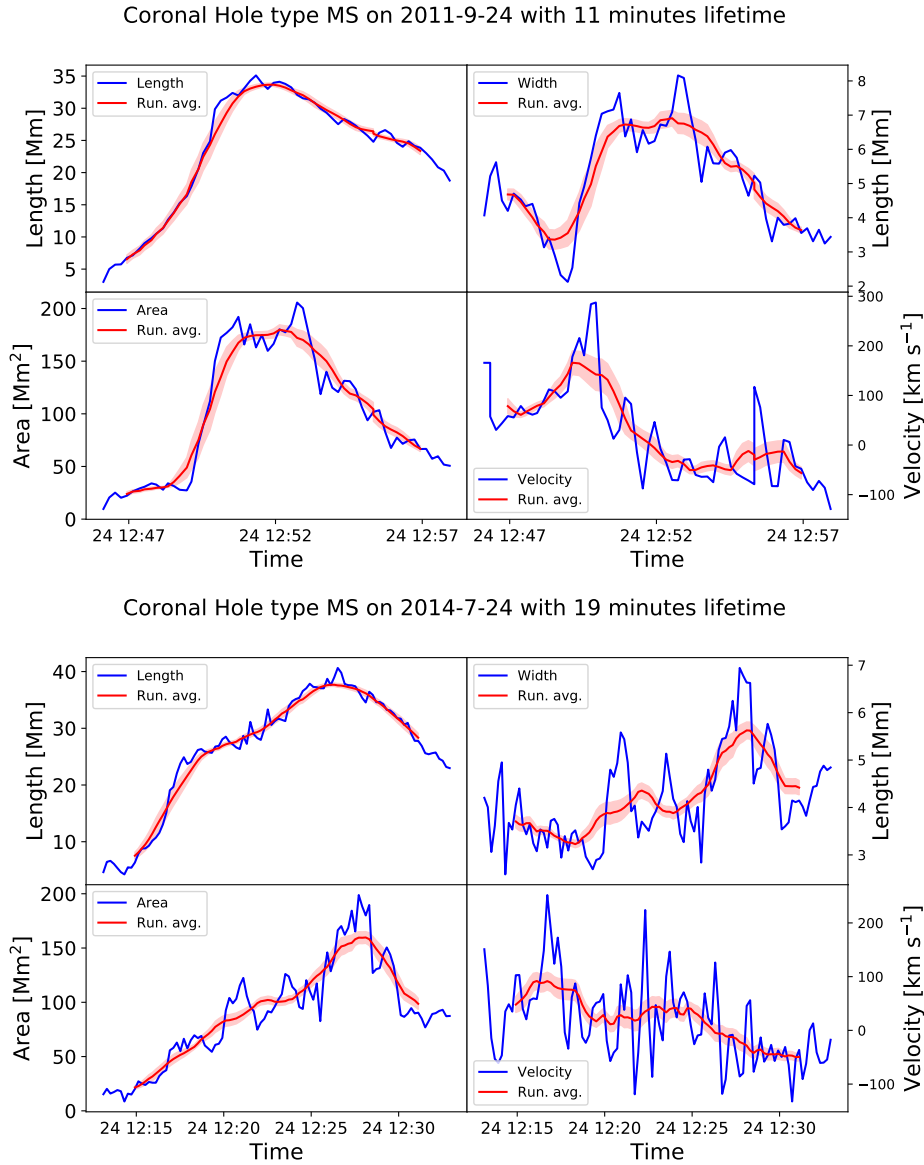
Figure 3.1: Temporal distribution of four physical properties. Each four-panel plot refers to a macrospicule. Top left-right, bottom left-right panels: height-width-area-velocity. Blue lines represent the raw data, red lines indicate the running average with window size of $\approx 10\%$ of the temporal length of the set.

These histograms were plotted with solid black lines on the right-hand side panels of Figures 3.3–3.7. After test fittings, several continuous probability distribution functions, the log-normal distribution (alternatively,
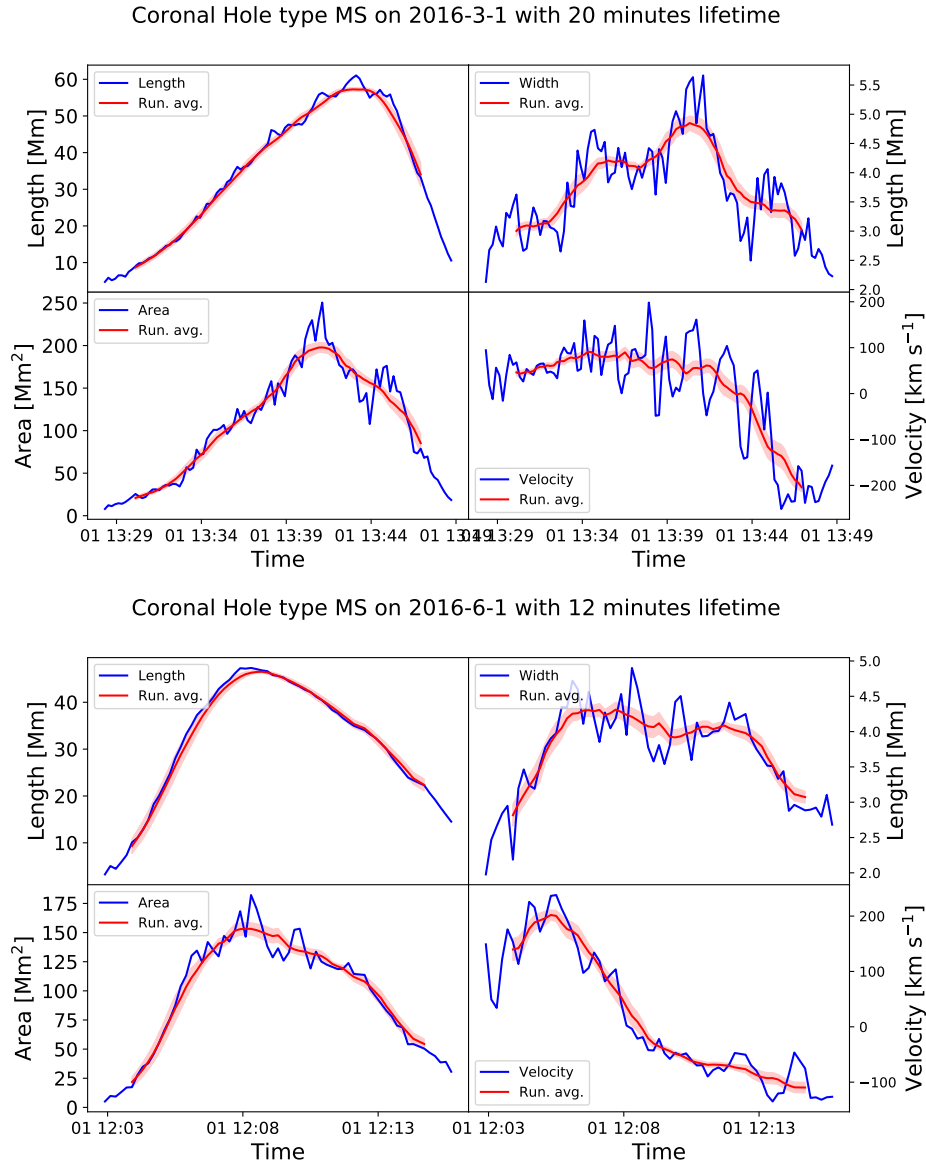
Figure 3.2: Temporal distribution of four physical properties. Each four-panel plot demonstrates a macrospicule. Top left-right, bottom left-right panels: height-width-area-velocity. Blue lines represent the raw data, red lines indicate the running average with window size of $\approx 10\%$ of the temporal length of the set.

Galton distribution) provided the best possible fit. The probability den-

sity function of the log-normal distribution:

$$f(x; \mu, \sigma^2) = \frac{1}{x\sigma\sqrt{2\pi}} \exp\left(-\frac{(\ln x - \mu)^2}{2\sigma^2}\right) \qquad (3.1)$$

where μ and σ are the mean and the standard deviation of the natural logarithm of the variable, respectively (Crowl & Kunio, 1988). The fitted log-normal distribution was represented alongside the histogram with a dash-dot continuous line in Figures 3.3–3.7. The mean of each fit was indicated with a dashed line. The white-light and gray-dark gray domains displayed the $1\sigma - 2\sigma - 3\sigma$ deviance from the mean. Table 3.1 summarises the complete coverage of the gained parameters.

The values with 1σ standard deviance from the mean of the fitted log-normal functions have been compared with numerous studies from the literature and summarized in Table 3.2. Regardless of the rather outstanding example of Kamio et al. (2010), the lower height limit found in the earlier studies was somewhat smaller to the recent ones: earlier investigations have not made a distinction of macrospicules from spicules a priority. The characteristic values of other physical properties, such as lifetime, width and area are relatively close in each of these studies. For validation, the physical properties of the subjects of the current research appear to be consistent with the literature of macrospicules.
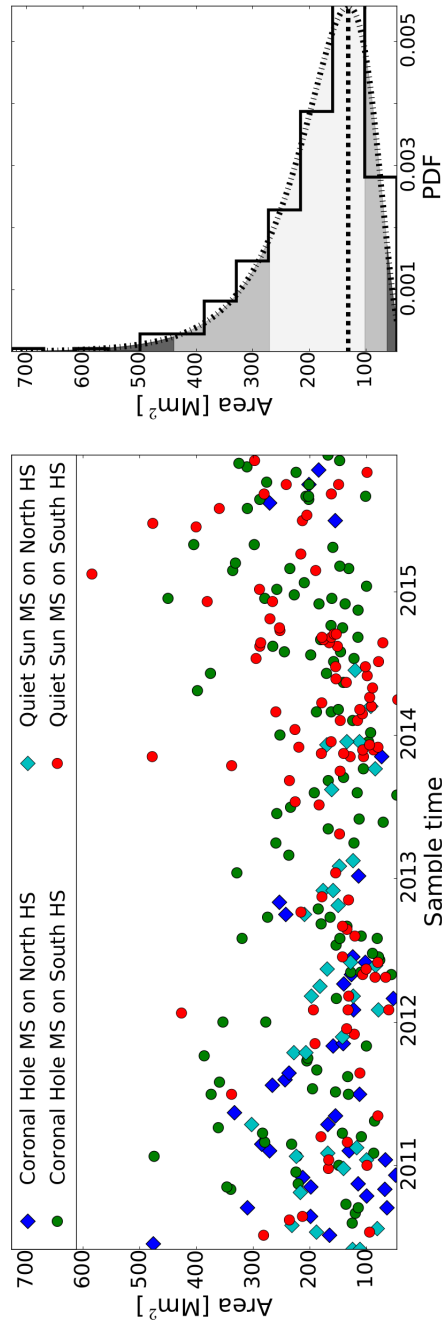
Figure 3.3: Temporal distribution of the maximum area. On the bottom, the distribution of the area can be seen. Different types of marks are used for different hemispheres: diamonds represent the northern hemisphere (dark blue – CH, light blue – QS), circles denote the south (green – CH, red – QS).
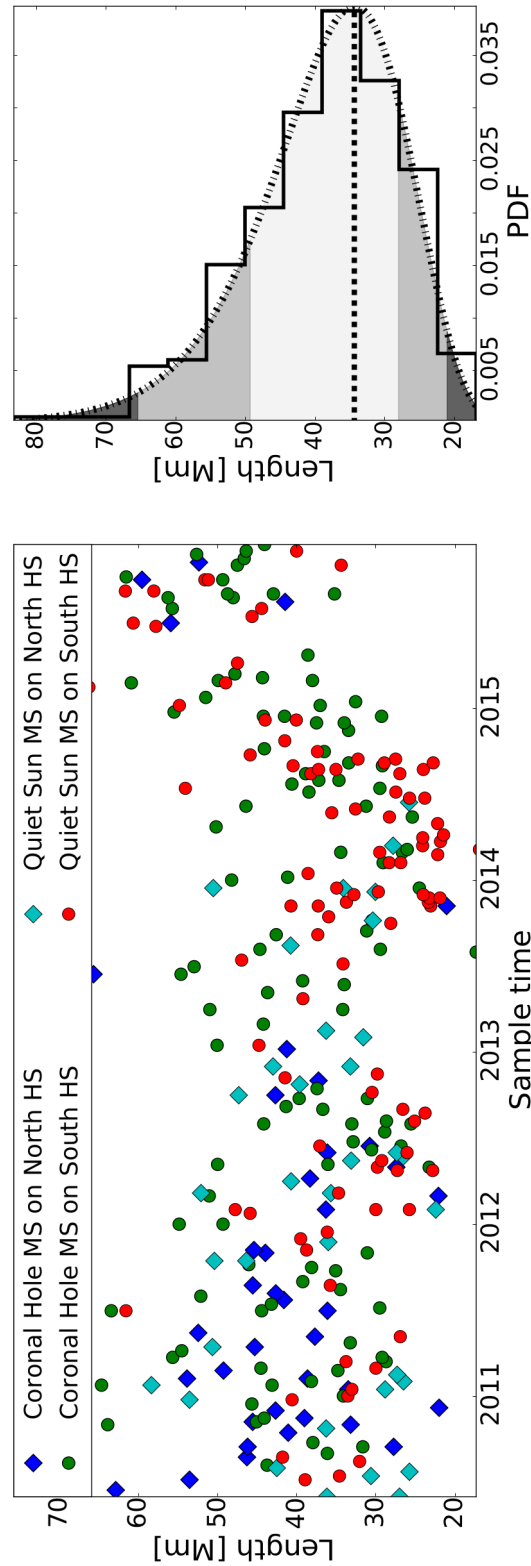
Figure 3.4: Temporal distribution of the maximum length. The notation is the same as of Figure 3.3.
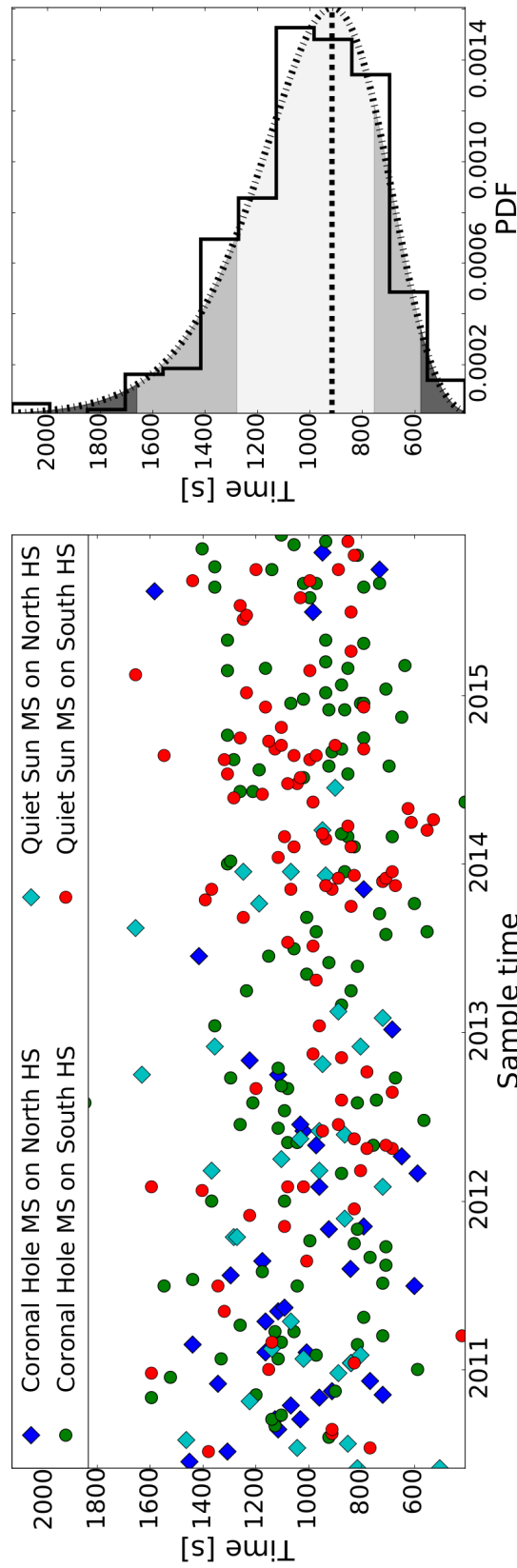
Figure 3.5: Same as Figure 3.3, but for the temporal distribution of the lifetime.
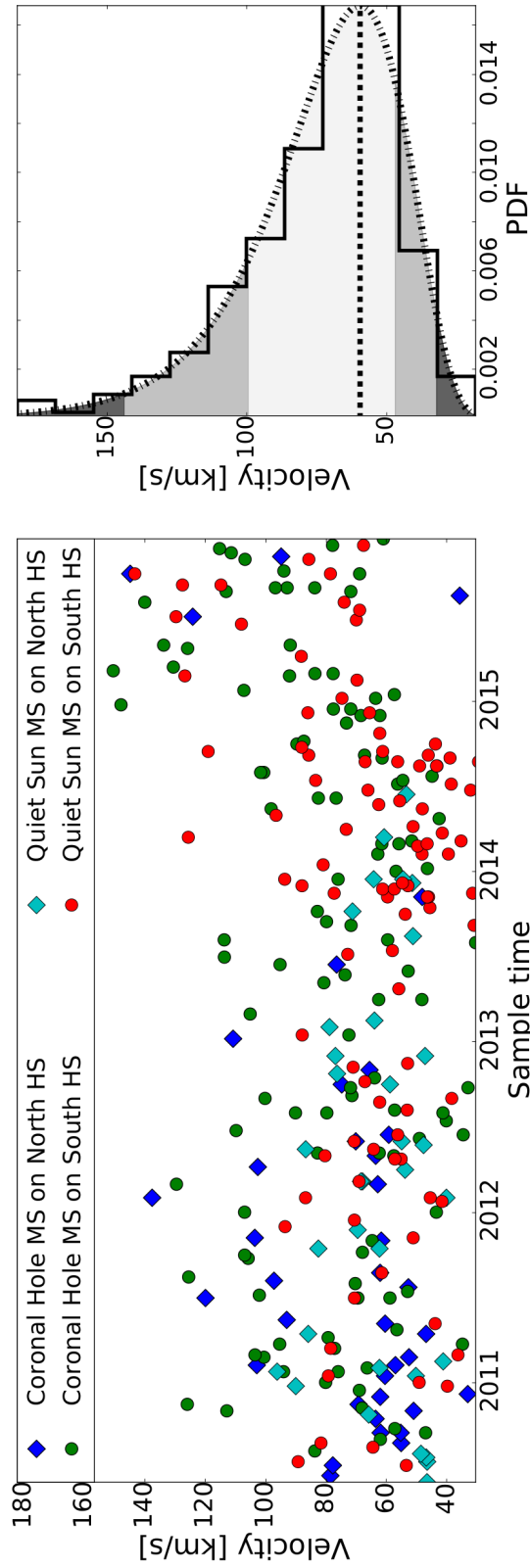
Figure 3.6: Same as Figure 3.3, but for the temporal distribution of the average velocity.
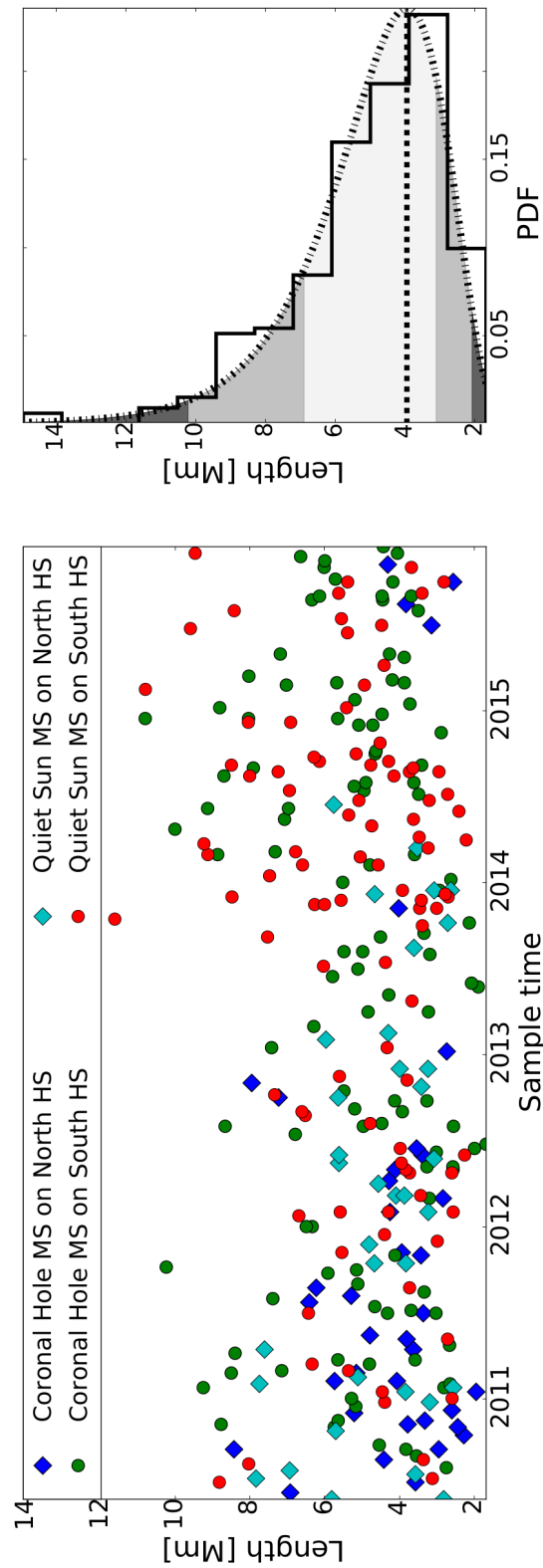
Figure 3.7: Temporal distribution of the maximum width. The notation is the same as of Figure 3.3.

3.3 Analysis of Macrospicule Properties

The long-term variation of the five physical properties has been displayed in the bottom panels of Figure 3.3 to Figure 3.7. By separating the presented data with respect to the main MS types and hemispheres, no strong temporal variation could be seen in the first approximation. For this reason, the analysis was continued with the cross-correlation of the different physical properties in order to unveal any possible correlation. These cross-correlations are as displayed in Figures 3.8 and 3.9. For each pair of measurements, the correlation coefficient k was estimated. Variables with correlation coefficient of 0.6 are considered to be relevant, i.e. there is a clear relationship. The coefficient is mostly rather low for both CH-MS ($k_{CH} = [-0.29, -0.012, 0.127, 0.131, 0.195, 0.214, 0.557]$) and QS-MS ($k_{QS} = [0.179, 0.355, 0.373, 0.406, 0.58]$). A relatively strong correlation was only determined for the following pairs: "Maximum length vs Maximum area" ($k_{CH} = 0.78, k_{QS} = 0.87$), "Maximum width vs Maximum area" ($k_{CH} = 0.64, k_{QS} = 0.75$) and "Maximum length vs Average velocity" ($k_{CH} = 0.76, k_{QS} = 0.81$). Additionally, "Maximum area vs Average velocity" ($k_{QS} = 0.71$) and "Maximum area vs Maximum lifetime" ($k_{QS} = 0.65$) pairs indicate a stronger correlation for QS-MS only. Several of these stronger correlations seem to be logical, as area data are derived from the length and width. An interesting feature could be seen by averaging the correlation coefficients: $|k_{CH\_avg}| = 0.372, |k_{QS\_avg}| = 0.57$. This difference was also noticed for the ratio of number of strong correlations to all the correlations: $n_{k\_CH} = 3/10$, $n_{k\_CH} = 5/10$. The source of these differences may lie in the underlying governing physical differences between the two types of MS. Equipped with this information we conclude that, the different physical properties of MS did not show a strong relationship in general.

By investigating the large-scale time-dependence (i.e., solar cycle evolution), in this study, an interesting effect is visible. Namely, in Figures 3.8 and 3.9, the change of the marker color represents the passage of time: Red marks represent the value of an MS property around June 2010, and the sequential color variation into blue captures the progress in time. Tracking the variation from red to blue draws a trajectory in each figure, which is a kind of similar to the existence of these different
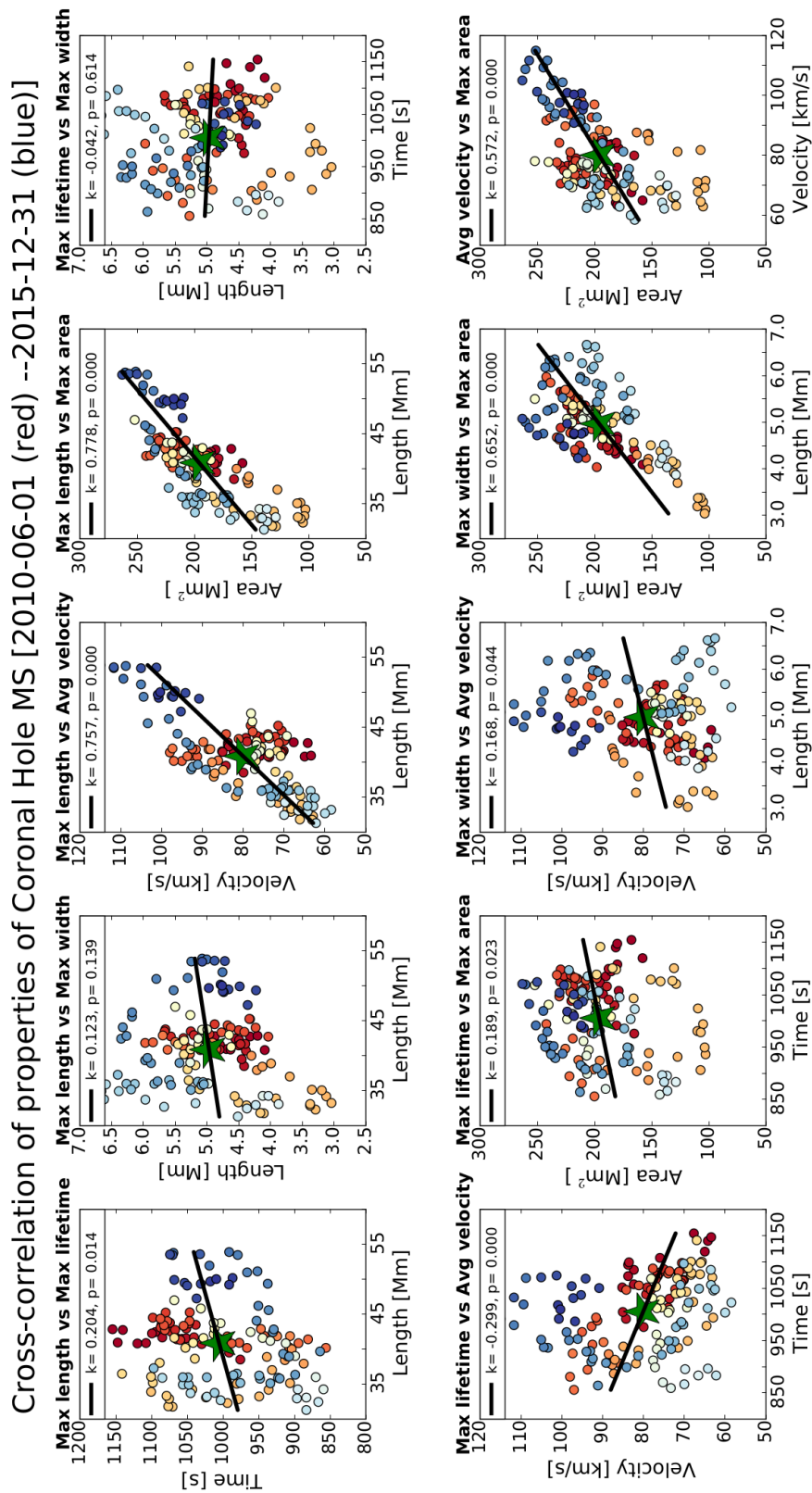
Figure 3.8: Cross-correlation of a range of CH-MS properties. Variation in color of markers represents the progress in time: red indicates the beginning of June 2010, blue denotes the end data December 2015. Green star indicates the weighted geometric center of property for a given plot. Characteristics of a fitted black line is the k correlation coefficient and two-sided p-value obtained in the associated hypothesis test.
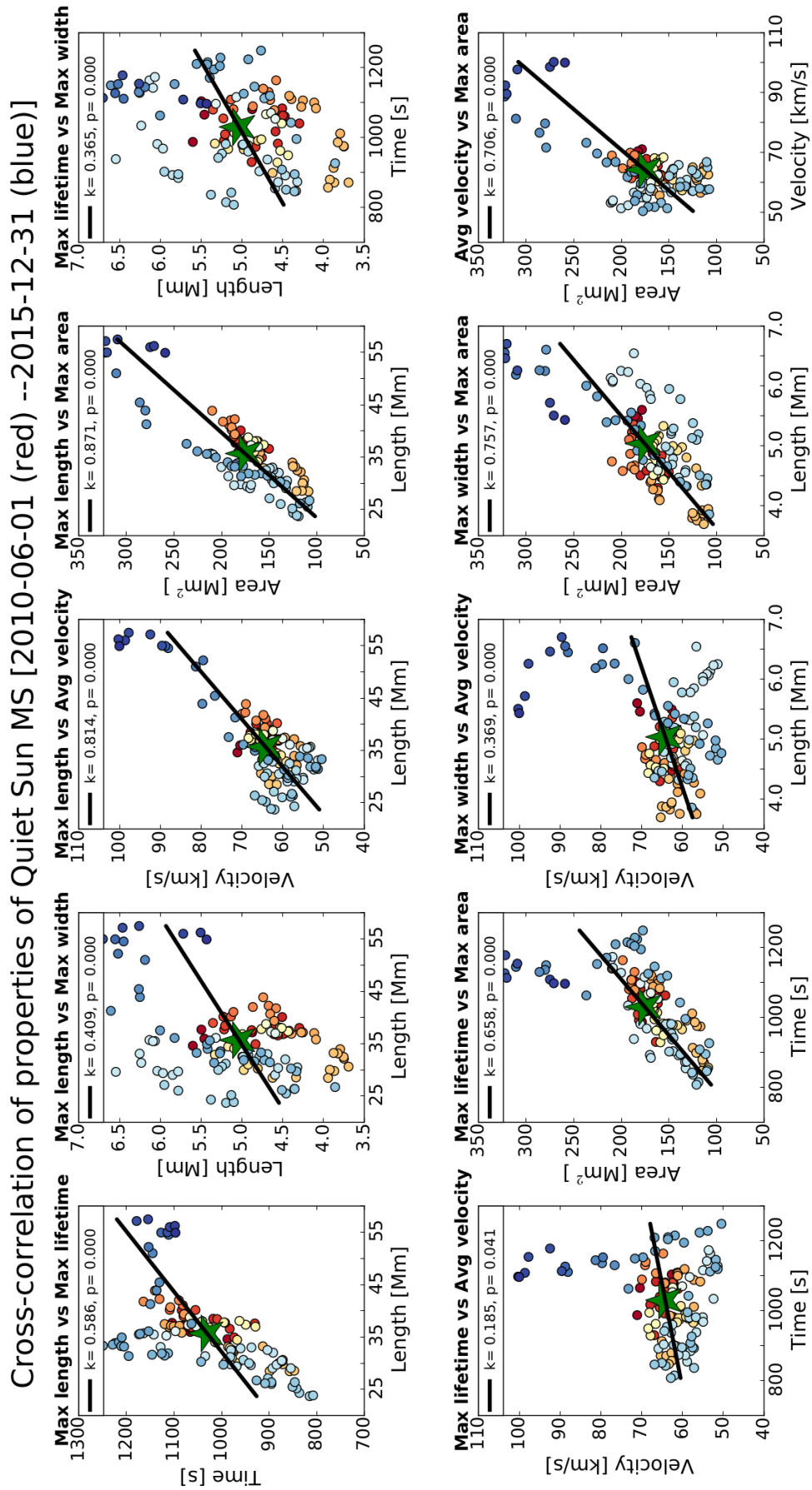
Figure 3.9: Same of Figure 3.8, but for QS-MS properties

branches of the well-known Hertzsprung-Russell diagram (HRD). Stars "migrate" on the HRD on a specific route during their lifetime, when their luminosity or surface temperature changes. MS seem to show a very much alike behaviour. In order to gain further information about the variation in each plot, the entire problem is approximated by a geometrical problem. Every plot was considered as a geometric shape, which is built up by all the points in the plot. The geometric center of this "mass" became the fixed point and is marked as green stars in each panel of Figures 3.8 and 3.9. Therefore, the position of each point of the body was calculated with respect to the fixed point. Figures 3.10 and 3.11 show the distance between the fixed point and all the points of the rest. It is important to note that the actual magnitude and unit, of course, of physical properties is different (e.g., lifetime values are three magnitudes greater, than maximum width values). To avoid any bias caused by such deviance during the approximation of the distance, all the physical properties are normalised. A strong oscillatory pattern, as a result, can be seen in the distance plot with strong peaks of a roughly several-year-long period. After separating the northern hemisphere MS (red marks) from the southern hemisphere MS (green marks), no significant trends or features are visible.

Next, the wavelet analysis of QS-MS reveal a more complex evolutionary pattern. Similarly to the CH-MS, the period at around 2-year appears. However, this peak is most apparent after 2014 and mainly inside the Cone of Influence (CoI). For this reason, more data is necessary here for further investigation. The source of this period could be a strong wave peak in the first half of 2015. This peak appears in each distance plot of QS-MS of the bottom panels of Figures 3.10 and 3.11. Furthermore, a 3-year long periodicity can also be identified in the analysis, with significance for "Maximum width vs Maximum area", "Lifetime and Maximum width", "Lifetime vs Maximum area" and, furthermore, less significantly for nearly all the remaining cases. The most interesting case is the cross-correlation "Lifetime vs Maximum width", where the 0.5-year-long oscillation is the dominant one with a less powerful 1-2-year period peak. In several cases, a strong peak appears during a 2-4 years long domain, but these regions are in the CoI.

3.4 Connection to Other Solar Activity Proxies

Following the analysis of the cross-correlations of MS physical properties, a more detailed study of the raw data was necessary as was conducted in Kiss & Erdélyi (2018). New results were obtained after the second extension of the database. In all the panels of Figure 3.14, the wavelet analysis of the temporal variation of each physical is displayed. In order to remove the noisy nature of the signal, the running average is calculated with a window size of one-month. This time interval is long enough to mask the short-scale noise-like variations of the data. On the other hand, the window is short enough to prevent their influence on long-scale oscillations. These smoothed plots were also added to Figure 3.14.

The distributions of "Lifetime" and "Maximum width" do not show a clear oscillatory pattern, however, a strong oscillatory pattern is visible in the case of "Maximum length", "Average velocity" and "Maximum area". From the left-hand-side of Figure 3.14, one can see that the local maxima of each cycle occurs during the summer of each odd years: 2011, 2013, 2015. This trend suggests a period of around two-years, but a proper signal processing would be required to gain more precise (and with confidence) information about the oscillatory properties of these signals.

The 7-year length of the extended datasets is now sufficiently long enough to provide a power peak with the expected 2-year period outside the CoI. The right panels of each row, in Figure 3.14, show the results of the wavelet analysis. "Lifetime" and "Maximum width" do not show power peaks at around 2-year. However, wavelet analysis of the remaining three properties of MS provides a much more promising outcome. A significant peak appears at around 1.8 years outside the CoI. Oscillations with periods between 1.5 – 2.5 years are often referred as Quasi-Biennial Oscillations – QBOs (Akioka et al. 1987; Benevolenskaya 1998a,b; Broomhall et al. 2009; Penza et al. 2006; Zaqarashvili et al. 2010; Fletcher et al. 2010; Elek et al. 2018). Hence the periods of the oscillations found in the MS fit into the required interval, these signals are also referred as QBOs. These oscillations are more dominant after 2012, hence some parts of these oscillation peaks are inside the CoI.
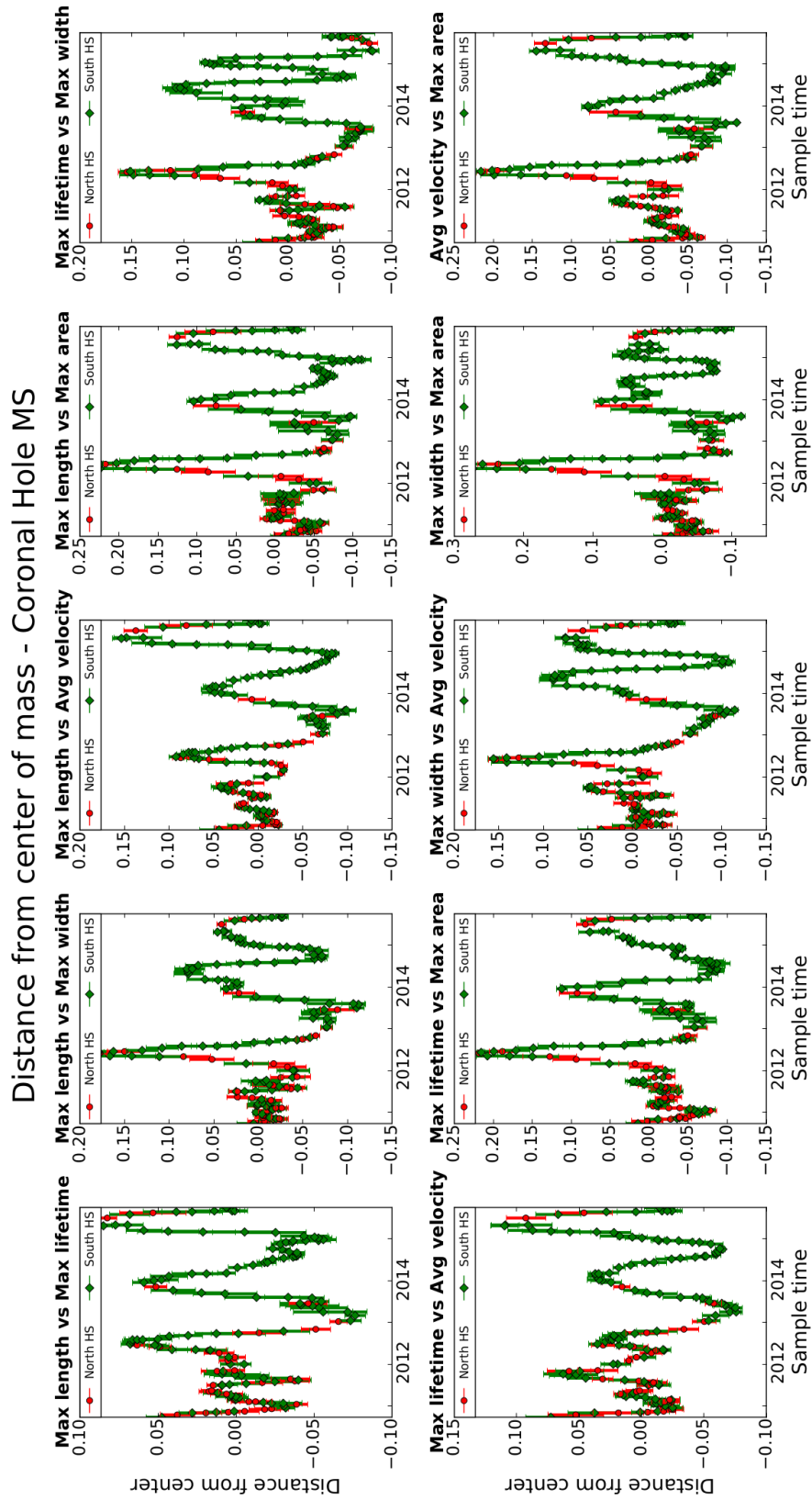
Figure 3.10: Distance plot of each marks in Figure 3.8 from the center of mass. Red points indicates the north hemisphere values, green marks represent MS from south hemisphere
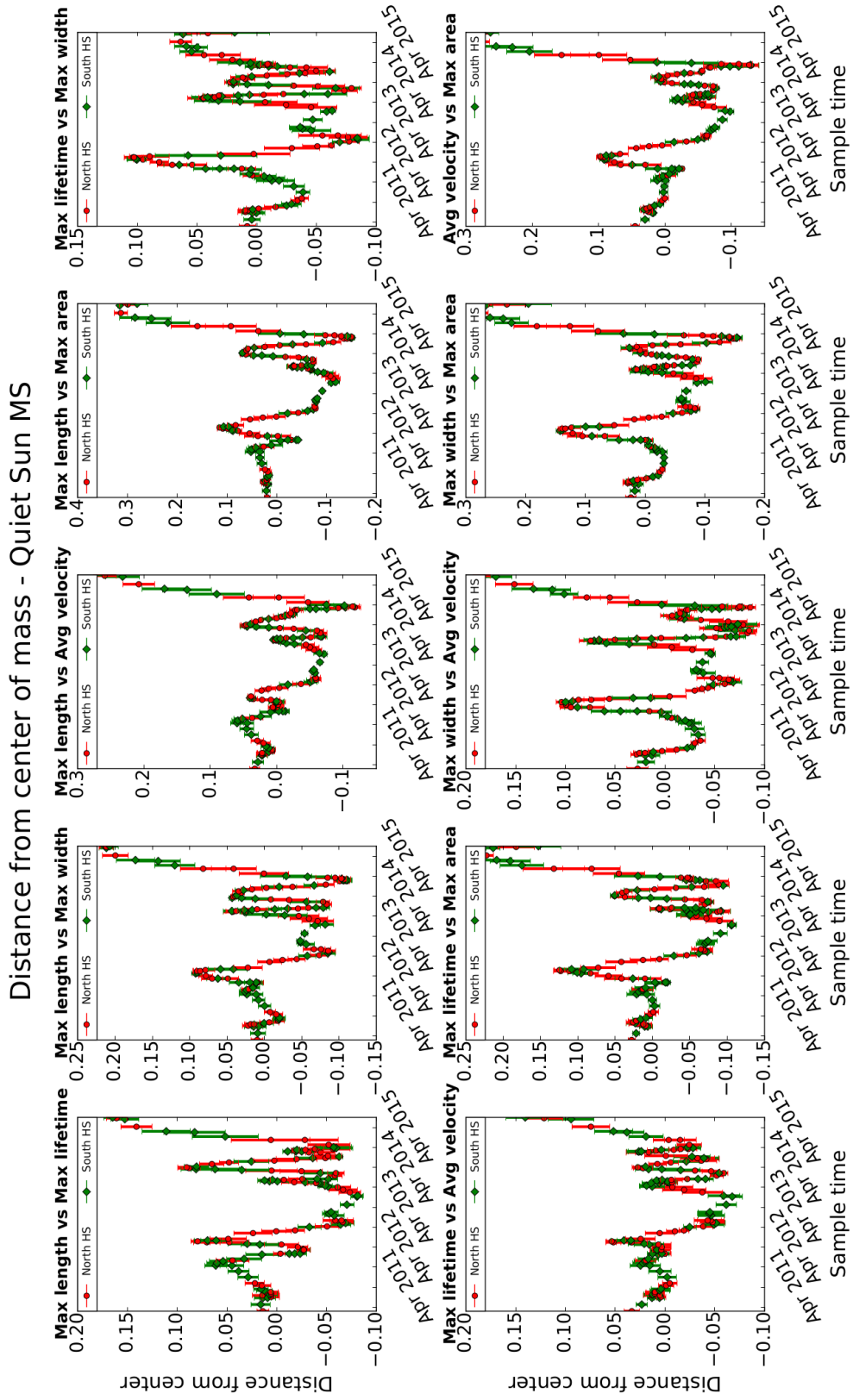
Figure 3.11: Same as Figure 3.10, but for QS-MS.
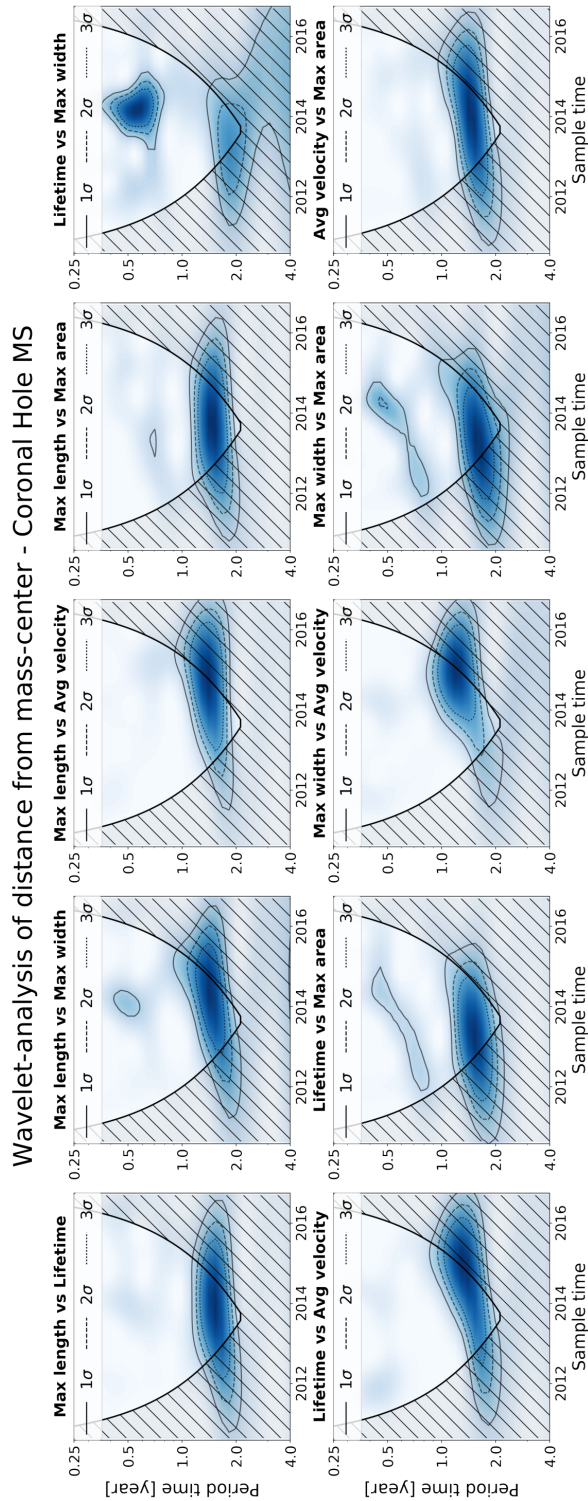
Figure 3.12: Wavelet analysis of the variation of distance from the center of mass for cross-correlated physical properties of CH-MS. The upper two rows are of CH-MS, the bottom two rows of QS-MS. Solid, dashed and dotted contour lines represent the $1\sigma, 2\sigma$ and 3σ deviations from the average. The COI is outlined by a black line and grey filling.
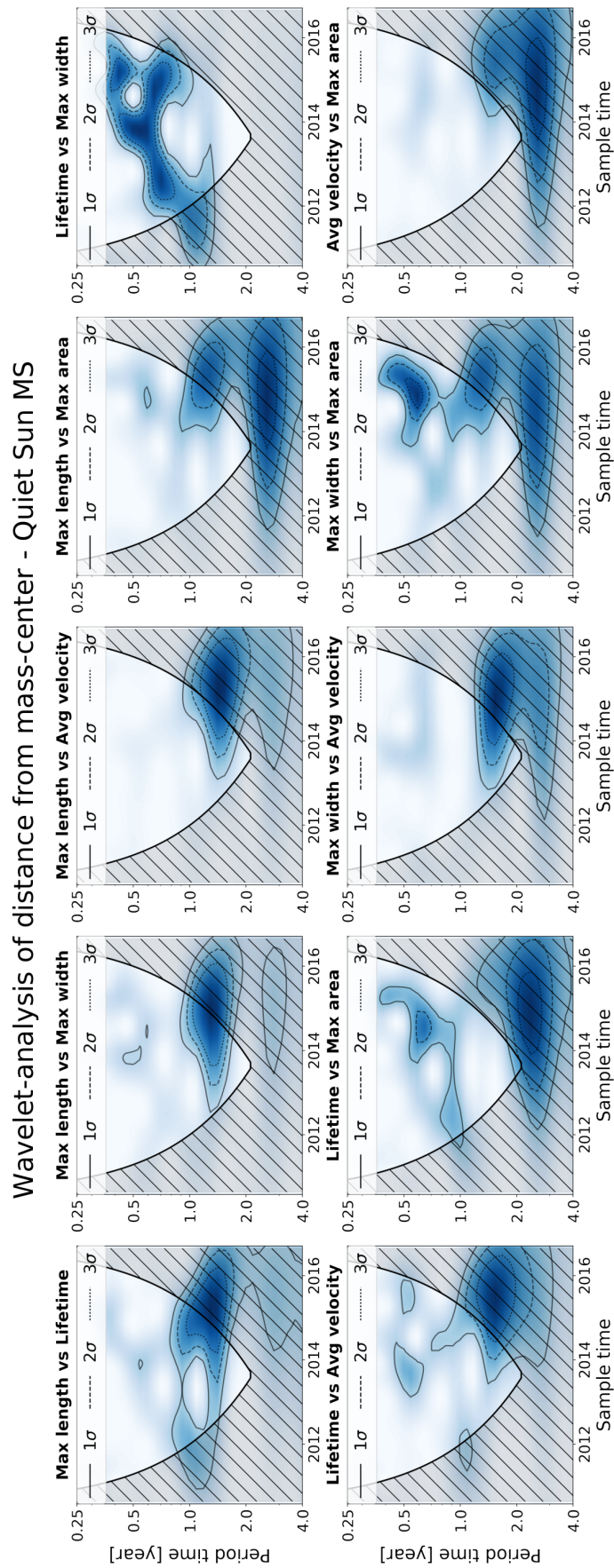
Figure 3.13: Same as Figure 3.13, but for QS-MS.

However, there are highly significant areas of QBOs outside of the CoI. Some power peaks, with shorter periods, are also visible in these figures, but they are not as significant as the QBOs.

The global wavelets confirm the statements made above (see e.g. the right-hand-side of the wavelet panels in Figure 3.14). "Lifetime" does not seem to provide any measurable oscillation peaks, furthermore "Maximum width" shows a more complex global wavelet with several non-significant power peaks. "Maximum length", "Average velocity" and "Maximum area" have clear and significant peaks at about 2-year (outside CoI).

Broomhall & Nakariakov (2015) compared the long-term variation of the global p-mode frequency shift to a few other solar activity proxies for a period between 1985 and 2014: namely, two indicators in the photosphere (i.e. sunspot number, sunspot area), two proxies in the solar atmosphere (i.e. 10.7 cm radioflux, 530.3 nm green coronal index) and two activity phenomena present farther away from the solar surface (interplanetary magnetic field, the galactic cosmic-ray intensity). After the removal of the dominant 11-year long cycle, QBOs were found in each dataset. However, the actual details of these high-frequency oscillations were not compared to each other.

Here, besides highlighting the high-frequency variation of the physical properties of MS, we also shed light on the temporal variations of different QBOs in comparison to each other. For this reason, we have also removed the 11-year cycle from the time series of 5 solar activity proxies (and labelled them with abbreviation in square brackets): the sunspot number $[n_{SN}]$, area $[n_{SA}]$, 10.7 cm radioflux $[\mathcal{F}_{10.7}]$, average channel intensity of SDO/AIA 9.4 nm $[I_{SDO}]$ and the p-mode frequency shift $[d_p]$. The residual data, after removing the solar cycle trend, are plotted in the bottom two panels of Figure 3.15. The trend removal was executed in the following way: a smoothing was utilized with a large windowsize (nearly 2.5 years), which has removed shorter-scale fluctuations but preserved the 11-year cycle. The smoothed graph clearly shows the 11-year oscillation. Next, this smoothed graph is extracted from the original dataset, and the residual is shown in the middle and bottom panels of Figure 3.15. All the SDO channels present QBO patterns, however, the 9.4 nm channels provide the most similarities to other solar activity proxies. "Maximum

Table 3.3: Dates and Errors for Extrema of the Three MS Properties

	Maximums			Minimums	
No.	Date	Error	No.	Date	Error
I.	24.06.2011	$\pm$ 28 days	II.	15.07.2012	$\pm$ 35 days
III.	24.05.2013	$\pm$ 84 days	IV.	15.03.2014	$\pm$ 56 days
V.	01.06.2015	$\pm$ 49 days	VI.	07.04.2016	$\pm$ 37 days

length", "Maximum area" and "Average velocity" of MS, reveal QBOs, that are clearly visible in the top panel of Figure 3.15. The duration of the MS dataset allows to carry out this study now between June 2010 and July 2017.

In the next step, we compare the oscillatory signatures of the MS data to other solar proxies. Local extrema (minima and maxima) can be determined for each MS datasets. To find the epochs of all the MS extrema, the dates of the local extrema of the "Maximum length", "Maximum area" and "Average velocity" datasets were averaged (solid vertical lines for maxima and dashed vertical lines for minima in Figure 3.15) and their standard deviations (gray vertical bars around the lines Figure 3.15) were estimated from error analysis. Dates for all MS extrema are given in Table 3.3 (labeled with Roman numbers I–VI). The dates of the extrema clearly indicated supporting evidence for the 2-year long oscillation, only the minima in 2014 may seem to be somewhat early.

In the following, we now compare these extrema with those of the other solar proxies:

I: this maximum is close to one of the maxima of n_{SN}-n_{SA}-$\mathcal{F}_{10.7}$, though, not matching them really well. With a good approximation, however, they are *in-phase*. I_{SDO} and d_p are in their rising phase.

II: this minimum occurs around at the time, when there is a small "step" in each of the other proxies.

III: this maximum is matching the local minimums of all other proxies. They are clearly *out-of-phase*.

IV: this minimum happens at the same time, when there is a local maximum in the n_{SN}-$n_{\mathrm{SA}} - d_p$ variations. In the case of $\mathcal{F}_{10.7}$ and I_d, IV also marks the local maximum, however, these variables have a smaller secondary maximum. Overall, they are all *out-of-phase*.

V: this maximum is similar to that of I. At this epoch, n_{SN}-n_{SA} are around their local minimum, but the matching is not perfect. $\mathcal{F}_{10.7}$-I_d is in its decaying phase from their secondary maximum, closing up to the minimum. Overall, they are all *out-of-phase*.

VI: Close to the epoch of this minimum, a small-scale maxima is visible on the n_{SN} - n_{SA} - $\mathcal{F}_{10.7}$ - I_{SDO} plots.

For the six extrema of the MS properties, four of them are in- or out-of-phase with the other solar proxies. Only at II there is no extrema, but a "step" is still visible in all the other proxies. This may suggest a change in the underlying process: before this time, I is *in-phase* with the other proxies and after this time, III is *out-of-phase* with other proxies.

To corroborate this *out-of-phase* behaviour, we implement a cross-correlation analysis between the three MS time-series and the five solar activity proxies as seen in Figure 3.16. If this *out-of-phase* behaviour is present in the data, anti-correlation should be found on the cross-correlation plots. Linear regression is utilized to analyse the correlation between every combination of them. By taking into account the entire time-span of the data-series, no strong anti-correlation is found (the average of r^2 values is -0.218). By considering the data points only after May 2013 (the epoch of III), the anti-correlation between the MS properties and the solar proxies is significantly stronger (the average of r^2 values is -0.3895). In 13 cases out of 15 cross-correlations, the absolute value of the correlation coefficients is larger. Figure 3.16 clearly shows that the blue points (data values before May 2013) are robustly vertical, which weakens the correlation coefficient and, thus, the anti-correlation. This is supporting evidence for the previously discussed out-phase nature.

However, for a more detailed investigation of these variations of extrema, longer data would be needed. Therefore, this analysis may be a promising motivation for investigation in the future.
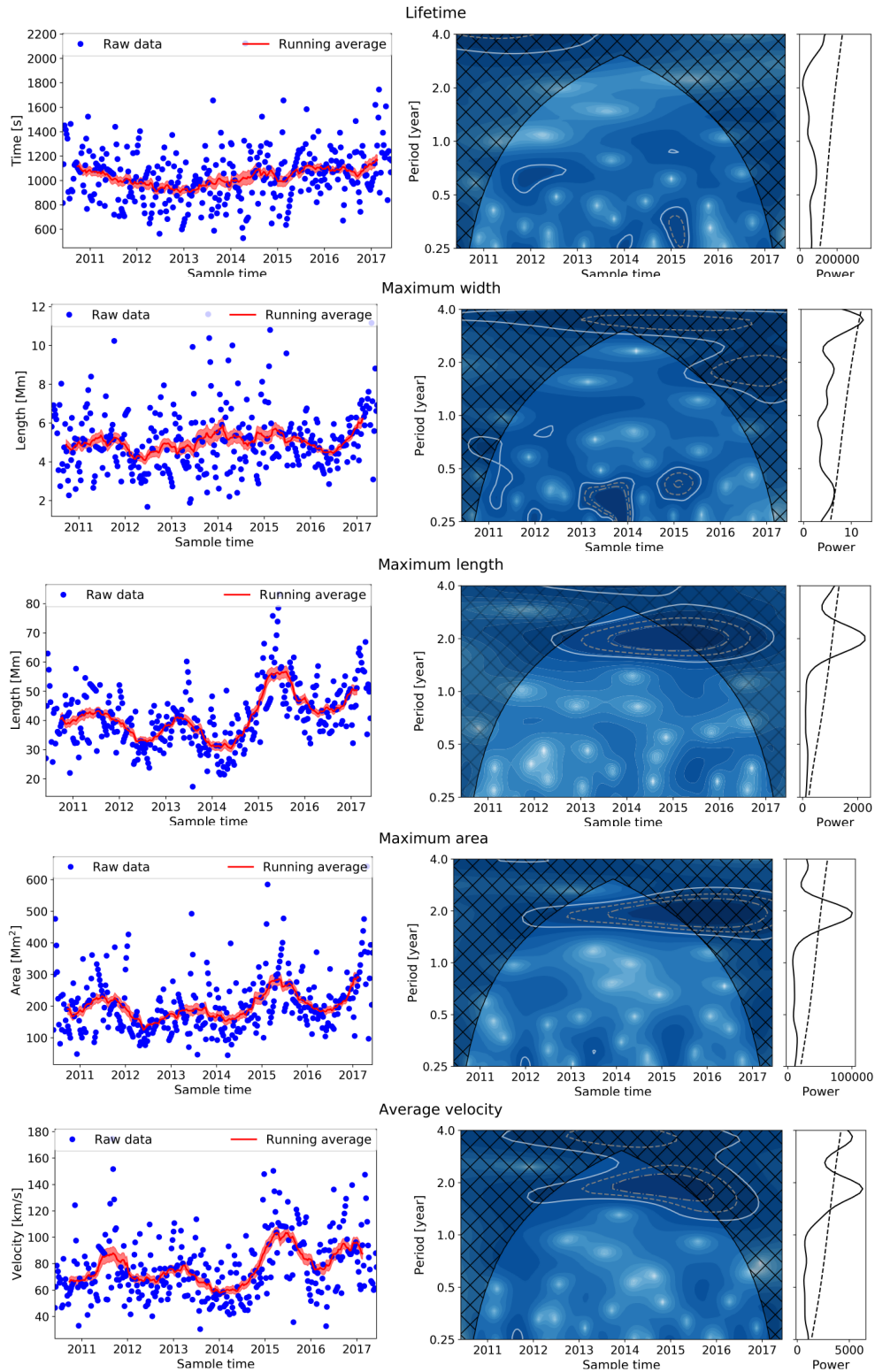
Figure 3.14: On the left in each row, raw data of the properties of MS are marked with blue dots and their running-average is highlighted with red dots with error bar. On the right, wavelet analysis of the row data of the five investigated physical properties of MS are shown. Solid, dashed and dotted contour lines represent the $1\sigma, 2\sigma$ and 3σ deviations from the average. The COI is bounded with a black line and filled with hatches. Attached to each wavelet on their right, the global wavelet power is seen.
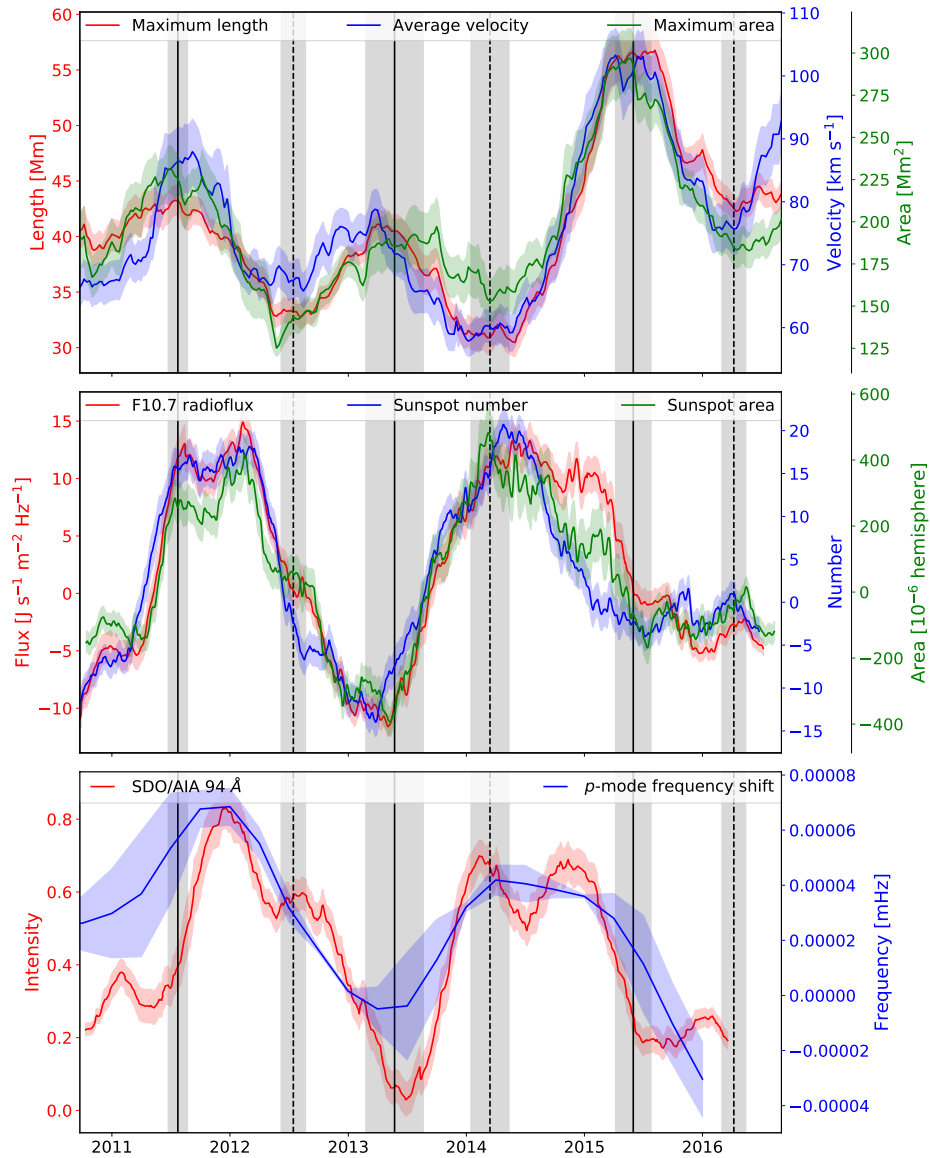
Figure 3.15: QBOs in various parameters of solar activity phenomena. The top panel contains three MS properties, which indicate QBOs: maximum length (red solid line), average velocity (blue solid line), maximum area (green solid line). In the middle panel, 10.7 cm radioflux (red solid line), sunspot number (blue solid line) and sunspot area (green solid line) are plotted. *SDO/AIA* 9.4 nm intensity (red solid line) and the *p*-mode frequency shift (blue solid line) are showed. Coloured, partially transparent, areas around each line indicates the error. Maximum and minimum dates of MS variables are represented with black vertical lines: solid vertical lines reveal the time of the maximums, dashed vertical lines illustrate the time of the minimums. Gray bars around the vertical lines demonstrate the error of the extrema.
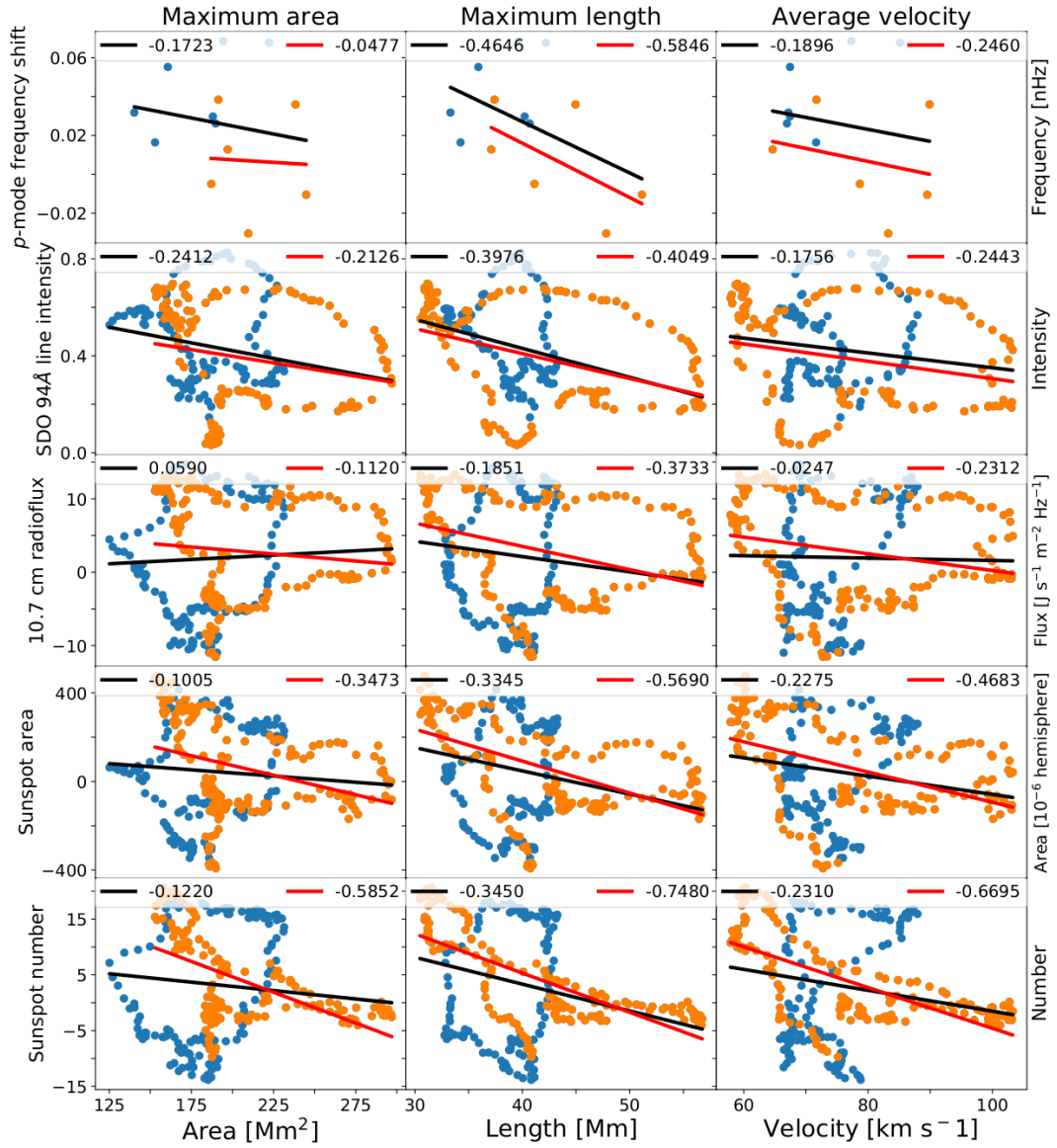
Figure 3.16: The cross-correlations between the three MS properties and the five solar activity proxies. In each panel, blue and orange data points represent, together, the entire time-span. The solid black line shows linear correlation between the datasets and the corresponding r^2 value can be found on the LHS of legend. Orange points demonstrate the data taken after May of 2013. Their linear correlations are displayed by red lines with r^2 values on the RHS of the legends.

3.5 Conclusions

In this Chapter, we focused on the investigation of the long-term variation of properties of chromospheric jets, the macrospicules.

Distributions of MS properties in time show a strong temporal variation. To have accurate estimates for the average properties, the temporal variation was put aside and their histograms were studied initially. Each histogram was fitted with a log-normal distribution and their preferences (e.g. mode, mean, median, distribution) were determined to characterise the MS. Comparing our findings to those of the previous studies (note, that values here are 1σ distribution of the log-normal distributions) we conclude that: lifetime (16.75 ± 4.5 min), width (6.1 ± 4 Mm), average velocity (73.14 ± 25.92 km s^{-1}) values are in an agreement, while length (28.05 ± 7.67 Mm) is slightly greater. Correspondence between the results found in this research and those in the literature verify the choice of the tetragon assumption.

Last but not least, cross-correlation of the raw data was investigated. After linear fittings on each cross-correlation distributions, there is often a lack of a dominant correlation ($|k_{\mathrm{CH\_avg}}| = 0.372, |k_{\mathrm{QS\_avg}}| = 0.57$). In three cases, however, the coefficients are found to be relatively strong for both types of MS. For QS-MS, further two combinations of physical parameters (e.g. "Maximum area vs Average velocity" and "Maximum area vs Maximum lifetime") show a stronger correlation, which may reveal the underlying physical differences between the formation of CH-MS and QS-MS. Considering the temporal evolution of these distributions, remarkable paths became visible in cross-correlation visualisations. To study this behaviour, the distances between the center of mass and each points were determined. These distance plots in time reveal a strong, previously unseen temporal variation in the database.

The full length of this dataset enables us to study more comfortably periodicities present in the property signals of MS at around the period of two-year, the so-called Quasi-Biennial Oscillations. To find such periodicities in the five time-series of MS properties ("Maximum length", "Maximum width", "Maximum area", "Average velocity", "Lifetime"), wavelet analysis was applied. A study comparing QBOs present in the properties of MS to the five additional solar activity proxies (namely,

sunspot number, sunspot area, 10.7 cm radioflux, *SDO/AIA* 9.4 nm intensity, *p*-mode frequency shifts) was carried out as well. For the period of June 2010 to July 2017, six extrema (local minimum or maximum) were identified in the QBOs of MS (labelled with I–VI) in Figure 3.15. To have a deeper understanding of these QBOs, we compared directly the QBOs of MS to the QBOs of other solar activity proxies. All of the extrema indicate a local change of trend in the solar proxy oscillations. Five of them [I, III, IV, V, VI] are close to a local minimum or maximum of the solar proxy QBOs. Furthermore, III and IV are matching with high accuracy the local extrema of the solar proxy plot.

Another interesting feature is that I is *in-phase*, III-IV-V-VI are *out-of-phase* with the activity proxies. The shift between the phases may take place during the epoch of II, where there is no extremum in the activity proxies, but a slight trend-breaking "step" is also visible. This *out-of-phase* behaviour is also corroborated by a cross-correlation analysis. The linear regression shows a weak anti-correlation between the three MS properties and the five solar activity proxies during the studied time-span ($r^2 \sim -0.2$). However, the cross-correlation of data taken after May 2013 (the epoch of III) presents a stronger anti-correlation ($r^2 \sim -0.4$) as seen in Figure 3.16.

This analysis indicates a possible connection between solar proxies, hence the high-frequency oscillatory component of the magnetic field, and the locally driven macrospicules.

Chapter 4

Spatial distribution

Abstract

In this chapter, we aim to study the latitudinal distribution of MS. To achieve this goal, we investigate four measurable properties of each jet, as proxies, as a function of their latitudinal position. Characteristic values of these parameters are found to be slightly greater for QS-MS than that of for CH-MS all around the solar disk. Contrary to the typical locii of QS-MS, which do not show a strong temporal variation, the birthplaces of CH-MS migrated further away from the poles between 2011 and 2014. After identifying four clusters in their spatial distribution, MS tend to follow the following nature: at around the date of beginning of each cluster, MS are seemed to be formed more likely around the solar poles. The formation locii of MS migrate away from the poles with a maximum longitudinal angular separation of $30°$ - $40°$ as time progresses. We have also found evidence towards supporting the hypothesis that there is a connection between the migration pattern of the formation cradle of MS and the nearly two-year-long oscillations present in a number of physical properties of MS.

4.1 Macrospicules Around the Solar Disc

The position of every jet is projected into a polar coordinate system. The radial coordinate is the angular distance between the disc center and the bottom point of each MS. The angular coordinate is derived as a right-angle difference between the position of the bottom point of each MS and the western equatorial limb. These polar coordinates are then converted into latitudinal and longitudinal positions.

CH-MS tend to appear around the northern and southern poles. QS-MS form a "ring" around CH-MS at lower latitudes as displayed in Figure 4.1. The main difference between the two MS classes is the ratio of the number of MS in the two hemispheres: QS-MS are formed nearly equally in terms of numbers on both hemispheres ($n_{\text{North\_QS}} = 69, n_{\text{South\_QS}} = 65$), respectively, while CH-MS prefer to appear more abundant on the southern hemisphere ($n_{\text{North\_CH}} = 39, n_{\text{South\_CH}} = 119$) during the interval of time investigated. Currently, these differences seem to be persistent after several extensions of the dataset: $n_{\text{North\_QS}} = 91, n_{\text{South\_QS}} = 76$, $n_{\text{North\_CH}} = 50, n_{\text{South\_CH}} = 130$. Our aim here is to connect the spatial distribution of MS to the distribution of their investigated physical properties (maximum length, maximum width, average velocity, maximum area).

In Figure 4.2 and Figure 4.3, an average value of all the MS properties are shown detected in bands of 30° around the solar disc. On the top-left panel of Figure 4.2 and Figure 4.3, QS-MS are wider in each segment of the solar disc. The widest QS-MS are formed around the solar equator (≈ 7.2 Mm), the narrowest ones are generated around the southern pole (≈ 6.3 Mm). The widest CH-MS appear around the southern pole and at lower latitudes on the northern hemisphere (≈ 6.5 Mm) with the average of ≈ 5.9 Mm.

The other three plots in Figure 4.2 and Figure 4.3 have one feature in common: each characteristic physical parameter of CH-MS is larger, than their counterparts of QS-MS. CH-MS jets grow higher in almost every direction at the solar limb (≈ 41–42 Mm), excluding the eastern equatorial territory, where QS-MS can match their size (≈ 40 Mm). In the remaining two cases, characteristic parameters of QS-MS are only greater at the eastern limb (≈ 70 km s^{-1} and 185 Mm^2 for average
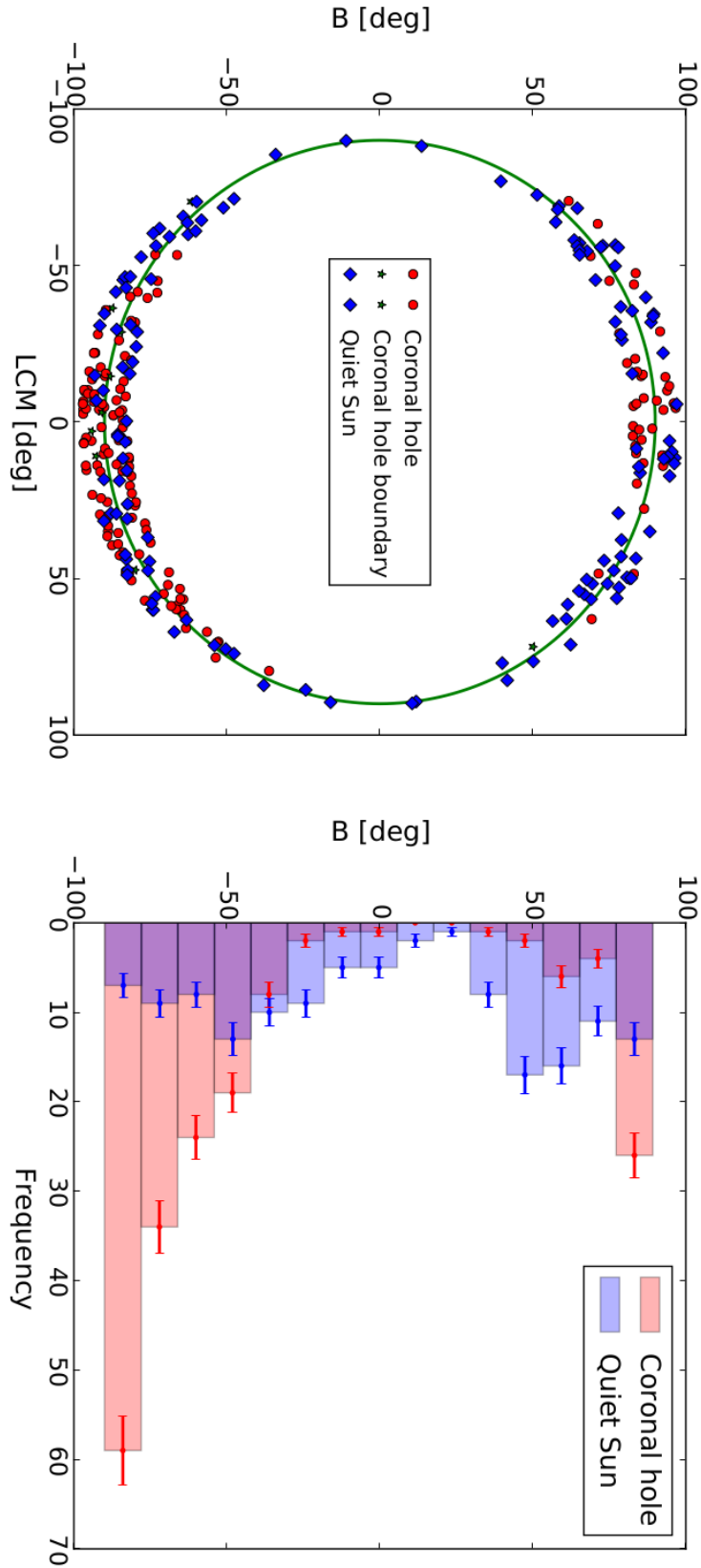
Figure 4.1: On the top, locations of all investigated MSs are plotted around the solar limb. Red, blue and green mark the coronal hole, Quiet Sun and coronal boundary MS, respectively. The vertical axis is the heliographic latitude (B). Longitude of central meridian (LCM) is along the horizontal axis. On the bottom, a histogram of CH-MS and QS-MS location is provided with red and blue strips, respectively.
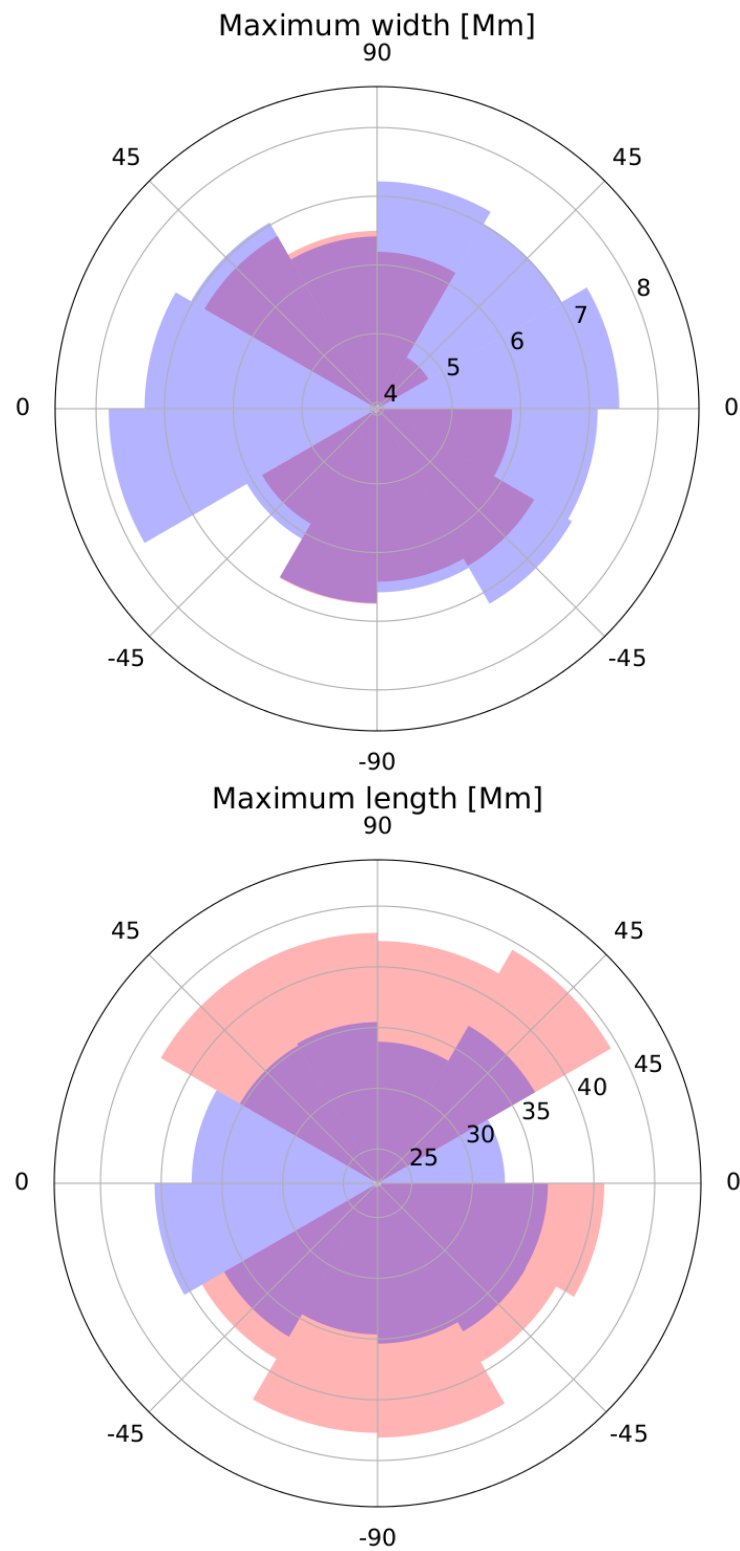
Figure 4.2: Latitudinal distributions of maximum width and maximum length of MS, observed around the solar limb. Red columns represent CH-MS, blue ones display QS-MS.
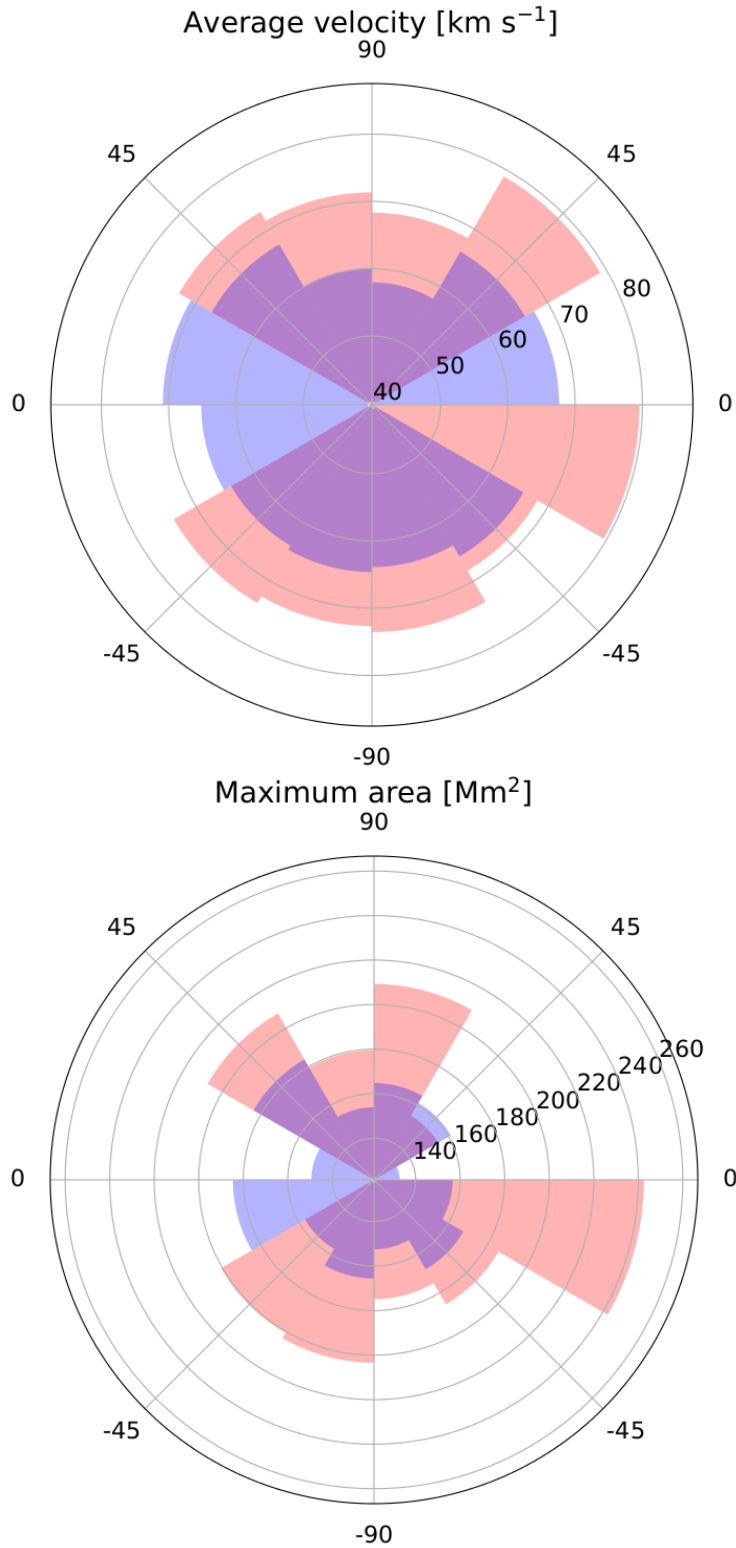
Figure 4.3: Latitudinal distributions of average velocity and maximum area of MS, observed around the solar limb. Red columns represent CH-MS, blue ones display QS-MS.
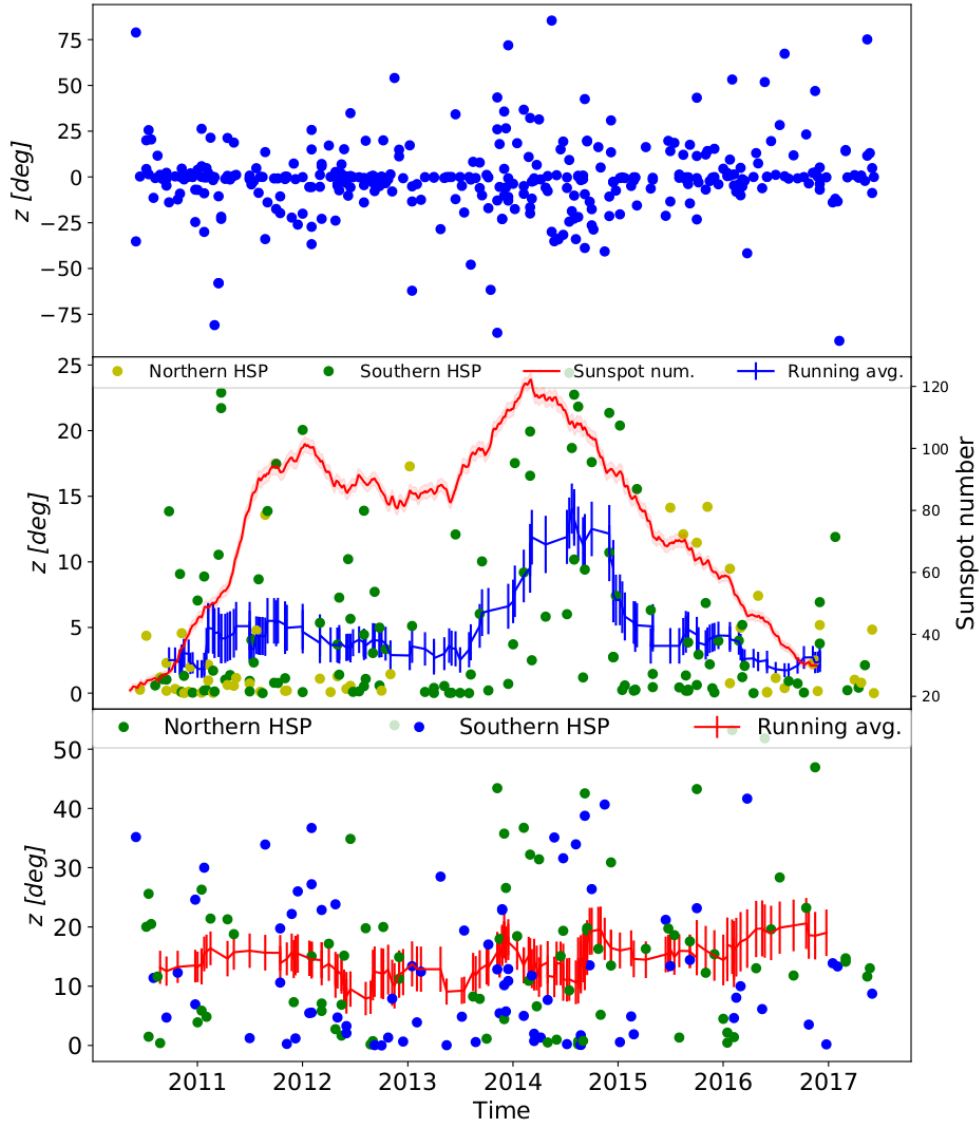
Figure 4.4: Top panel: latitudinal distance from the poles for MS. Middle panel: the distance from poles of CH-MS. Yellow/green points mark the MS on the northern/southern hemisphere. Blue error bars describe the running averages of these values. Bottom panel: the distance from poles of QS-MS. Green/blue markers refer to the northern/southern hemisphere. Red errorbars show their running average.

velocity and area, respectively). However, an outstanding peak can be seen in the distribution of the average valocity and the maximum area on the south-western limb for CH-MS (≈ 79 km s^{-1} and 240 Mm^2).
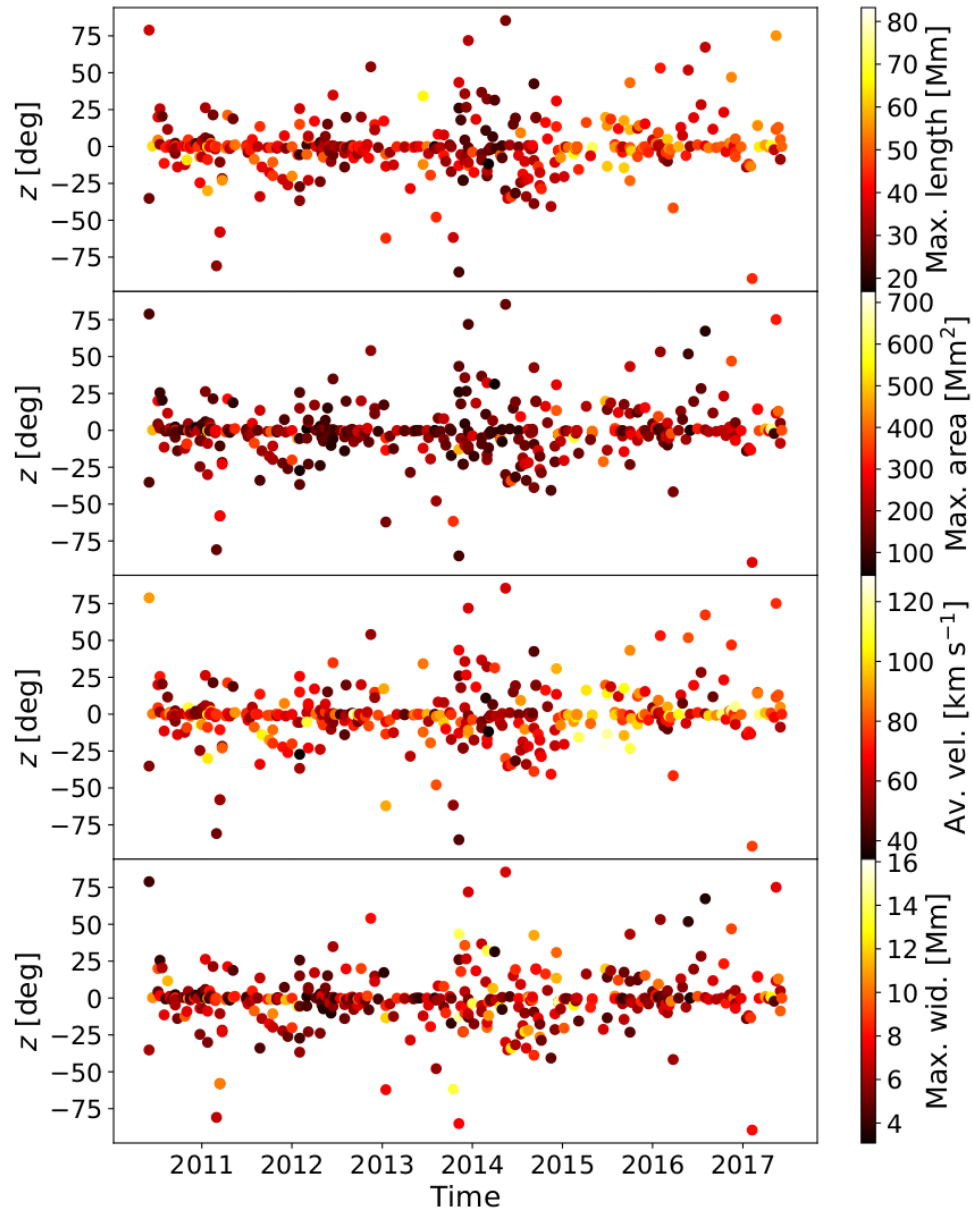
Figure 4.5: The *z*-distribution of MS scaled with the actual value of each MS parameters.

4.2 Distance from the Poles

In the following, we build on a major advantage of our dataset: its multiple-year-long length in time. To study the temporal variation of the spatial distribution of MS, we utilize the *distance from the poles* of each MS as follows:

$$z = \begin{cases} 90° - \theta_{\mathrm{MS}} & \text{if } \theta_{\mathrm{MS}} \geq 0 \\ -90° + \theta_{\mathrm{MS}} & \text{if } \theta_{\mathrm{MS}} < 0, \end{cases} \tag{4.1}$$

where θ_{MS} is the latitudinal position of a given MS. A similar geometric consideration was used previously by Gyenge et al. (2015). Due to the high-latitudinal appearance of these jets, the z parameter introduces an easier description of the spatial migration of MS.

z is visualized in the top panel of Figure 4.4 and all the panels in Figure 4.5. The locii of MS migrate from the poles with a maximal angular separation of $\approx 25°$. 40% of the sample (146 MS) are within $\pm 5°$ angular distance. Furthermore, it is clearly visible that MS tend to group together in this coordinate system. We investigate this latter behaviour in more detail further down.

In the lower two panels of Figure 4.4, we separate the CH-MS and QS-MS from each other. The samples of the two main MS classes are fundamentally different. The variation of the smoothed QS-MS data is rather limited, no clear feature can be seen. However, in the case of a smoothed z of CH-MS, a strong oscillation pattern is observable with two peaks: a smaller one around 2011 and a greater one between 2013 and 2015. By comparing this detected feature to the variation of the sunspot number during Solar Cycle 24, the similarities are obvious. Regardless of some outlier points around 2011, the highest values follow the trend of the sunspot number.

Another interesting aspect is the distribution of northern and southern macrospicules, visualised in the bottom and middle panels of Figure 4.4. QS-MS on both of the hemispheres and CH-MS on the southern hemisphere build up a quite homogeneous distribution, no obvious trends can be seen. However, northern CH-MS form two larger aggregations: one between June 2010 and January 2013 and another after June 2015. The average value of z is lower in the first group than in the second one.

According to this diagram, the coronal holes of the northern hemisphere seem to generate macrospicules during distinct time intervals.

4.3 Clusterization of the Spatial Distribution

In Figure 4.5, the distance from the poles of each MS is presented (similarly to Figure 4.4). Every point is scaled in colour according to the corresponding physical property (maximum length, maximum width, maximum area, average velocity) of each jet. The purpose of Figures 4.4–4.5 is to investigate the possible connection between the temporal variation of z of MS and their physical properties. MS tend to form groups in their z-distribution. These patterns would support two conjectures: i) the generation of MS is not homogeneous temporally, lower and higher MS activity sequences follow each other in time, and ii) the generation of MS is homogeneous temporally, then the formation locii of these jets are migrating and returning to the poles periodically.

To study the extent of validity of the first statement, more data is needed. The sampling rate which was used to construct our dataset does not provide a sufficiently large number of MS to prove fully this point. The frequency of detecting MS can reach even 4 MS per observing day with the average at around 1.07 per observing day.

However, we can run a more detailed investigation for supporting the second statement. First of all, groups of MS in the z-distribution have to be determined. For this analysis, we used the free and open-source *scikit-learn* package (Pedregosa et al., 2011) of Python. The utilized mean shift clustering is a centroid-based algorithm, which is aimed to discover "blobs" in a smooth density of samples. Four clusters have been identified this way. The time epoch of the boundaries for each cluster along with their central time, as given in brackets, are the following (nominated with upper case letters): A) 01.06.2010 – 24.08.2011 (24.01.2011), B) 01.09.2011 – 24.08.2013 (07.03.2012), C) 07.09.2013 – 01.07.2015 (07.07.2014), D) 24.06.2015 – 07.06.2017 (15.01.2016). These clusters are presented in the top panel of Figure 4.6 and visualised with four different colours to distinguish them.
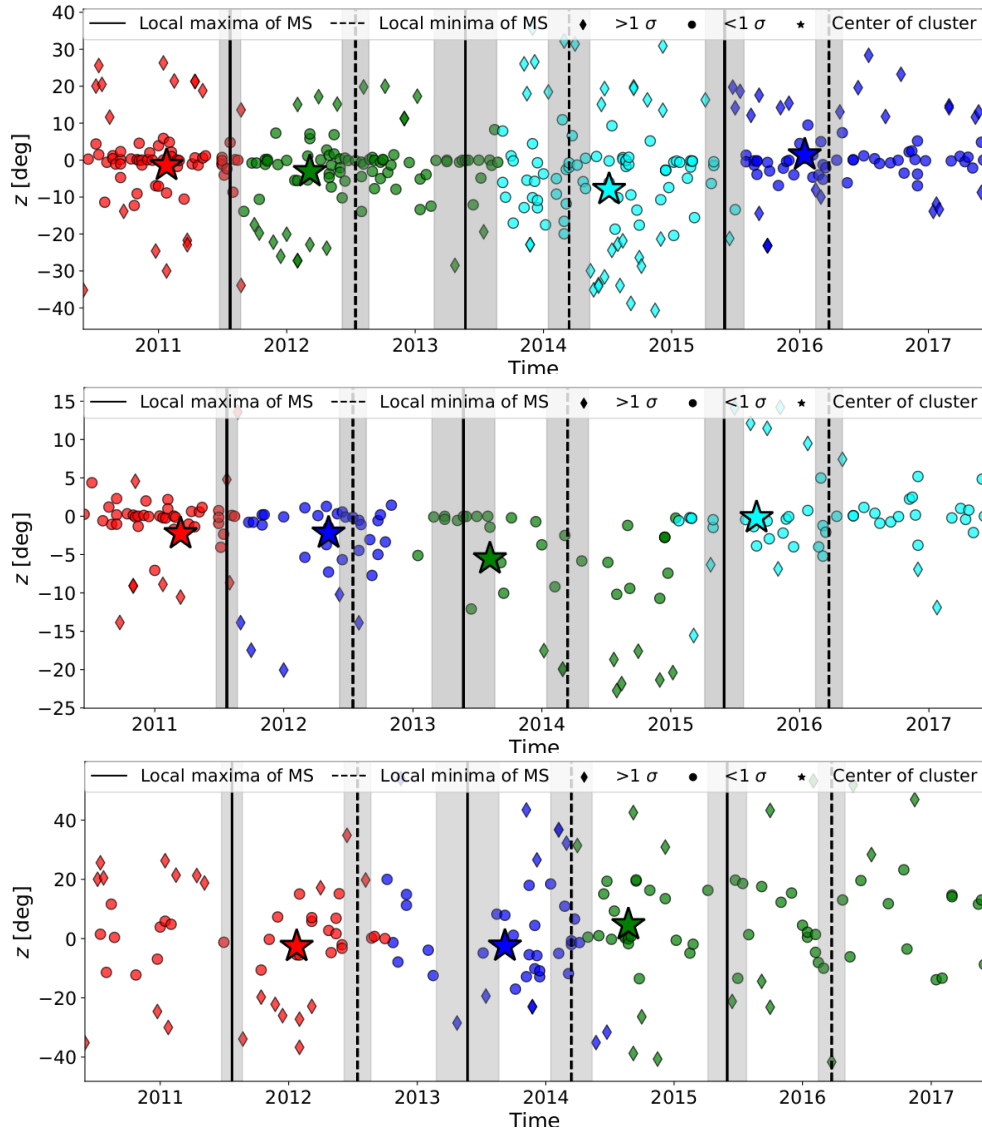
Figure 4.6: The z-distribution of three different datasets: top) all the MS, middle) only CH-MS, bottom) only QS-MS data are shown. The colors (red, green, cyan, blue) represent the identified clusters.

After we determine the values within (marked with circles in Figure 4.6) and outside (indicated by diamonds in Figure 4.6) of 1-σ distribution threshold for each cluster, the migration of locii of MS is strongly visible. In the beginning of every cluster, MS tend to be formed around the solar poles. Then, the jets begin to appear closer to the solar equator

on both hemispheres until their formation locii return to the solar poles and the next cluster starts to form. This trend is already visible for $< 1\sigma$ jets, but is even more clear for $> 1\sigma$ MS.

To gain more information about the plots in Figure 4.5, the average values for each physical property of MS in each cluster were determined. In each group, MS have been separated with respect to whenever they are inside or outside the 1σ threshold. Besides the averages, their standard deviations were also calculated. The results of this process are summarised in Table 4.1. By comparing the values around the poles to their counterpart ones further away, the average of MS with small z appear to be greater with a fraction of 13/16. The only greater values for further averages come up in the maximum length of B and the maximum width of C and D.

Nearly two-year-long periodicities were observed in three physical properties of MS. The epochs of the local maxima of these QBOs (solid vertical lines) overlap with the dates of the boundaries between clusters within 1σ error measurement. Therefore, when the formation locii of MS migrate back to the poles, their physical parameters reach the highest values. Conversely, then, the physical properties decrease to their minimum values when being spatially closer to the solar equator. However, the epochs of the minima do not overlap with the cluster centres within a 1σ error of measurement.

The same method was applied to the separated data of CH-MS and QS-MS, respectively. The middle panel of Figure 4.6 shows that four clusters were identified for CH-MS. To reflect on the similarities between clustering of all-MS and CH-MS, while also keeping them distinguished from each other, we used the notation of lower case letters for the CH-MS clusters. The time epoch of the boundaries for each cluster along with their central time, as given in brackets, are the following: a) 15.06.2010 – 24.08.2011 (15.03.2011), b) 01.09.2011 – 07.01.2013 (07.05.2012), c) 15.01.2013 – 01.15.2015 (07.08.2013), d) 24.01.2015 – 07.06.2017 (01.09.2015). As nomination for further comparison, we formed pairs of the clusters such as A–a, B–b, C–c, and D–d. The observed behaviour after clustering of CH-MS is similar to what we have found for all-MS: the epoch of the cluster boundaries are nearly identical for the A–a and D–d pairs. A difference arises at the epochs

Table 4.1: Averages and Standard Deviations of Each MS Physical Property for Every Cluster and the Difference Between the Averages Over and Under the 1σ Limit

Cluster	$< 1\sigma$ Maximum length [Mm] Average	Standard deviation	$> 1\sigma$ Maximum length [Mm] Average	Standard deviation	Diff.
A	42.1	10.03	37.49	10.04	4.61
B	36.56	8.71	37.01	8	-0.41
C	37.78	12.44	33.76	11.35	4.02
D	47.64	8.47	45.99	11	1.65

Cluster	$< 1\sigma$ Maximum area [Mm^2] Average	Standard deviation	$> 1\sigma$ Maximum area [Mm^2] Average	Standard deviation	Diff.
A	201.5	102.67	174.51	73.38	26.99
B	161.4	77.43	159.6	63.37	1.8
C	190.59	102.73	182.49	86.9	8.1
D	237.5	102.1	223.93	91.36	13.57

Cluster	$< 1\sigma$ Average velocity [km s^{-1}] Average	Standard deviation	$> 1\sigma$ Average velocity [km s^{-1}] Average	Standard deviation	Diff.
A	70.22	15.6	62.81	14.74	7.41
B	68.51	16.41	66.05	13.9	2.46
C	69.42	19.43	65.69	16.3	3.73
D	81.65	18.05	74.97	20.25	6.68

Cluster	$< 1\sigma$ Maximum width [Mm] Average	Standard deviation	$> 1\sigma$ Maximum width [Mm] Average	Standard deviation	Diff.
A	6.68	2.02	6.47	1.84	0.21
B	6.25	2.12	6.21	1.47	0.04
C	7.48	2.61	7.78	2.4	-0.3
D	6.85	1.95	6.99	1.92	-0.14

of the cluster boundaries between the second and the third clusters: the
duration of b is shorter, then B (or on the other way around, the length
of c is larger, then C). The differences between the central times of each
cluster are: A–a) -50 days, B–b) -61 days, C–c) 334 days, D–d) -136 days.
Furthermore, the migrating behaviour is strongly visible.

After the separation of QS-MS from CH-MS, as displayed in the bot-
tom panel of Figure 4.6, three clusters were found, therefore, their be-
haviour is significantly different, then the nature of CH-MS. The migra-
tion behaviour is not that obvious when compared to its counterpart in
the case of CH-MS.

All these results indicate a yet to be understood connection between
the physical properties of MS and their spatial distribution that requires
modelling efforts, beyond the scope of our current study. The related
fundamental questions to be answered are: What physical process(es)
would generate the spatio-temporally oscillatory properties of MS. How
are these processes linked to global solar oscillations? Are they even
global, as a result of the global solar dynamo, or local, as a result perhaps
of local dynamo?

4.4 Conclusions

In this chapter, we studied the spatial distribution of MS in more detail. The polar coordinates of each MS on the solar disc have been converted into a heliographic coordinate system for analysis. Because Active Regions were excluded from the solar area of investigation by definition, where MS also could be identified, the observed jets are found to be at high(er) solar latitudes. CH jets accumulate around the solar poles due to the large-scale open magnetic field of polar Coronal Holes. Quiet Sun MS form a "ring" around them. Further, a strong asymmetry is visible in the number of CH-MS between the hemispheres. The number of CH-MS on the southern hemisphere is almost three times larger, than that of the northern hemisphere. The sources of this difference may be the solar dynamo as that was shown for e.g. sunspot area (Chowdhury et al., 2013; Kitchatinov & Khlystova, 2014).

First, it was found that the southern hemisphere dominates the northern hemisphere in the terms of CH-MS production rate ($n_{\mathrm{North\_CH}} = 43, n_{\mathrm{South\_CH}} = 162$). However, the numbers of QS-MS are nearly the same on both hemispheres ($n_{\mathrm{North\_QS}} = 75, n_{\mathrm{South\_QS}} = 87$).

Then, the distribution of four physical properties of MS (i.e. maximum length, maximum width, maximum area and average velocity) were shown to be coupled to the latitudinal position of each MS. QS-MS are found to be wider and nearly all around the solar disc (≈ 7.1 Mm for QS-MS and ≈ 5.9 Mm for CH-MS). However, CH-MS appear to be longer, faster and larger in area all over the disc: e.g., maximum length – CH-MS ≈ 42 Mm, QS-MS ≈ 35 Mm average velocity – CH-MS: ≈ 70 km s^{-1}, QS-MS ≈ 63 km s^{-1}.

To study the migration properties of the locii of MS, the following reference system was used: the angular distance from the solar poles (z) was introduced instead of the latitudinal position. Due to their high latitudinal position, the z-distribution of MS aggregate around $0°$ with a maximum separation of $\approx 25°$. However, 146 jets out of 361 stay within $\pm 5°$ from the poles. A strong temporal variation can also be seen here: MS tend to form clusters in their z parameter.

After the separation of CH-MS from QS-MS, the two classes seem to behave in rather different ways. The distance of QS-MS from the poles

seems to be overall constant, while CH-MS present a strong oscillation pattern. Two peaks are visible: a weaker one between June 2010 and January 2013 and a greater one between August 2013 and June 2015. This oscillatory behaviour shows similarities to the temporal variation of the sunspot number in Solar Cycle 24.

In order to gain more information about the z-distribution of the MS groups, we utilized the mean-shift clustering of the *scikit-learn* package for Python. The result of the analysis is the detection of four clusters: A) 01.06.2010 – 24.08.2011, B) 01.09.2011 – 24.08.2013, C) 07.09.2013 – 01.07.2015, D) 24.06.2015 – 07.06.2017. Each cluster is divided into two subgroups with respect to whenever they are inside or outside of the 1σ standard deviation threshold from the poles. The average of each physical property of MS in each subgroup was determined. In 13 out of 16 cases, MS close to the poles are larger, wider and their upward speed is larger. A similar analysis is applied separately to both CH-MS and QS-MS data. Four clusters have been identified for CH-MS: a) 15.06.2010 – 24.08.2011, b) 01.09.2011 – 07.01.2013, c) 15.01.2013 – 01.15.2015, d) 24.01.2015 – 07.06.2017.

Furthermore, the formation locii of MS display a strong migration behaviour. At the beginning of each cluster, MS appear close to the poles with small z. Progressing in time, the locii of MS tend to migrate away from the poles and return at the end of the cycle. The magnitude of separation varies between 20° and 40°. The epoch of all the local minima and maxima of the QBO signatures of MS cover the boundary between clusters. After the separation, CH-MS seem to feature this migration pattern, while QS-MS are more scattered. Therefore, as a final conclusion, we report the finding that CH-MS may play the dominant role in the periodic migration trend of the investigated MS.

Chapter 5

The Motion of Macrospicules

Abstract

In this chapter, the trajectories of MS are studied in order to analyse the interaction between the plasma of the jets and the surrounding plasma environment. During the entire lifetime of each MS, their height data are collected. This dataset shows a strong parabola-like feature of their trajectory, which indicates the powerful influence of gravity on the motion of the jets. In order to gain more information about other prominent forces (e.g. drag force), we seek asymmetries in the data of these parabola-like trajectories in order to e.g. account these deviation to the non-ideal (e.g. viscous) nature of the solar atmosphere. After excluding the phase of MS during their rising time, when they are not visible over the solar limb, strong asymmetries have been found both in their parabolic path and the time-spans between the rising and decaying phases of MS. Kinematic and dynamic models are also constructed in order to simulate the motion of the jets.

5.1 Trajectories in the Solar Atmosphere

Several earlier studies have already investigated the motion of MS in the solar atmosphere. Withbroe et al. (1976) and Karovska et al. (1994) found that the orbit of MS is nearly parabolic, which indicates the dominant impact of gravity on the motion of these ejecta. However, the measured deceleration of jets was found to be much lower than acceleration due to gravity. Recently, Loboda & Bogachev (2019) carried out a detailed analysis concerning the observed orbit of chromospheric MS based using the intensity maps of the *SDO/AIA*. The authors investigated a subset of MS, whose trajectories are close to parabolic. According to their findings, MS may be driven by magnetoacoustic shocks with a period of 10 ± 2 minutes. This generation process may be similar to the one of type-I spicules (De Pontieu et al., 2004). Furthermore, $10\% - 30\%$ of the plasma material reach the temperature of the corona.

Our orbit measurement is based on the data gathered with the tetragon approximation. The first indication of the appearance of a jet is a brightening under the solar limb, as described in Section 2.2. The lifetime of a macrospicule is counted from the moment of appearance of the brightening until the top point falls back under the limb. In order to map their trajectories, the actual height is estimated based on observation during the lifetime of each MS. Since the temporal resolution of the 30.4 cm channel of *SDO/AIA* is 12 s, 31032 data points were collected about the continuously changing heights of 356 detected jets. These data are, then, visualised along with the elapsed time since the epoch of the kick-off of each MS in Figure 5.1. In these figures, each point is coloured with respect to the density of the surrounding points: dark-blue represents low density of points, yellow indicates a high density. The density profile reveals a parabola-like trajectory for the path. Such behaviour also remained after the separation of MS into subclasses: 15490 and 1420 data points for CH-MS and QS-MS, respectively.

Firstly, we investigate whether short-lived MS behave similarly to ones with longer lifetimes. For this reason, MS have been divided into four classes according to their lifetime. The reason for splitting MS into four groups is twofold: i) we wish to generate an adequate number of groups to make any variation statistically clearly relevant (and visual)

Table 5.1: Comparison of the Trajectory of Different Lifetime Macrospicules

Duration	NP[1]	1	2	3	4	5	6	7	8	9
All MS										
0 – 534 s	159	6.53	14.46	21.97	24.60	24.80	25.63	25.27	25.06	11.58
535 – 1068 s	14854	7.99	20.22	29.27	31.89	30.78	27.29	23.43	19.56	13.50
1069 – 1602 s	14701	10.20	25.87	36.14	39.37	37.10	29.85	22.59	19.82	16.39
1602 – 2136 s	1318	13.45	29.47	39.49	43.74	47.33	39.00	28.05	22.30	14.37
CH-MS										
0 – 531 s	35	4.65	8.69	13.30	19.86	24.70	24.14	21.55	20.06	17.13
532 – 1062 s	7713	8.42	21.43	32.39	34.26	33.44	30.06	26.56	22.90	15.19
1063 – 1593 s	7359	10.17	26.92	38.40	42.26	40.15	32.53	25.42	21.00	20.85
1594 – 2124 s	383	10.39	37.45	49.44	60.37	55.17	43.13	42.60	33.49	23.45
QS-MS										
0 – 534 s	124	7.11	20.38	23.98	24.52	27.74	31.20	29.85	25.06	11.58
535 – 1068 s	6291	7.33	18.34	25.57	28.39	27.90	24.94	20.69	16.51	12.16
1069 – 1602 s	7076	10.24	25.32	34.46	36.63	34.02	27.99	20.49	18.96	12.86
1603 – 2136 s	712	14.38	29.54	41.29	51.34	49.24	38.60	26.82	26.93	26.90
Difference between CH-MS and QS-MS										
0 – 534 s	-	-2.46	-11.69	-10.67	-4.65	-3.03	-7.05	-8.30	-4.99	5.54
535 – 1068 s	-	1.09	3.08	6.81	5.86	5.54	5.11	5.86	6.39	3.03
1069 – 1602 s	-	-0.05	1.60	3.94	5.63	6.12	4.53	4.93	2.03	7.98
1603 – 2136 s	-	-3.98	7.91	8.14	9.02	5.92	4.53	15.77	6.56	-3.44

This table summarizes the medians of boxplots of MS heights in each duration group for four different data collections: i) all the MS; ii) only CH-MS; iii) only QS-MS; and iv) differences between the values of only CH-MS and only QS-MS measurements. Under the numbers 1–9, the height values are provided in Mm unit. Column NP shows the number of points in the given duration group.

in the orbit of MS with different lifetimes; and ii) construct sub-datasets
with sufficient amount of data for further analysis. Consequently, four
groups are constructed with the following time durations: 1) 0 – 534 s;
2) 535 – 1068 s; 3) 1069 – 1602; 4) 1602 – 2136. The volume of data in
groups 2 and 3 is sufficiently large. The size of groups with longer and
shorter lifetimes is one and two magnitudes smaller, respectively. These
groups are visualised in Figure 5.2. The density estimation of points is
also applied in each groups. The high-density area in each groups show
a parabola-like trend.

Information about the trends in each group has been analysed by us-
ing boxplots (McGill et al., 1978), as shown in Figure 5.3 and Figure 5.4.
The box extends from the lower to the upper quartile values of the data,
with a line at the median. The whiskers extend from the box to show
the range of the data. Flier points are those past the end of the whiskers.
Each box represents 50% of the data, while the whiskers cover 95%. The
medians of each sets are collected into Table 5.1. In each group, MS
reached their maximal height in the fourth or fifth box. The groups
show a growing trend when compared to each other: the longer-lived MS
seem to reach higher altitudes in the same phase of existence.

By comparing the two subclasses to each other, as seen in Figure 5.5,
it is clear that their orbits are significantly different. Among the shortest
MS, QS-MS seem to reach higher during their entire lifetime. However,
there is only one CH-MS in this time domain (while the population of QS-
MS is three). For this reason, this time domain should not be considered.
In all the other groups, CH-MS are significantly longer during their entire
lifetime. The possible explanation for this nature could be rooted in the
difference between the magnetic field topology of the CH and QS areas.

The trajectory of each MS in the current state is definitely asymmet-
ric. The reason of this effect is simple: the data collection of each jet
began before the ejecta appeared over the limb, however, it ended when
the top point of the jet fell under the solar limb. After this epoch, there
is no visible information about the position of the jet any more. In order
to investigate the behaviour of the jets over the surface, the first part of
their rising has been removed from each time series. Therefore, both the
beginning and the ending of an MS lifetime is the epoch of the crossing
of its top point and the solar limb. Similarly to Figure 5.2, the boxplots
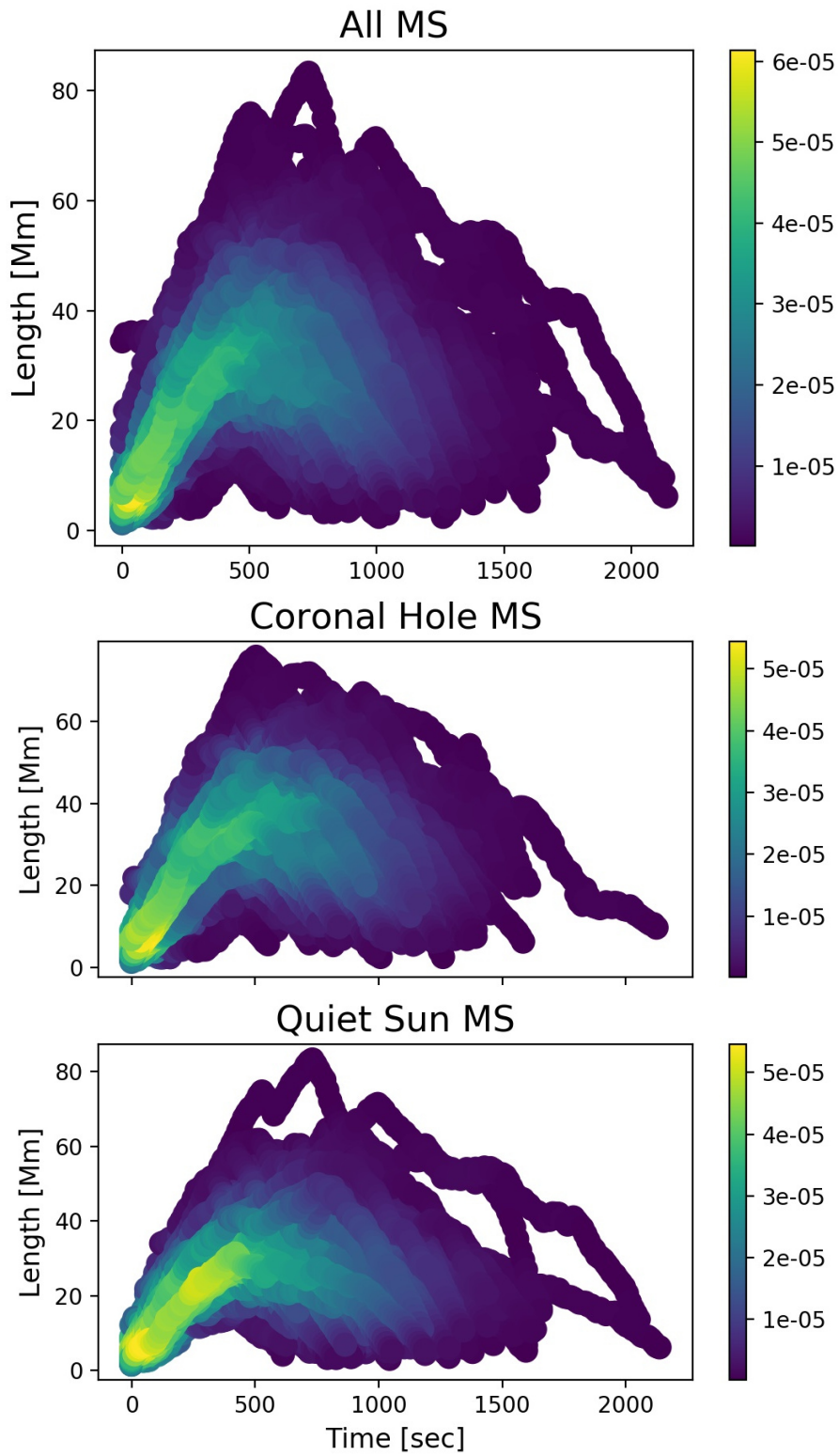
Figure 5.1: Orbits of MS from original data.

Figure 5.2: Boxplot of duration-separated MS orbits.
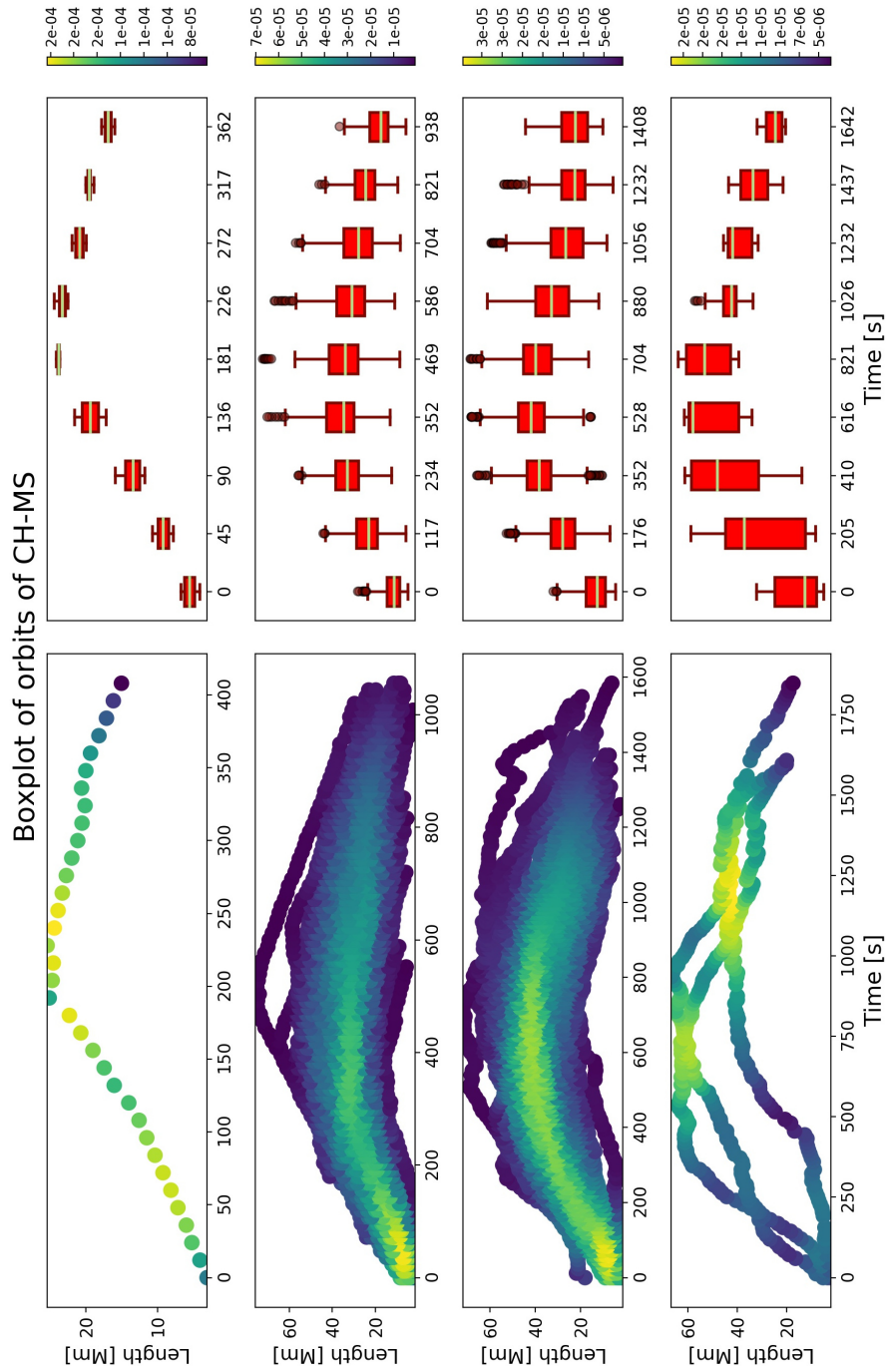
Figure 5.3: Boxplot of duration-separated CH-MS orbits.
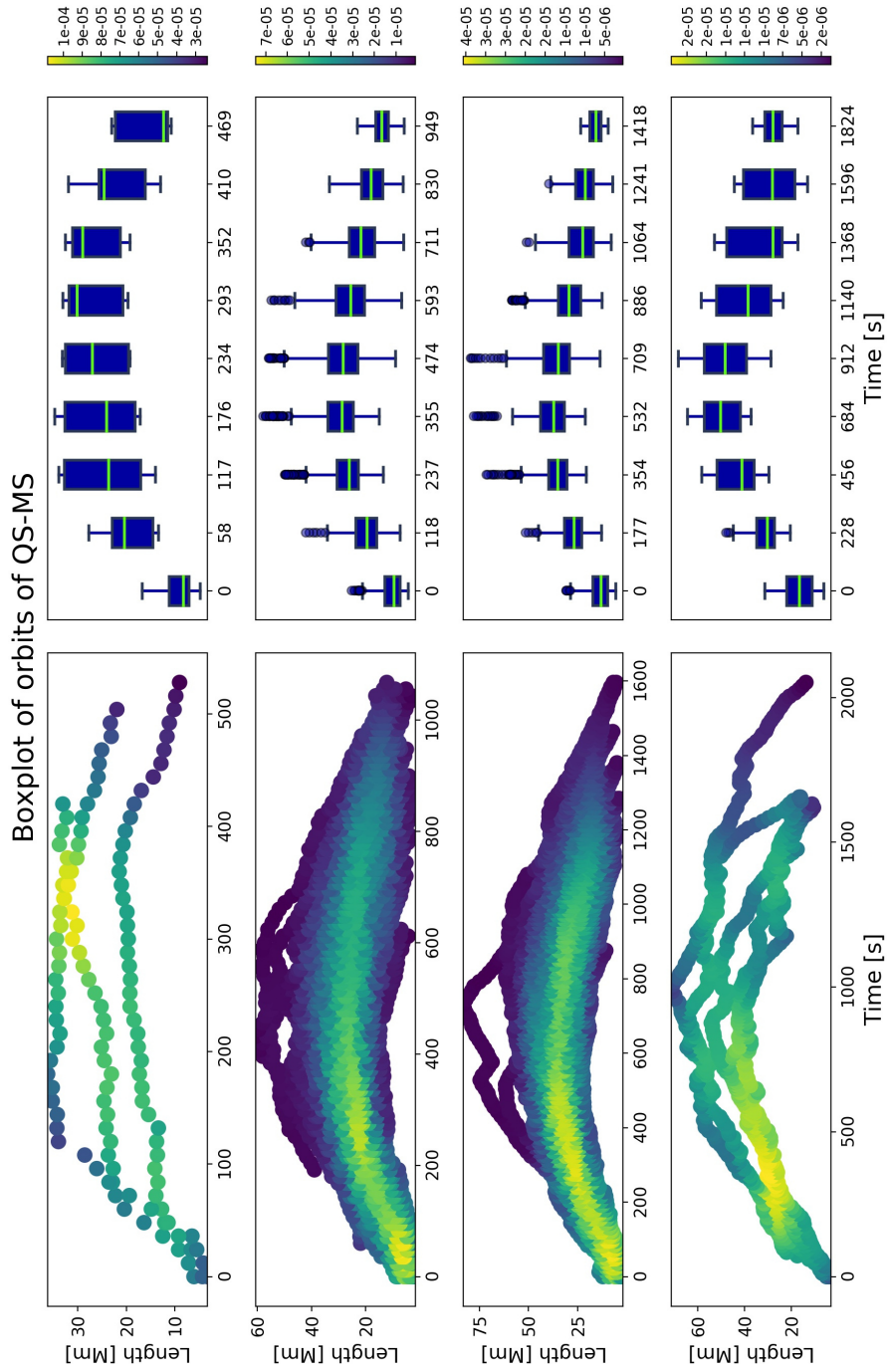
Figure 5.4: Boxplot of duration-separated QS-MS orbits.
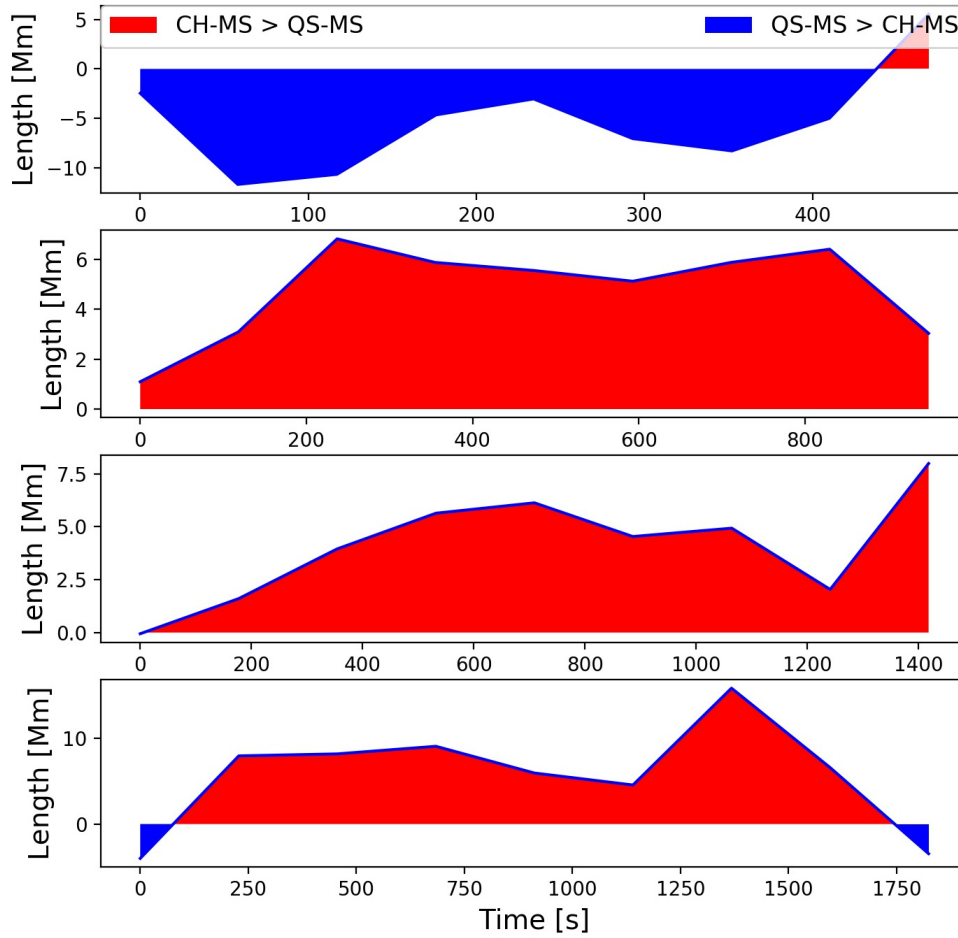
Figure 5.5: Difference between medians of boxplots in each panel from Figure 5.3 and Figure 5.4. If the colouring is red, CH-MS reach a higher length. If QS-MS are longer, the shading is blue.

of each group of this over-the-limb data are shown in Figure 5.7 and Figure 5.8. The population of each lifetime duration group is changed slightly: the first group becomes more populous and the last one turned up to be less dense. However, the trends between them remained the same in Figure 5.11: CH-MS seem to be larger in their entire lifetime than QS-MS.

The removal of the under-the-limb phase of each MS lifetime was necessary to study asymmetries in the dataset. The time ratio between the duration of the rising phase and the decaying phase must be calculated.

We defined the rising phase as the time-span between the first observation of the MS over the limb and the epoch of the maximum length. Similarly, the decaying phase stretches between the epoch of the maximum length and the last observation. These time-spans are estimated for all the MS. The results are presented in Figure 5.10. In a purely symmetric case, all the points must be organised along the identity function. However, the points are scattered and the linear correlation between them is weak in both MS classes ($k_{CH} = 0.1689, k_{QS} = 0.2583$). Furthermore, the slopes of the lines are much lower ($s_{CH} = 0.1575, s_{QS} = 0.2721$) than that of the identity function. The populations of points under and over the identity function is not equal: for QS-MS, 101 jets have longer decaying phase than rising phase out of 172 cases ($\approx 62\%$). In the case of CH-MS, the trend is the opposite: out of 183 CH-MS 136 have a longer rising phase than decaying ($\approx 74\%$). This ratio would also support that the evolution of the two MS classes are different during their lifetime. Moreover,

Similarly to their temporal study, the asymmetry in the length distributions should also be investigated. For this analysis, we take the medians of boxes in Figure 5.7 and Figure 5.8. Each median in the rising phase has been correlated to its counterpart in the decaying phase: e.g. the median of the first box in the rising phase is compared to the median of the last box in the decaying phase, the second box of rising phase to the penultimate one of the decaying phase and so on. This procedure is then carried out for all four lifetime duration groups and displayed in Figure 5.11. These points are much closer to a linear distribution, but are still rather scattered.

Next, let us normalise all the MS length and lifetime data with respect to their maximum length and lifetime. With this step, we assume that all the MS are generated in the same way, and physically, there is no difference between their evolution. The differences between the trajectories of the jets we identified are in the maximum lengths and lifetimes they reach. The normalised distribution shows a strong parabolic trend after excluding the outlying values (over 3σ distribution), as demonstrated in Figure 5.12. However, the trend is not entirely symmetric, which shows up in the differences between the lengths of the rising and the decaying phases as visualised in Figure 5.12. The boxplot of the normalised dataset is also provided in Figure 5.12. Similarly to the non-normalised

Table 5.2: Comparison of the Trajectory of Different Lifetime Macrospicules (Over-the-limb data)

Duration	NP[1]	1	2	3	4	5	6	7	8	9
					CH-MS					
0 – 534 s	159	20.83	26.90	27.61	28.81	28.61	27.30	24.50	22.85	19.07
535 – 1068 s	14854	14.72	27.50	34.20	35.45	33.55	30.06	26.61	22.29	15.48
1069 – 1602 s	14701	13.96	30.46	40.91	42.85	40.06	31.69	24.20	21.07	19.70
1602 – 2136 s	1318	16.46	37.46	46.53	56.75	48.56	39.83	37.74	23.73	14.73
					QS-MS					
0 – 534 s	124	15.13	22.61	23.93	25.12	27.29	24.59	21.43	17.23	15.42
535 – 1068 s	6291	12.14	22.02	27.72	29.09	27.66	24.40	20.33	16.93	12.12
1069 – 1602 s	7076	13.69	27.45	35.10	36.79	34.31	27.36	20.06	18.78	13.87
1603 – 2136 s	712	16.90	29.89	41.40	51.34	49.14	37.78	26.94	30.53	16.55
				Difference between CH-MS and QS-MS						
0 – 534 s	-	5.70	4.30	3.68	3.68	1.32	2.71	3.07	5.62	3.65
535 – 1068 s	-	2.58	5.48	6.48	6.36	5.89	5.66	6.28	5.37	3.36
1069 – 1602 s	-	0.27	3.01	5.81	6.06	5.76	4.33	4.14	2.29	5.83
1603 – 2136 s	-	-0.44	7.56	5.13	5.41	-0.58	2.06	10.80	-6.80	-1.82

This table summarizes the medians of boxplots of over-the-limb MS heights in each duration group for four different data collections: i) all the MS; ii) only CH-MS; iii) only QS-MS; and iv) differences between the values of only CH-MS and only QS-MS measurements. Under the numbers 1–9, the height values are provided in Mm unit. Column NP shows the number of points in the given duration group.
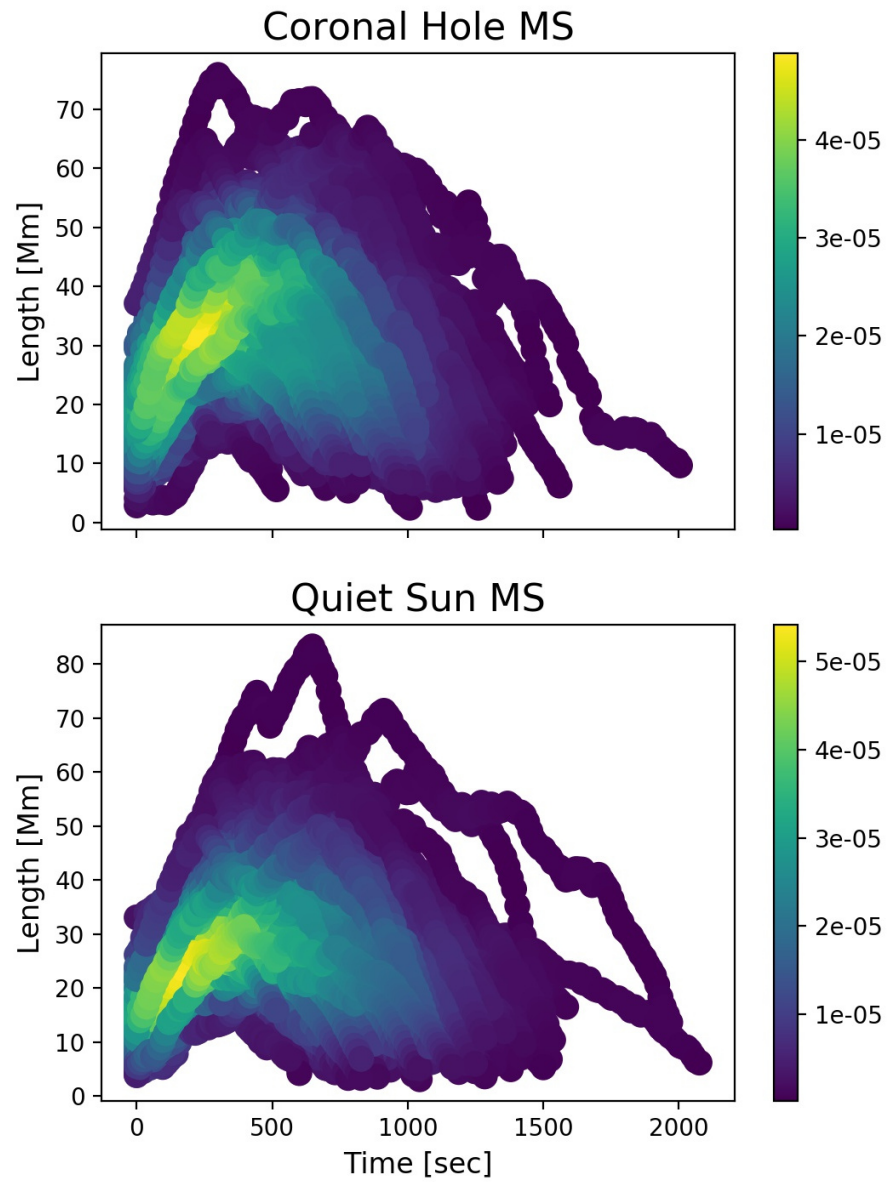
Figure 5.6: Orbits of CH-MS and QS-MS from the over-the-limb data.
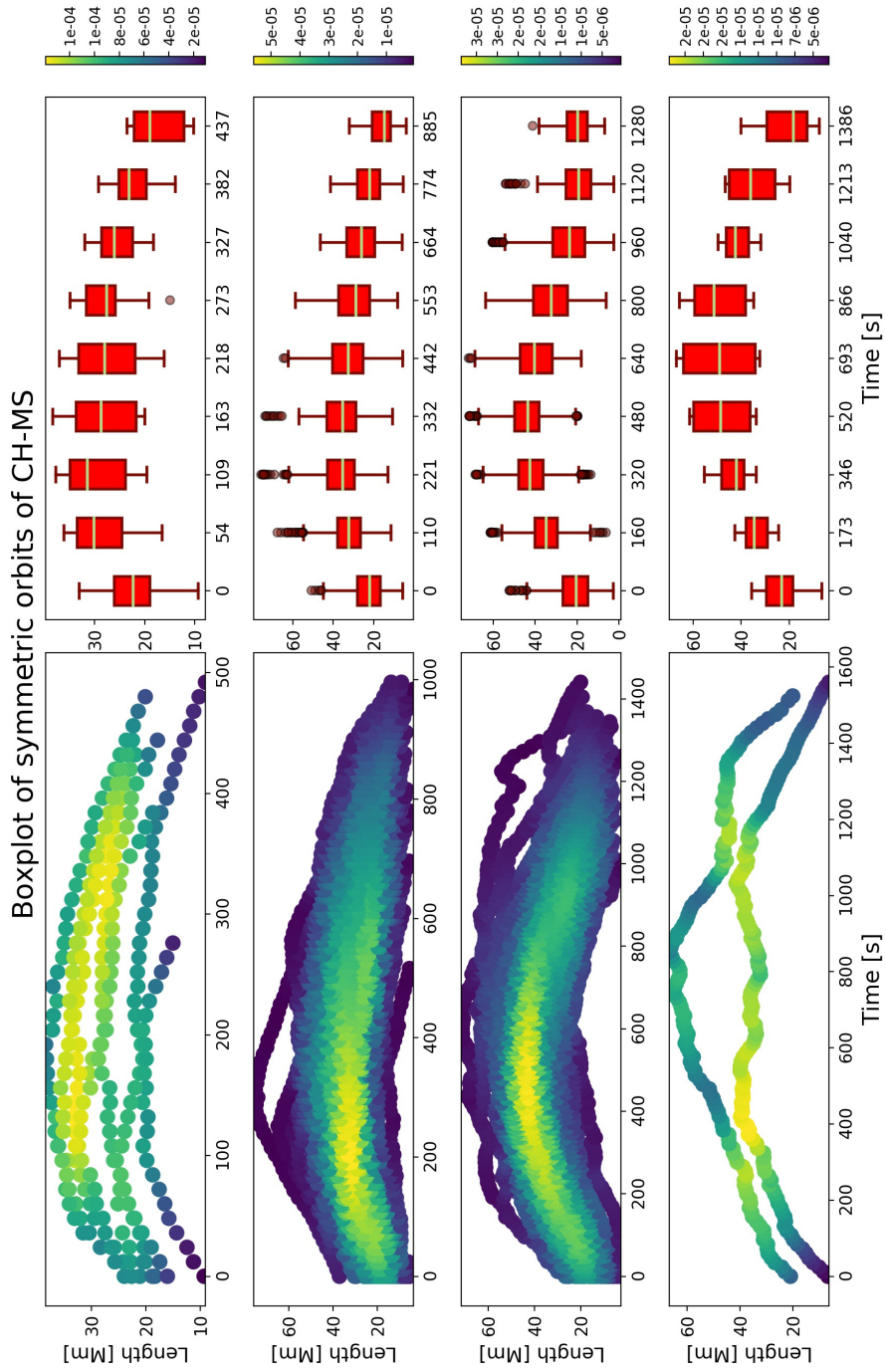
Figure 5.7: Similar methods utilized as in Figure 5.3, but applied on over-the-limb CH-MS data.
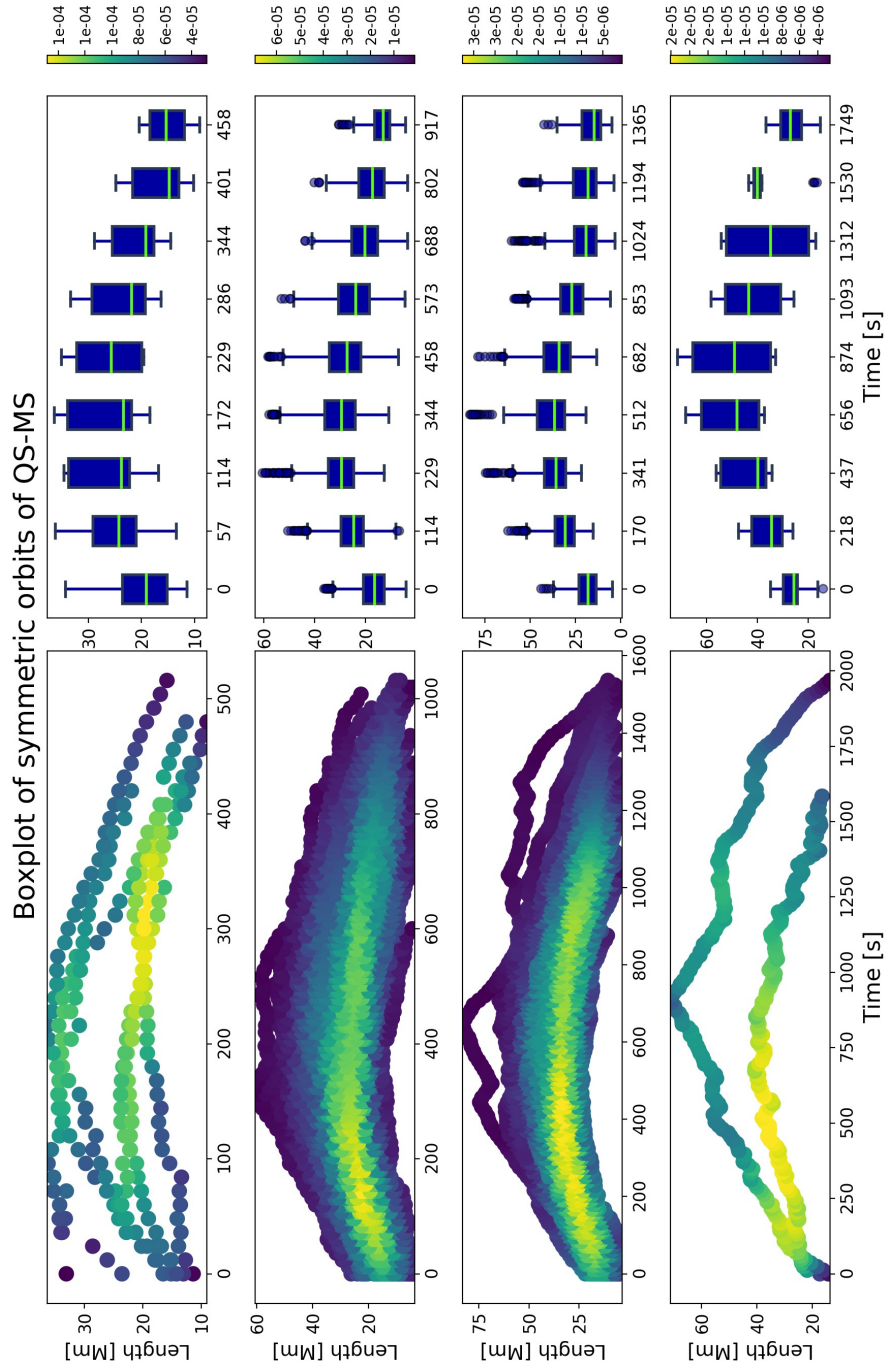
Figure 5.8: Same as Figure 5.4, but the data is the over-the-limb QS-MS orbits.
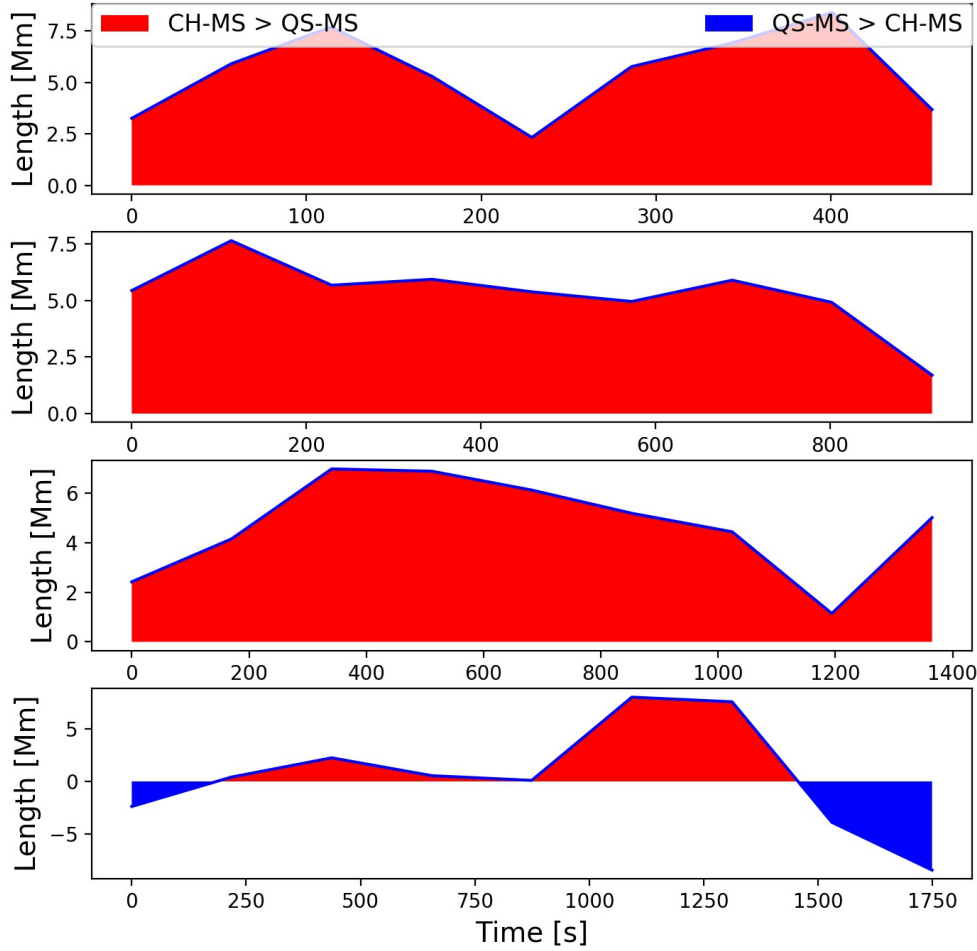
Figure 5.9: Difference between medians of duration-separated over-the-limb box-plots in each panel from Figure 5.7 and Figure 5.8. If the colouring is red, CH-MS reach a higher length. If QS-MS are longer, the shading is blue.

dataset, we have carried out a correlation analysis between the medians of corresponding boxes in the rising and the decaying phases of MS evolution. These correlations are also displayed in Figure 5.13. The linear correlation in this plot is really strong ($k = 0.9913$), with having a nearly identical slope. Significant divergence from the fitted line occurs close to maximum of the dataset. The source of this fluctuation is possibly due to the asymmetric nature of propagation of the individual MS: they reach their maxima with some deviation (temporally, in both directions) from the half of the their lifetime.
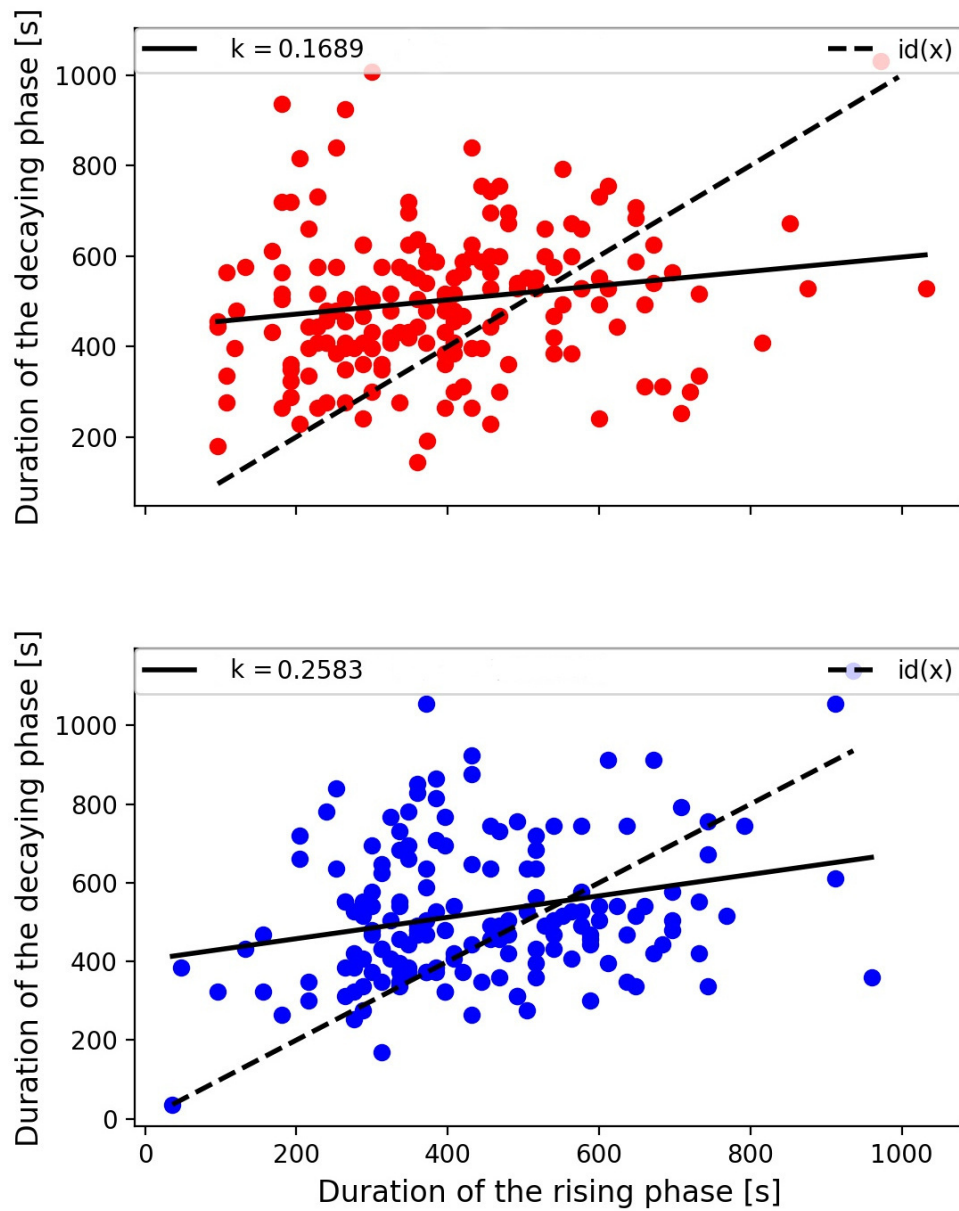
Figure 5.10: Ratio between the durations of the rising and decaying phase of MS. The top panel contains the over-the limb data of CH-MS, the bottom panel represents the data of QS-MS.
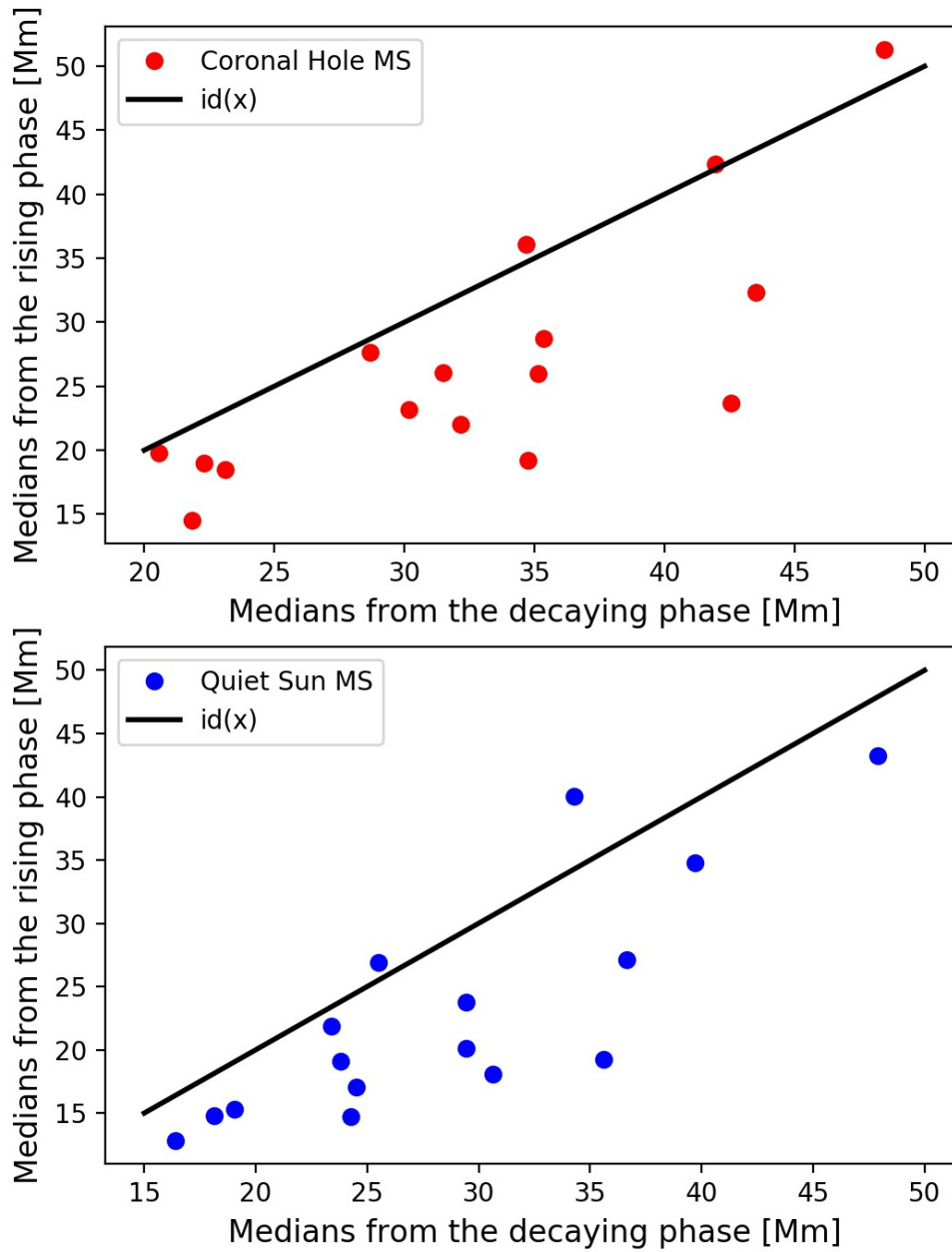
Figure 5.11: Ratio between the medians of the rising and decaying phase of MS. The top panel contains the data for CH-MS, the bottom panel represents the data of QS-MS.
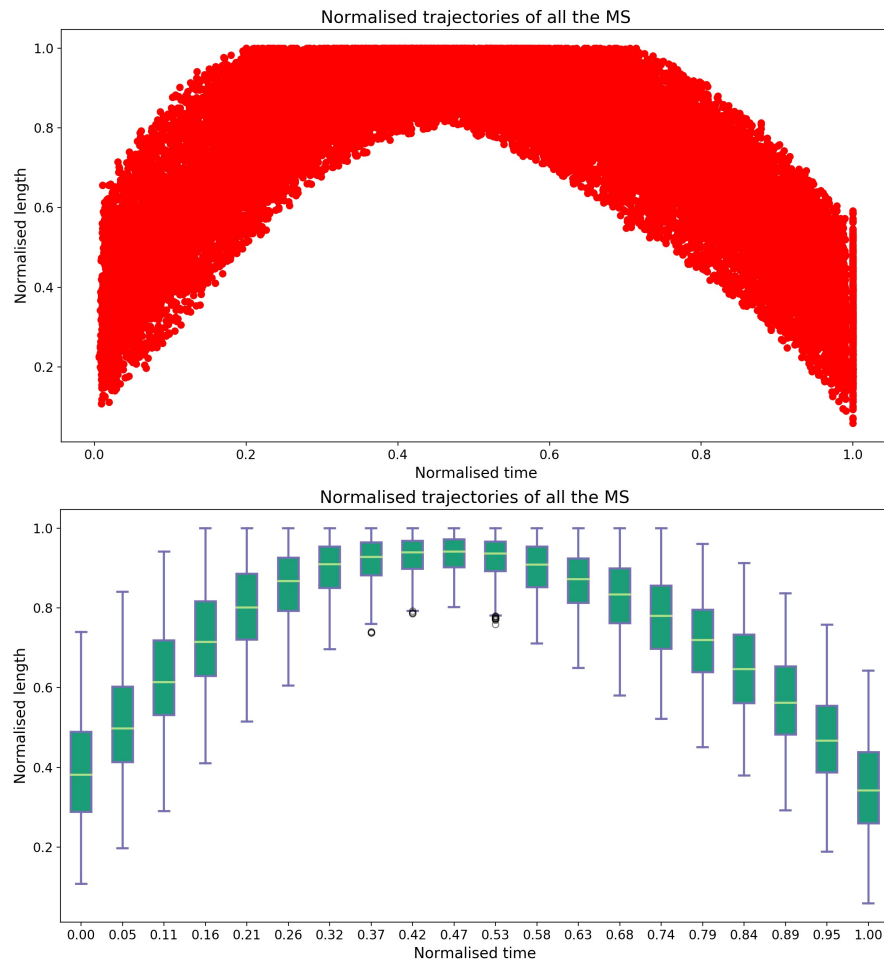
Figure 5.12: Top panel: collection of normalised trajectories. Bottom panel: box-plot of the normalised trajectories.

5.2 Modelling of the Trajectories

5.2.1 Kinematic Approach

After collecting data about the movement of MS in the solar atmosphere, we would like to provide a simple modelling interpretation of the observed features. It has been already discussed in the literature and also seen during the data collection campaign of the Thesis that MS extend along a given direction. This direction of rise and receding could be possibly the direction of the orientation of a magnetic flux tube, which the MS
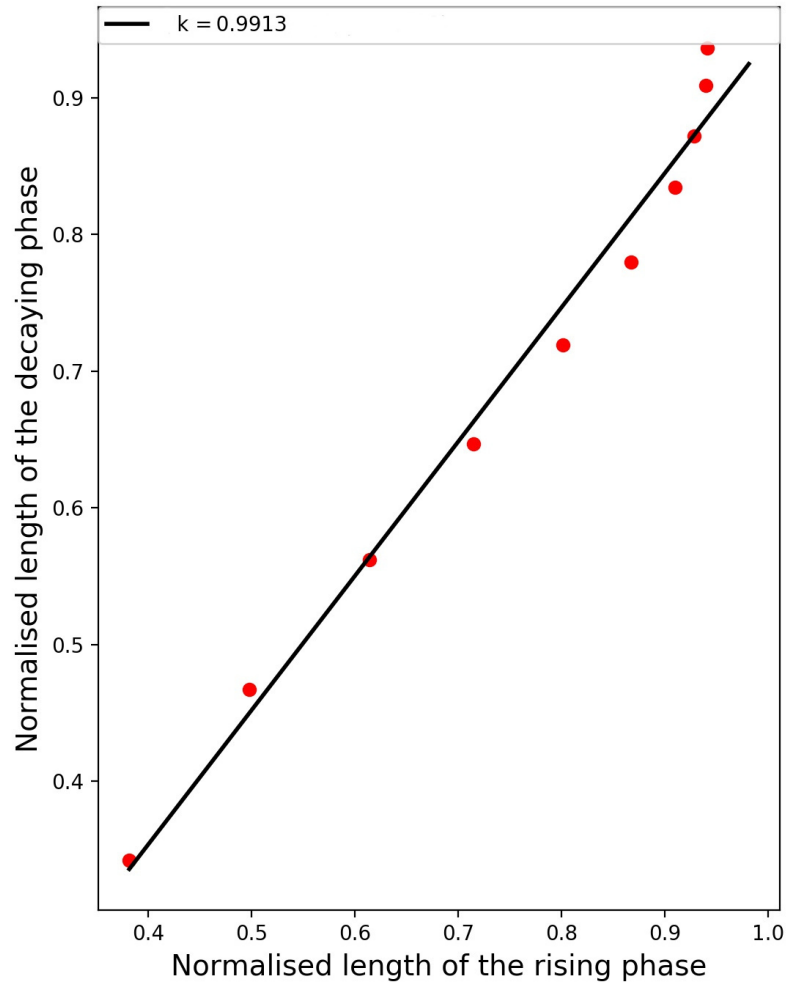
Figure 5.13: Ratio between the medians of the normalised boxplots in the rising phase and in the decaying phase.

evolves within. The driving mechanism, probably shock wave formation, magnetic reconnection or another energy release process, accelerates the plasma of the MS in the direction along the magnetic field. While the MS reaches up in solar corona, the plasma bulk can only move along the magnetic field line and cannot cross it in ideal MHD.

By inspecting the observed data, we took the medians of each box from Figure 5.12. The normalised time and length parameters are turned into physical parameters by multiplying them with the median of all the MS maximum lengths and lifetimes as discussed in Table 3.1. These

process yielded values of 27 Mm and 982 s, for the length and lifetime, respectively. These values represents the motion of an average MS in the solar atmosphere and serves as an observing reference for the modelling as displayed in Figure 5.15. Our aim is now to find a simple kinematic model and a parameter space that accounts for a well-fitted height profile to these points.

We apply now the following methodology in order to simulate the observed orbits of MS: since the 30.4 nm measurements of the *SDO/AIA* do not provide any information about the magnetic field configuration or plasma distribution of MS in LoS direction, MS are considered as neutral, spherical body displaying two-dimensional motion along an inclined slope. Such calculations were carried out by Timmerman & van der Weele (1999). This would mimic the frozen-in rise and descent of plasma motion along an inclined field line with *field-aligned* viscosity. The pitch angle of the slope is α, which relates to the tilt of the magnetic field line with respect to the solar limb. A MS is launched into α direction with a v_0 initial velocity from the $(0, 0)$ starting point. During their motion, three forces affect the ejecta: gravity, $\vec{F}_G$, the drag force of the surrounding environment, $\vec{F}_D$ and the normal force of the inclined surface, $\vec{F}_N$. Hence, the equation of the balance of the forces is:

$$\vec{F} = \vec{F}_G + \vec{F}_N + \vec{F}_D. \tag{5.1}$$

The position of the jet is described by two coordinates: ξ is the component parallel to the slope, η is perpendicular to it as displayed in Figure 5.14. The forces in this (ξ, η) coordinate system have the following components:

$$\begin{aligned}
\vec{F}_G &= \left(- g \cos \alpha, -g \sin \alpha \right), \\
\vec{F}_D &= \left(- \frac{1}{2} \rho_E v^2 C A, 0 \right), \\
\vec{F}_N &= \left(0, g \sin \alpha \right).
\end{aligned} \tag{5.2}$$

where v is the velocity of the bulb, g is the gravitational acceleration, A is the cross-section of the bulb, C is the drag-coefficient which is a function of the Reynolds-number, ρ_E is the density of the modeled MS. The velocity and acceleration in the η direction are 0 in order to model
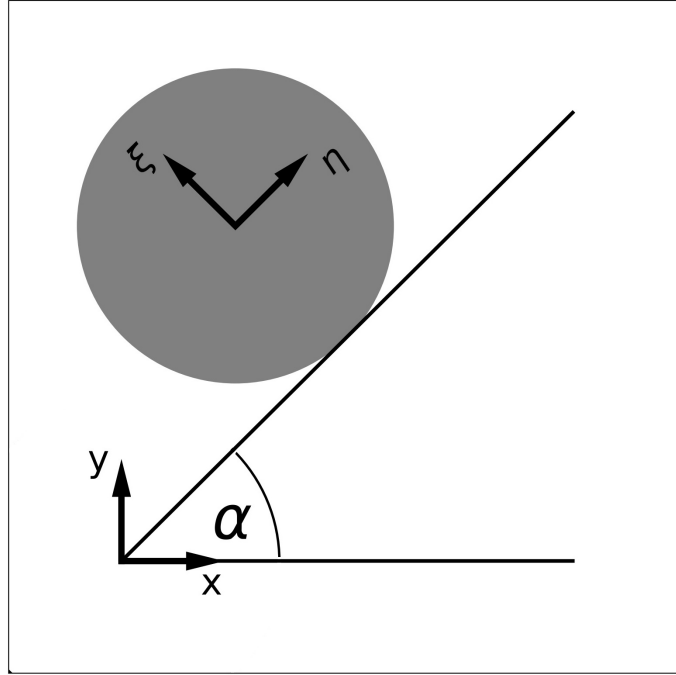
Figure 5.14: Schematic visualisation of our MS model. The gray circle represents the model body.

the frozen-in nature of the magnetic field lines. The acceleration in ξ, after rearrangement, can be expressed as:

$$a_\xi(t) = -Bv^2(t) - g\cos\alpha. \tag{5.3}$$

The motion of the body must be separated into a rising (RP) and a decaying phase (DP). After integration, the velocities are

$$v(t)_{\mathrm{RP}} = \frac{1}{2Bv}\ln\left\{\frac{g\cos\alpha + Bv_0^2}{g\cos\alpha + Bv^2}\right\},$$
$$v(t)_{\mathrm{DP}} = -v_t\tanh\left\{[t - t_{\max}]\frac{g\cos\alpha}{v_t}\right\}, \tag{5.4}$$

and the positions along the slope can be calculated as

$$\xi(t)_{\text{RP}} = \frac{1}{2Bv} \ln \left\{ \frac{\cos \left[\arctan(v_0/v_t) - tg \sin \alpha/v_t \right]}{\cos \left[\arctan(v_0/v_t) \right]} \right\},$$

$$\xi(t)_{\text{DP}} = \frac{v_t^2}{g \cos \alpha} \ln \left\{ \frac{[1 + (v_0^2/v_t^2)]^{1/2}}{\cosh \left[g \cos \alpha t/v_t - \arctan(v_0/v_t) \right]} \right\},$$

(5.5)

where g is gravitational acceleration. The parameters of the drag force are collected in

$$B = \frac{3}{8} \frac{\rho_E}{\rho_I} \frac{1}{r} C,$$ (5.6)

where $r = r(\xi)$ is the characteristic radius of the axially rotationally symmetric body (e.g. cylinder or cone) used to model the MS which is the function of the distance from the initial position, however, r is constant in the current calculations. ρ_I is the density of the surrounding environment. The so-called terminal velocity could be derived:

$$v_t = (g \cos \alpha/B)^{1/2}.$$ (5.7)

At this speed, the pulling force of the gravity equals with the drag force of the wind resistance. The epoch of maximal elevation is

$$t_m = \frac{v_t}{g \cos(\alpha)} \arctan \left(\frac{v_0}{v_t} \right).$$ (5.8)

In order to apply the model to the MS rise/fall and obtain the path of the "average" MS, which is i.e. comparable to the observations, we have fixed several parameters: $g = 0.244$ km s^2 is the gravitational acceleration at 40 Mm height in the solar atmosphere (Parenti et al., 2002), $r = 5$ Mm is the median of the width of all the MS, $\rho_I = 10^{-10}$ is the density of MS (Withbroe et al. 1976; Habbal & Gonzalez 1991). $\alpha = 85$ deg is set after analysing the tilt-angles of all the MS at the epoch of their maximum height. The free variables of the model are ρ_E, v_0 and C. Further requirement is that the body should reach zero length at the end of the modeled lifetime.

Figure 5.15 demonstrates a few model runs with the outcome of the best possible fit to the observations. Calculations were made 20 times in the temporal range of 982 s. We focus on two norms: i) the modelled MS
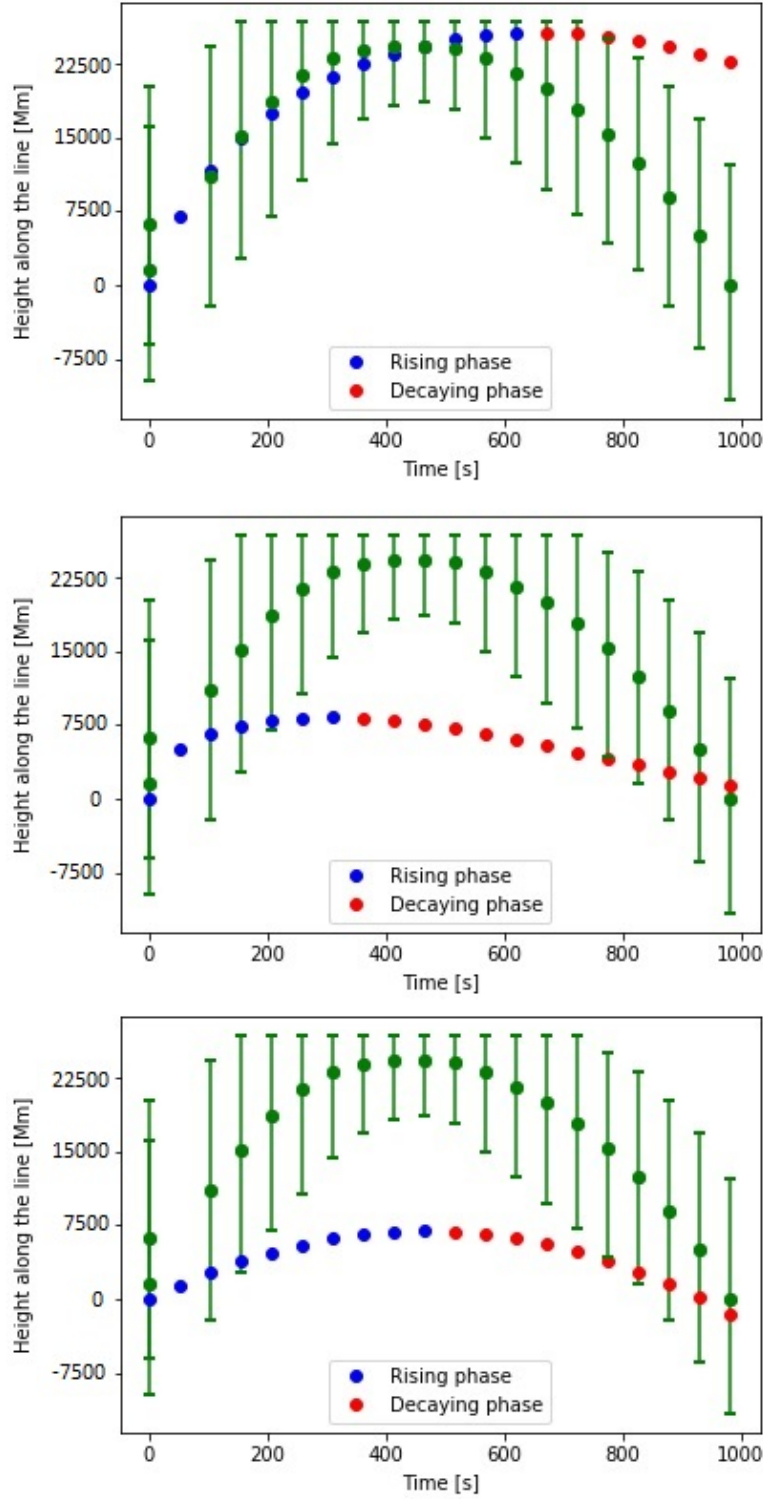
Figure 5.15: Three model runs on the trajectories of MS. Green points with error bars represents the observed orbits of MS. Blue and red points demonstrate the position of the modelled body in the rising and the decaying phase, respectively. The following values have been assigned to the free variables: top panel) $v_0 = 120 \text{ km s}^{-1}, C = 0.1, \rho_\mathrm{E}/\rho_\mathrm{I} = 10^{-1.85} \text{ kg m}^{-3}$; middle panel) $v_0 = 200 \text{ km s}^{-1}, C = 0.6, \rho_\mathrm{E}/\rho_\mathrm{I} = 10^{-1.9} \text{ kg m}^{-3}$; bottom panel) $v_0 = 20 \text{ km s}^{-1}, C = 0.6, \rho_\mathrm{E}/\rho_\mathrm{I} = 10^{-4} \text{ kg m}^{-3}$

is required to match the height parameters of the observing reference; and ii) the height of the modelled MS is demanded to be zero at the end of the simulation. The free parameters were determined in the following intervals:

- $0.1 < C < 3$

- $10^{-5} < \rho_{\mathrm{E}}/\rho_{\mathrm{I}} < 10^{-1}$ kg m^{-3}

- $10 < v_0 < 200$ km s^{-1}

After running the model with several different combinations of parameters, Figure 5.15 demonstrates a few examples of trajectory calculations. We were unable to complete the two norms on the same model. In order to reach to observed heights with the model, C and $\rho_{\mathrm{E}}/\rho_{\mathrm{I}}$ must be small. However, the gravity force is not enough for the modelled MS to return to zero height. On the other hand, v_0 should be small in order to reach a zero height at the end of the simulation.

5.2.2 Dynamic Approach

Further study of the decaying phase of MS requires a more sophisticated description. In order to achieve this goal, MS could be considered as neutral, free-falling bodies in the solar atmosphere. High-altitude free-falls in the atmosphere of the Earth has been both studied (Benacka, 2010) and modeled (Mohazzabi & Shea 1996; Anderson 2011; Colino & Barbero, 2013). Recently, Guerster & Walter (2017) conducted a study about the aerodynamics of a highly irregular body at transonic speeds. In their paper, the authors analysed the supersonic free-fall of Felix Baumgartner and also completed a dynamical simulation. In the current study, the methodology of Guerster & Walter (2017) has been applied to MS.

The governing equation, which describes the falling of a body from h altitude from the ground, is:

$$\frac{\mathrm{d}v}{\mathrm{d}t} = g(h) - \frac{1}{2}C\rho(h,T)\frac{A}{m}v^2. \tag{5.9}$$

The quantities used in the above governing equation are the following:
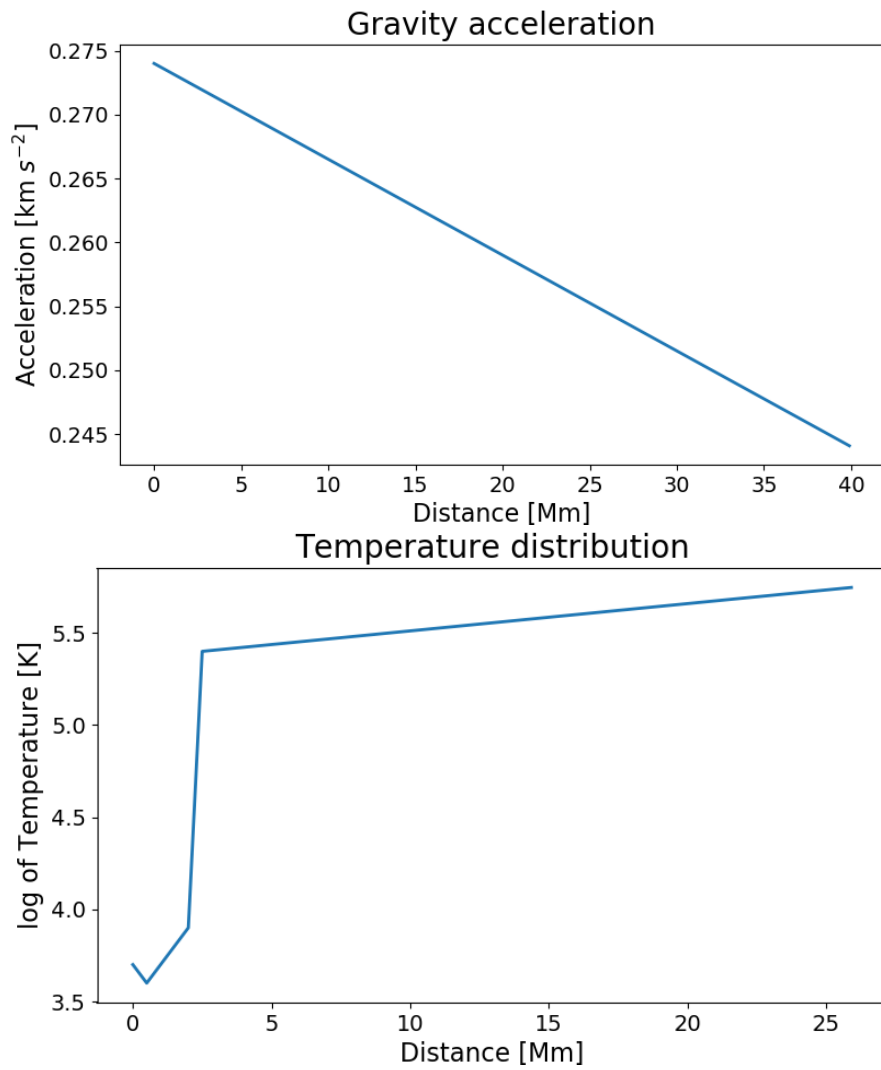
Figure 5.16: Top panel: gravity acceleration profile between 0 Mm and 40 Mm height. Lower panel: temperature profile of the solar atmosphere based on the VAL IIIc model (Vernazza et al., 1981).
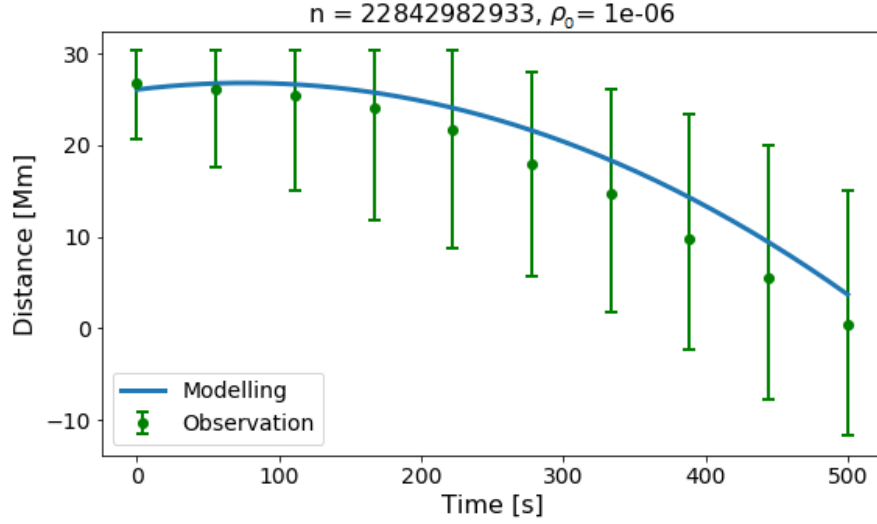
Figure 5.17: Model run with $n \sim 10^{10}$ cm^{-3}, $\rho_0 \sim 10^{-6}$ kg m^{-3} and $v_0 = 0$. Green points with error bars represent the observations of the MS trajectories, blue line indicates the simulated trajectory.

- g is the gravity acceleration, varying between $0.244 - 0.274$ km s^2 from the solar surface to 40 Mm height in the lower corona (Parenti et al., 2002).

- C is the drag coefficient, which is function of the Reynolds number and the Mach number. The drag coefficient of a sphere is 0.5.

- ρ is the density of the surrounding area. The density distribution of the solar atmosphere has been adopted from the VAL IIIc model (Vernazza et al., 1981).

- A is the aerodynamically wetted area. This is the area of the body, which is in contact with the external airflow, hence, has a direct relationship with the aerodynamic drag of the body. In the current study, this is the area of a hemisphere with diameter as the width of a MS.

- m is the mass of the body. This quantity is estimated as the mass of a sphere with the diameter (5 Mm) and number density n (10^{10}, Withbroe et al. 1976; Habbal & Gonzalez 1991) of a MS.

Also, the instantaneous terminal velocity must be calculated:

$$v_{t0} = \frac{2mg}{C\rho_0 A},\tag{5.10}$$

where ρ_0 is the surface density. This velocity is not constant as the body is moving across the atmosphere. The density of the atmosphere is changing according to the barometric formula

$$\rho = \rho_0 \exp\left(-\frac{h-h_0}{H}\right),\tag{5.11}$$

with the scale-height H:

$$H(T) = \frac{TR_S}{g_0},\tag{5.12}$$

where T is the temperature and the $R_S = 286.91$ J kg^{-1} K^{-1} is the gas constant of the standard atmosphere. The derived equation of motion is:

$$\frac{1}{g}\frac{\mathrm{d}v}{\mathrm{d}t} = 1 - \frac{v^2}{v_{t0}^2}\exp\left(-\frac{h(t)-h_0}{H}\right).\tag{5.13}$$

To the best of our current knowledge, this equation has no indefinite integral. Nevertheless, the measurement of a MS position was not taken with infinitesimally small timescale, and a Δv velocity variation of MS was observed during a Δt interval. Hence, Δv could be estimated with the Taylor series of

$$\Delta v = \delta v - g\left(1 - \frac{v_0^2}{v_{t0}^2}\right)\Delta t + \frac{v_0 g^2}{v_{t0}^2}\left[1 - \frac{v_0^2}{v_{t0}^2} + \frac{v_0^2}{2gH}\right]\Delta t^2 + \cdots,\tag{5.14}$$

where $v_0 = v(t=0)$ is the initial velocity and δv is the estimated velocity of the previous step. The variation of the gravity acceleration is ignored due to the large distance from the core of the Sun. The temperature variation is taken from the VAL IIIc model Vernazza et al. (1981). The utilized temperature and gravity distributions are presented in Figure 5.16. In the calculations, two free-parameters are considered: the m mass (therefore, the n number density) and the ρ_0 surface density.

The falling of the blob modelling a macrospicule begins at the chracteristic height of 27 Mm and the modeling ends after a characteristic

time of 490 s, which are the median of the observed maximum length and lifetime distributions of MS as stated in Table 3.1. If $v_0 = 0$, than the second term in Equation 5.14 disappears.

From Figure 5.17, it is visible that only the gravitational acceleration can produce a path, which matches the measured trajectory of MS without any other forces.

To simulate the effect of the drag force, a small initial velocity ($v_0 \sim 20$ km s^{-1}) is considered. Figure 5.18 displays a model running with typical parameters observed on the Sun: $n \approx 10^{10}$ cm^{-3} and $\rho_0 \approx 10^{-6}$ kg m^{-3}. The modelled trajectory remains relatively close to the measured height values. However, in order to validate the behaviour of this solution, the input parameters must be investigated on a wider range. In Figure 5.19-5.20, a range of n and ρ_0 input parameters are used Equation 5.14. Particularly: $n \approx 2 \times 10^3$, 2×10^5, 2×10^8, 2×10^{10} cm^{-3} and $\rho_0 \approx [10^2, 10, 1, 10^{-6}$ kg m^{-3}. By varying these parameters, the model runs relatively quickly tending towards a solution, which seems to be sustained from any further input variation. This particular solution is generated with a pair of parameter values around 10^4 cm^{-3} for MS number density and 10^{-6} kg m^{-3} for surface density.

More information would be necessary to model the plasma environment around the bulk. MS are considered to move inside a cylinder. The density variation inside the cylinder was estimated according to the barometric density formula in Equation 5.11. Three parameters are considered here: the surface density ρ_0, scale-height H and the length of the cylinder L. To keep the modelling close to the observed properties of the solar atmosphere, the surface density is taken 10^{-6} kg m^{-3}. The gravitational scale-heights are characterised with gained three values for the analysis and remained independent from altitude: $H = 10^3, 10^4$ and 10^5 km, respectively. The scale-height up to 10^3 km is a typical value between photosphere and the chromosphere, while employing $H \approx 10^4$ km determines the density variation of the lower solar corona. $H \approx 10^5$ km could be possibly measured in the mid-upper corona. Moreover, since the density variation only has altitude dependence, the entire problem is turned now into a one-dimensional problem.

In order to be considered this modelling physically valid, the altitude of the centroid of the density distribution must is requested to 27 Mm

height as seen in the observations. Figure 5.21 shows the different model runnings, plotted according to the value of the scale-height. It is clear that $H = 10^3$ km scale-height does not provide an applicable solution: L could be enlarged up to nearly 200 Mm, the altitude of the centroid only grows by 1.5 Mm. In the case of $H = 10^5$ km, the altitude of the centroid varies significantly even for a minor enlargement of the cylinder. The ideal solution appears to be of the order of $H = 10^4$ km and this is a physically reasonable parameter in the upper solar corona, where the MS could reach up to.

To give a more sophisticated solution, the following requirements are to be satisfied: i) the height of the model cylinder shall not be larger than 80 Mm (this is the height of the longest MS); and ii) the centroid of the cylinder shall be at around 27 ± 3 Mm in altitude.

Figure 5.22 displays density distribution simulations with $H = 8, 15$ and 22 Mm scale-heights and $L = 50, 60$ and 80 Mm maximum heights. According to calculations, the modelled bulk would start free-falling from the height of 27 Mm in barometric atmosphere with 10^{-6} kg m^{-3} density at the solar surface, if the scale-height is between 15 and 22 Mm and the plasma column reaches up to 80 Mm.

According to these calculations, it is possible to describe the downward motion of MS based on a non-magnetic kinetic model. The main factor, which seems to influence the trajectory of MS, is gravity. However, to describe the entire motion of these jets from their first appearance until the falling under the solar limb, the effect of the electromagnetic processes must be likely to be taken into account as well. MS are likely not bodies of neutral gas and they are generated and driven in a strongly magnetised environment, therefore, their motions are strongly influenced by magnetic forces.
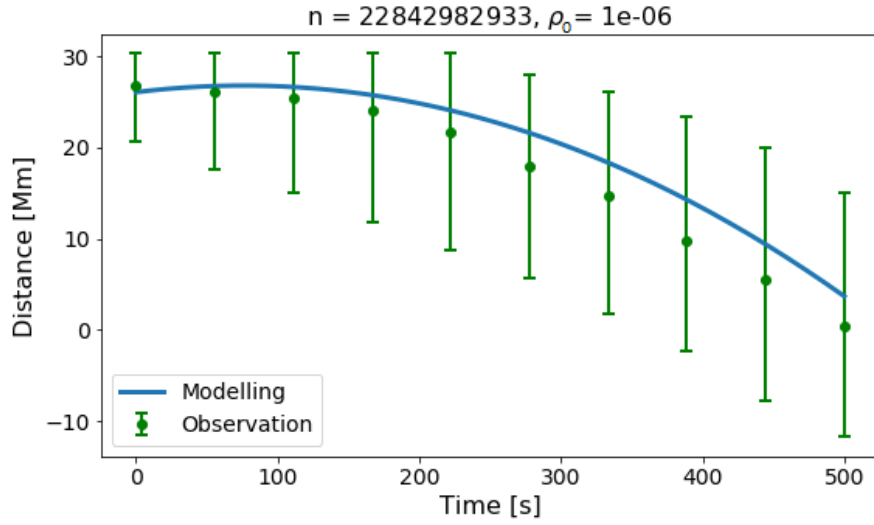
Figure 5.18: Model runs of the free-falling bulk with corresponding solar parameters: $n \approx 10^{10}$ cm^{-3} and $\rho_0 \approx 10^{-6}$ kg m^{-3}. Green points with error bars represent the observations of the MS trajectories, blue line indicates the simulated trajectory.

5.3   Conclusions

In this chapter, we investigated the motion of MS in the solar atmosphere. In the first part of the chapter, we analysed the dataset of our observations. In the second part, a simple physical model was constructed to model the kinematics of MS and compare them results to the observations.

The actual height of each MS was measured during their entire lifetime. After placing all of these timesets together, we calculated a density profile of these time-length distribution and identified higher and lower density areas. The high-density regions tended to follow a parabola-like feature. This nature of MS evolution turned up during the individual analysis of two MS subclasses. In order to investigate the parabola-like behaviour, MS were separated into four groups based on their lifetime. The time-spans of each groups were the following: 1) 0 – 534 s; 2) 535 – 1068 s; 3) 1069 – 1602; 4) 1602 – 2136. By determining the point density profile of each groups, the parabola-like trend in the height variation was obvious. Each group was divided into nine subgroups in time. With the application of boxplots, the median and the spreading of the heights were
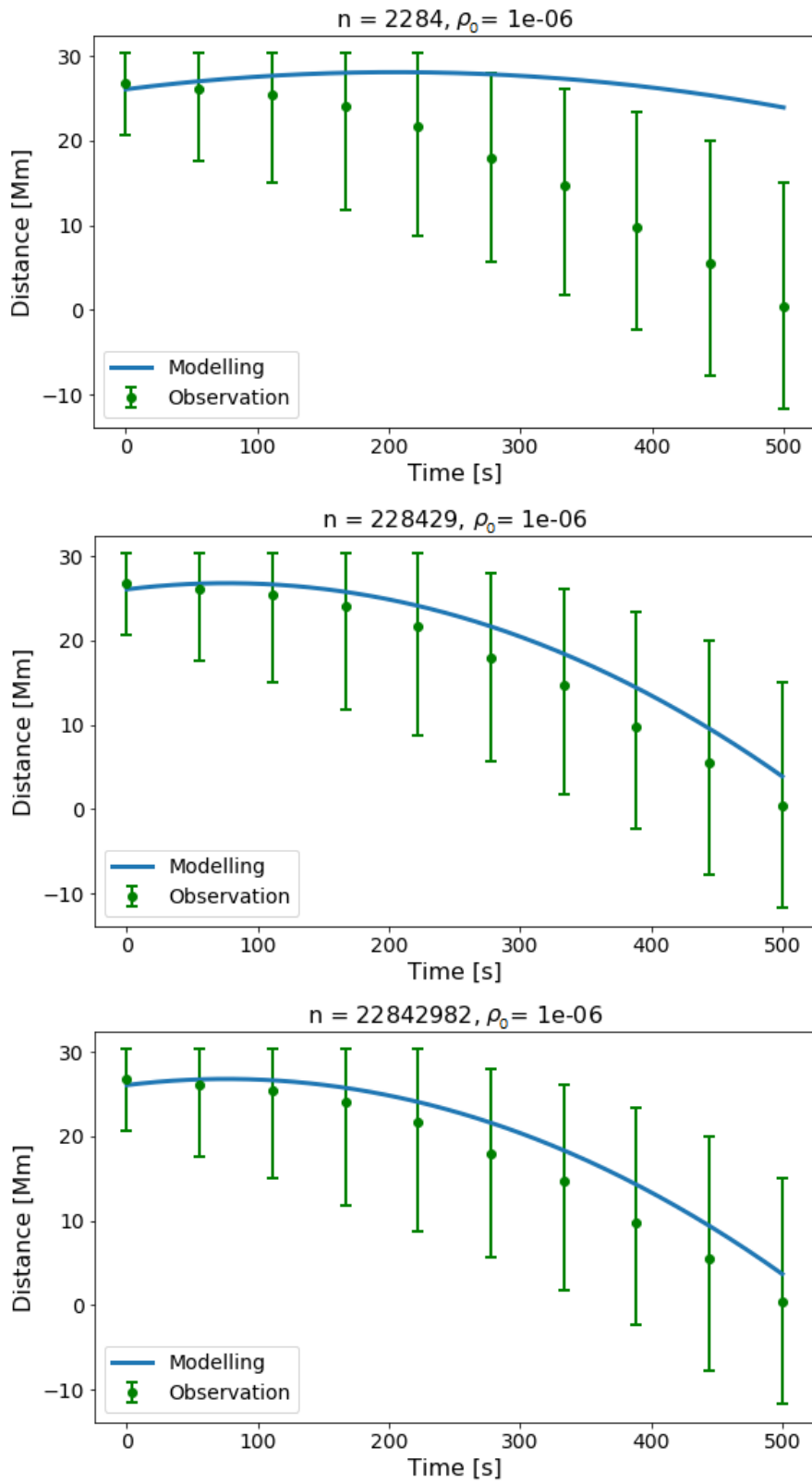
Figure 5.19: Model runs of the free-falling bulk with changing number density of the bulk. Green points with error bars represent the observations of the MS trajectories, blue line indicates the simulated trajectory.
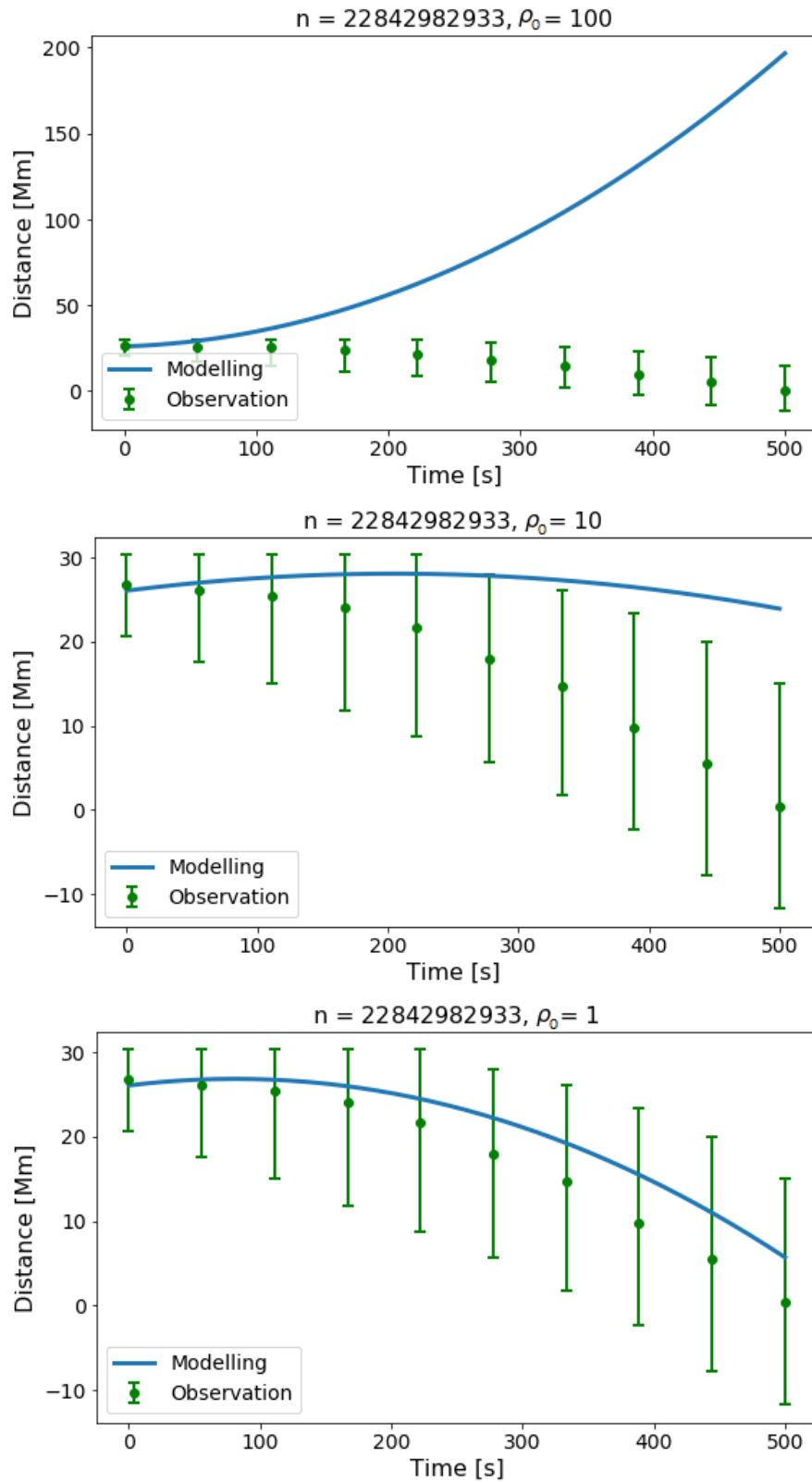
Figure 5.20: Model runs of the free-falling bulk with changing surface density. Green points with error bars represent the observations of the MS trajectories, blue line indicates the simulated trajectory.
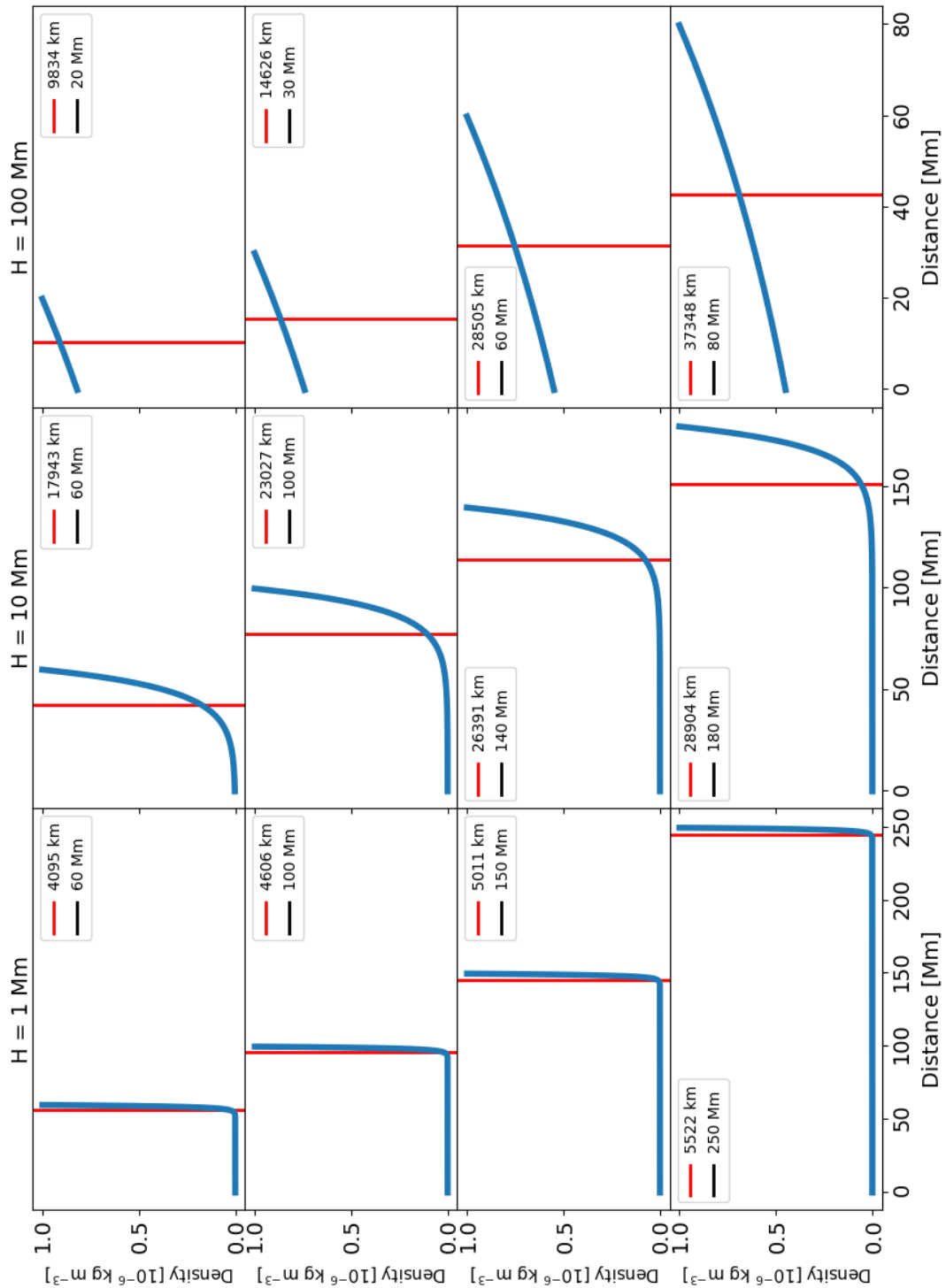
Figure 5.21: Modelling the barometric atmosphere with 1, 10 and 100 Mm scale height (from left column to right column). Blue line represents the simulated density, the red vertical line shows the altitude of the centroid and the actual associated value is given in the legend inlet. The height of the model cylinder representing an MS varies and its value displayed in the legend of each plot after a black line.
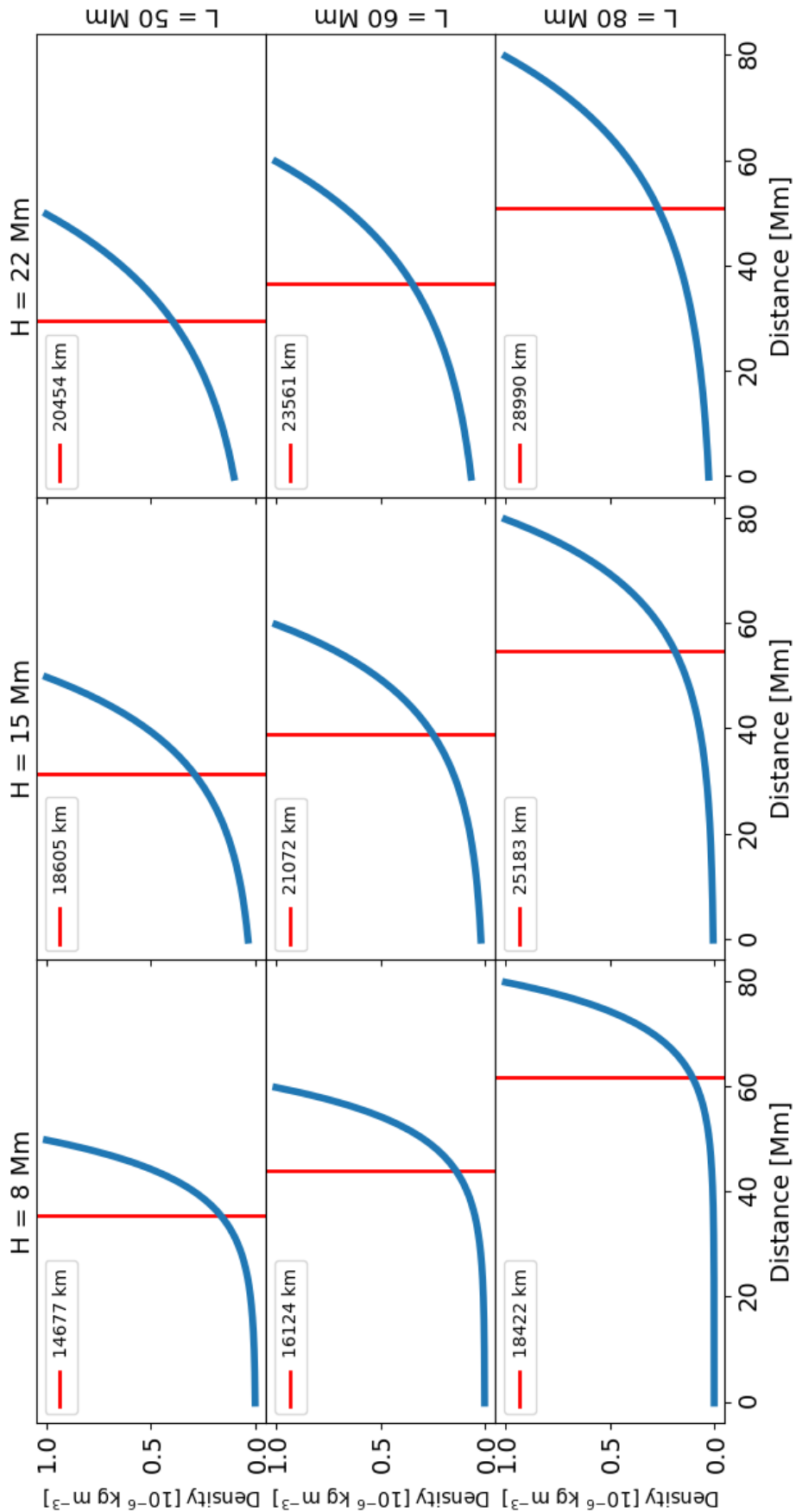
Figure 5.22: Modelling the barometric atmosphere with 8, 16 and 22 Mm scale height (from left column to right column). Blue line represents the simulated density, the red vertical line shows the altitude of the centroid. The height of the cylinder varies from top to bottom: 50 Mm, 60 Mm and 80 Mm, respectively.

resolved for each subgroup. The difference between the orbits of CH-MS and QS-MS were estimated by subtracting the corresponding medians in each groups: CH-MS turned up to be longer during their entire lifetime.

Since, in our criteria, the starting point of each MS was the appearance of a brightening under the solar limb, we detected MS under the limb for a short time in the beginning of the rising phase. However, the final epoch of MS detection was the falling back of the top point of the jet under the solar limb. This feature could lead to a biased interpretation. For this reason, we excluded the under-the-limb phase of MS evolution. Then, we carried out a similar analysis on the over-the-limb datasets like we did on the raw dataset. After calculating the differences between the medians of height in each time-span groups, CH-MS were still significantly longer than QS-MS. The analysis of the duration of the rising and the decaying phase revealed an another difference between the two subclasses. Nearly 62% of the QS-MS have a longer decaying time, while 74% of CH-MS have a longer rising phase. Possible source of the observed deviances could be the different magnetic field topology in the coronal holes and quiet Sun regions.

Next, we made a consideration that all the MS are generated and driven the same way. The only differences between them were their height and lifetime. Therefore, we have individually normalised the length and lifetime of all MS and analysed the normalised timesets together. With the application of boxplots, we were able to determine the trajectory of an "average" macrospicule.

In order to study the kinematics of MS in more details, we constructed a simple model. In this model, a MS was represented as a neutral, spherical bulk. Our goal was to construct an orbit of the modelled body and make it as similar to the observed, normalised trajectory as possible. After implementing several different varieties of input parameters into this model, the current version of model was not able to match the motion of MS entirely.

Also, a dynamical model was built to simulate MS as free-falling neutral bulks in the solar atmosphere. The utilized conception was created to imitate the motion of a free-falling body in the terrestrial atmosphere, but several properties have been applied such as temperature variation or gravity acceleration of the solar atmosphere. The down-falling motion

of MS could be simulated within statistical error to the observations by considering physically reliable input parameters. The dominant force in this system is gravity. The drag force seems to act a minor role in comparison to gravity. Furthermore, MS were described as neutral plasma cylinders with barometric density profile. The altitude of the release point of the bulk was considered to be the centroid of the cylinder. To model the observed heights of MS, the scale-height was required to be between 15 and 22 Mm and the plasma column needed to reach up to 80 Mm.

Chapter 6

Conclusions and Outlook

6.1 Summary Overview of the Thesis

This Thesis aims to study the long-term variation of the physical properties of short-lived localised chromospheric ejecta, the macrospicules (MS). The basis of this research is a dataset built-up from a self-consistent and vigorous definition system applied to a multiple-year-long observation campaign with a high sampling cadence. The applied criteria focused MS to be selected from the dense and dynamic region of the "chrompsheric zoo". The information obtained may indicate a key potential relationship between short-lived jets and the large-scale variation of the global magnetic field of the Sun. The obtained results of our investigation about the evolution of MS over a long time support the conjecture that MS formation could be connected both spatially and temporally to the so-called Quasi-Biennial Oscillations (QBOs), which were discovered in several solar activity proxies.

Chapter 1 of the Thesis presented a short introduction to several fundamental topics related to the research area of MS. Firstly, the structure of the solar corona was discussed through several physical variables like temperature or density. The Thesis embarked to find connections between MS and the solar activity, therefore, a brief introduction to the activity of our star was given here. Lastly, a comprehensive historical survey outlined MS observation and modelling over the past few decades.

A detailed critical description is outlined for the introduced definition

criteria of MS for our research along with the digitalization method of the implemented tetragon approximation and the observing campaign in Chapter 2. Additionally, the data pipeline of the *Solar Dynamics Observatory* and its *Atmospheric Imaging Assembly* is discussed as the primary source of the employed observations. A summary of the studied solar activity proxies and the mathematical/statistical toolkit are also presented in this Chapter.

The temporal evolution of several physical properties of MS is studied in Chapter 3. The physical properties of each jet were measured during their entire lifetime and summarised. For the current research, the following quantities have been utilized: maximum length, maximum area, maximum width, average velocity and lifetime. The characteristic values of each dataset were estimated with a log-normal fitting in their corresponding histograms. However, these data had to be validated: after a direct comparison, parameters of MS in the dataset were confirmed to be consistent with the results of previous studies in the literature. After all possible pairs of physical properties were cross-correlated with each other, strong correlations are only found in a number of cases. However, and perhaps most importantly, a significant temporal trend was found in all cross-correlation data: by considering the progress, each timeset oscillates around its fixed-point with a nearly two-year-long period. Such oscillations were found in the raw datasets of each MS physical property. The "Maximum length", "Maximum area" and "Average velocity" datasets of MS indicated a clear presence of QBOs. These oscillations have been compared to QBOs in the time-series of complementary solar activity proxies. A comparison with solar activity proxies that also possess the properties of QBOs provides some interesting features: the minima and maxima of QBOs of MS properties occur at around the same epoch as the minima and maxima of these activity proxies. For most of the time span investigated, the oscillations are out of phase. This out-of-phase behavior was also corroborated by a cross-correlation analysis.

In Chapter 4, we focused on the spatial distribution of MS around the solar disk. Here, a number of the measured physical properties of each jet were studied with respect to their latitudinal position. The generation rate of MS between the two hemispheres turned up to be largely different: nearly 60% of the ejecta were formed in the southern hemisphere. A new

parameter was also introduced here: the distance of each MS from the poles. As MS are mainly formed around the solar poles, this newly introduced quantity provided an easier way to analyse their position. The nature of two MS subclasses was found to be quite distinct: while CH-MS showed a strong oscillatory pattern temporally, the distance of QS-MS from the poles did not present any strong variations. By applying appropriate clusterization methods to the data, a clear two-year-long oscillatory pattern is revealed in the CH-MS data. The epoch of the boundaries of four identified clusters are found to be close to those dates where the QBOs in the temporal variation of MS physical parameters reached their local maxima, as discussed in Chapter 3.

The trajectories of each MS were analysed in Chapter 5. By investigating the orbits of all MS in the database, a significant trend was visible in the data. MS followed a parabola-like trajectory, which would indicate a dominant influence of gravity on their motion. However, the rising phases and the decaying phases of each jet were not equal: line-fitting on their cross-correlation provided a weak linear coefficient. Nevertheless, CH-MS had a longer rising time than decaying duration in 74% of the samples. Opposite to this, 62% of all QS-MS had a longer decaying phase than rising phase. After normalising all the MS trajectories both in time and space, the corresponding medians of boxplots of the normalised length in the early and the late phase of MS lifetime were cross-correlated and a strong linear correlation was found.

Next, we have built up a simple physical model on the kinematics of MS. This model considered MS as a neutral, spherical body moving along an inclined slope. This slope represented the frozen-in rise and decent of plasma motion along an inclined magnetic field line. The free parameters, such as viscosity and the density of the medium around the MS, were set to be constant. With this model, we were able to carry out simulations on the kinematics of the jets as a first approach. However, if the modelled body reached the previously observed heights, its length was not zero at the end of the simulated lifetime. For this reason, the construction of a more advanced model is necessary.

A dynamical model was also constructed in order to simulate the downward motion of the jets. In this construction, MS were considered as free-falling natural bulks in the solar atmosphere. This model was

designed to simulate free-falling bodies in the terrestrial atmosphere, but the implementation of the parameters of the solar corona revealed the strong influence of gravity on the motion of MS. Drag force appeared to be a less dominant factor. Moreover, MS were also simulated to be cylindrical bodies with a barometric density structure. By estimating the centroid of this density distribution, the scale-height of the density profile and the length of the cylinder were be determined to simulate the 27 Mm altitude, where the down-falling of MS begins.

6.2 The Double Solar Cycle

To give a plausible explanation to the previously described nature of MS, we propose the following theoretical conjecture. Macrospicules could be considered proxies of the higher-frequency component of the double solar cycle. Two aspects of the behaviour of MS should be recognised here: the migration pattern from the solar poles with a nearly 2-year periodicity and the fact that MS reach the maxima in their physical properties around the epoch of the return to the solar poles. The extent of the global magnetic field, which generates MS, expands and MS may appear at lower solar latitudes. Due to this expansion, the magnetic flux decreases and the physical dimensions of MS become small. After this point in time, the global magnetic field contracts back towards the solar polar regions. However, the magnetic flux increases, and MS grow physically greater. This hypothesis could give a reasonable explanation both for the migration of the formation locii of MS and their size variation.

The nature of QBOs is visualised in Figure 6.1. After considering the previously described behaviour of the higher-frequency component, the expansion/contraction of the field is represented with triangles between the poles and high solar latitudes. However, the nature of the higher-frequency component between high latitudes and the equator is still an open question. For this reason, the bars that represent the QBOs between the higher solar latitudes and the solar equator, are semi-transparent. The investigation of other locally formed solar activity indicators (i.e. solar faculae) featuring on global scales could give additional information about the conjecture of the existence of the double solar dynamo at these solar latitudes. Dark-grey ellipses around the solar equator represent the nearly 11-year-long cycle. Circled hatches illustrate regions where the polarity of the leading sunspots is northern, dotted hatches show the southern one. The 11-year long cycle must also follow the migration of sunspots from higher latitudes to the equator through a solar cycle. Around the poles, the triangles represent the behaviour of the high-frequency component indicated by the MS. Between the "butterfly wings" and the poles, light-grey territories illustrate the cycles of QBOs. Corresponding to the 11-year-long oscillation, the striped and crossed hatches distinguish the cycles of the two dominant polarities.
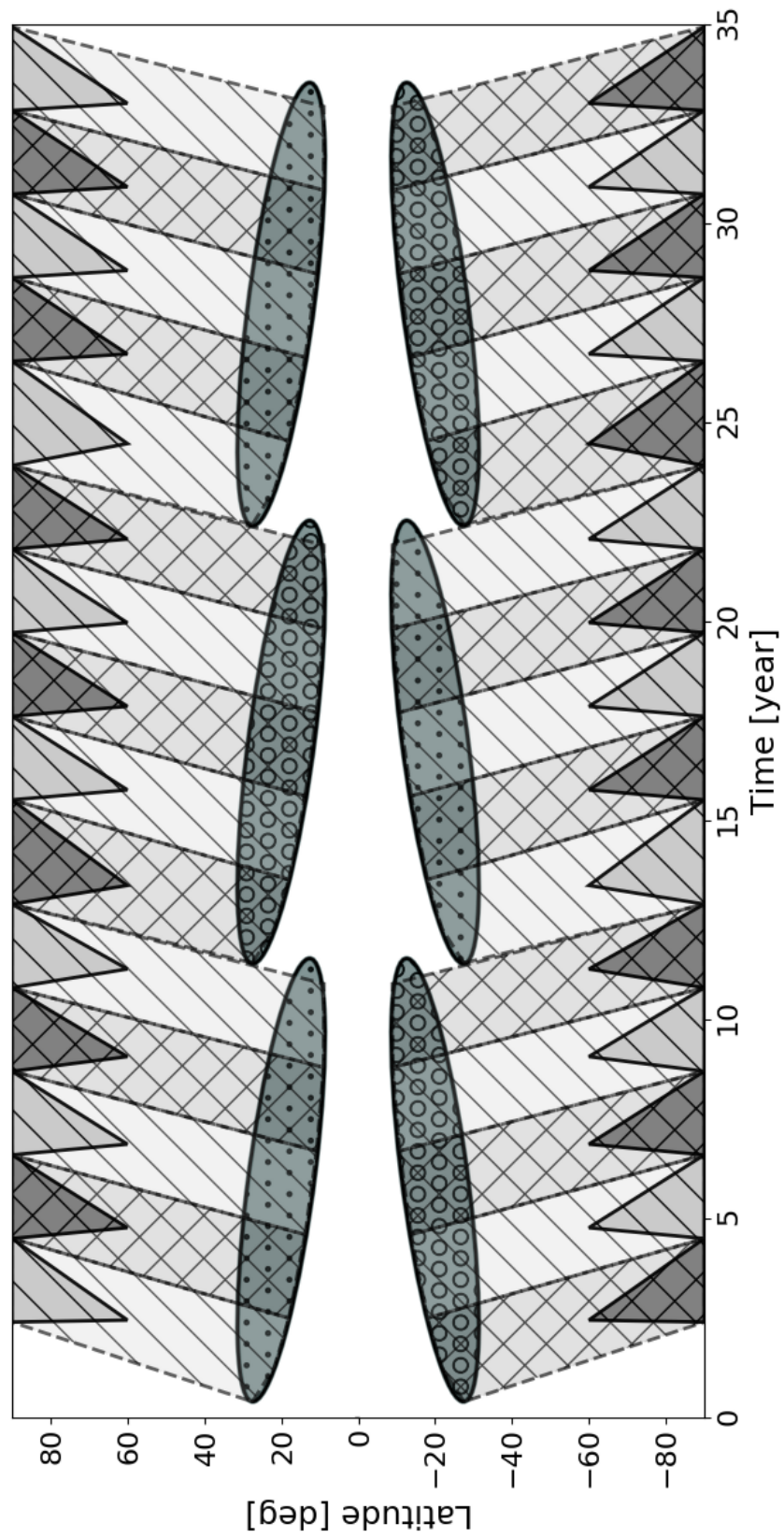
Figure 6.1: Schematic concept visualising the spatial distribution of the double solar magnetic cycle.

6.3   Future Works

This Thesis aims to answer questions about the generation and evolution of chromospheric macrospicules. The dataset gathered gathered by us so far is more extensive in its population and its duration than any other known and available jet dataset. However, there are several aspects, where further development is possible as it is outlined:

- **Improvement of the current dataset:**

    - *Gathering data on more MS:* The addition of more jets with the same methods and instruments would raise the duration of the dataset close to the nearly 11-year-long span of the solar cycle. Direct comparison of the long-term evolution of MS to the solar cycle is a yet unexplored area of research.

    - *Shape recognition:* There may exists better ways than the tetragon approximation to estimate the physical parameters of MS. Contouring MS intensity map observations and determining a threshold as a boundary of the MS would be a step forward.

- **Multi-line or/and multi-instrument observation:** This Thesis studied MS using the images of the *SDO/AIA* 30.4 nm channel. As it was stated earlier, these observations did not provide any information about the Line-of-Sight extent of the jets. The addition of such information on MS would grant a better insight into the complex physical system of the jets. Earlier studies claimed that MS are multi-thermal objects. Therefore, the analysis of MS in other chromospheric or/and coronal lines would be essential for further developments.

- **Automatization:** This step would be a ground-breaking improvement towards generating a much larger MS database. By the application of e.g. machine learning methods with shape recognition capability, this would enable us to teach the computer the basic characteristics of MS recognition.

- **Modelling:** The model, what we have constructed for the study of the kinematics of MS in Chapter 5, was a simple one. Adding a

height dependence to the density of the media around the MS and to the viscosity would be a beneficial way to improve the model.

Chapter 7

Appendix

In the following tables, all the data about the identified MS are summarized. The columns are the following:

- **Date of observation:** The date in Year-Month-Day format, when the MS was visible in the solar limb.

- **Start time:** The epoch in Hour-Minute format, when the brightening of the MS appeared under the solar limb.

- **End time:** The epoch in Hour-Minute format, when the top point of the MS fell under the solar limb.

- **Duration:** The time duration between the start time and the end time of the MS in minutes.

- **Position:** The angular position of MS. This angle is calculated counter-clockwise from the western end of the solar equator on the solar disk.

- **Type:** The subclass of the MS: coronal hole [CH], coronal hole boundary [CHB] or quiet sun [QS].

#	Year	Month	Day	Hour	Minute	Hour	Minute	Duration [minute]	Position [deg]	Type
	Date of observation			**Start time**		**End time**				
1	2010	6	1	12	52	13	7	15	5.62	QS
2	2010	6	1	12	54	13	3	9	0.13	QS
3	2010	6	15	12	42	13	6	24	1.64	CH
4	2010	7	7	12	13	12	36	23	0.88	QS
5	2010	7	7	13	18	13	40	22	1.25	CH
6	2010	7	15	12	3	12	20	17	1.38	CH
7	2010	7	15	12	13	12	24	11	0.80	QS
8	2010	7	24	12	0	12	16	16	2.25	QS
9	2010	8	1	13	12	13	38	26	5,21	QS
10	2010	8	7	12	30	12	45	15	4,81	CH
11	2010	8	15	13	2	13	18	16	1.05	QS
12	2010	8	24	12	38	12	56	18	1,73	CH
13	2010	8	24	13	14	13	29	15	1,47	QS
14	2010	9	1	12	34	12	53	19	4,86	CH
15	2010	9	15	12	14	12	31	17	1.79	CHB
16	2010	9	15	12	14	12	34	20	4.39	QS
17	2010	9	15	12	21	12	40	19	1,51	CH
18	2010	9	15	12	56	13	14	18	4.56	CH
19	2010	9	24	12	25	12	44	19	5,26	CH
20	2010	10	15	12	22	12	40	18	1,48	CH
21	2010	10	24	12	28	12	49	21	4,18	QS
22	2010	11	1	12	34	13	0	26	5,16	CH
23	2010	11	1	12	46	13	2	16	1,62	CH
24	2010	11	7	12	15	12	35	20	4,67	CH
25	2010	11	7	13	14	13	26	12	1,88	QS
26	2010	11	15	12	4	12	19	15	4,88	CH
27	2010	11	15	12	6	12	21	15	1,55	CH
28	2010	12	1	13	34	13	56	22	1.52	CH
29	2010	12	7	12	0	12	13	13	1,77	CH
30	2010	12	15	12	7	12	32	25	4,67	CH
31	2010	12	24	12	14	12	40	26	3,94	QS
32	2010	12	24	13	12	13	31	19	4,30	QS
33	2011	1	1	12	56	13	14	18	1,86	QS
34	2011	1	1	13	42	13	52	10	5.11	CH
35	2011	1	15	12	1	12	15	14	1.94	QS
36	2011	1	15	12	47	13	1	14	1,54	CH
37	2011	1	15	13	44	13	58	14	0,79	QS
38	2011	1	24	12	14	12	34	20	5,15	CH
39	2011	1	24	12	31	12	53	22	4,78	CH
40	2011	1	24	13	24	13	41	17	5,54	QS
41	2011	2	1	13	12	13	24	12	1.24	QS
42	2011	2	1	13	30	13	43	13	4.64	CH
43	2011	2	7	12	2	12	19	17	1,35	CH
44	2011	2	7	13	11	13	30	19	1,42	CH
45	2011	2	15	13	42	13	58	16	0.86	QS
46	2011	2	24	12	25	12	39	14	4,51	CH
47	2011	2	24	12	39	13	3	24	1,54	CH
48	2011	3	1	12	16	12	30	14	4.65	CH
49	2011	3	1	13	9	13	28	19	6.17	QS
50	2011	3	15	12	0	12	24	24	5.92	QS

#	Date of observation			Start time		End time		Duration [minute]	Position [deg]	Type
	Year	Month	Day	Hour	Minute	Hour	Minute			
51	2011	3	15	13	9	13	19	10	5.20	CH
52	2011	3	24	12	40	12	56	16	5,42	CH
53	2011	3	24	13	41	13	59	18	5,43	CH
54	2011	4	7	13	29	13	50	21	4,85	CH
55	2011	4	15	12	39	12	58	19	1,45	CH
56	2011	4	15	12	45	13	1	16	2,27	QS
57	2011	4	24	12	23	12	36	13	4,89	CH
58	2011	5	7	12	28	12	47	19	1,68	CH
59	2011	5	7	13	32	13	55	23	0,90	QS
60	2011	5	15	13	18	13	37	19	1.73	CH
61	2011	7	1	12	49	13	13	24	4.56	QS
62	2011	7	1	12	58	13	8	10	1,70	CH
63	2011	7	1	13	19	13	41	22	4,54	QS
64	2011	7	1	13	25	13	44	19	4,76	CH
65	2011	7	7	12	51	13	3	12	5,01	CH
66	2011	7	15	13	18	13	42	24	4,93	CH
67	2011	7	24	12	43	13	4	21	1,89	CH
68	2011	8	1	12	30	12	48	18	5.16	CH
69	2011	8	7	12	41	12	54	13	1,61	CH
70	2011	8	15	12	46	12	58	12	4,70	CH
71	2011	8	24	12	44	13	1	17	3,81	QS
72	2011	8	24	12	34	12	53	19	2,12	QS
73	2011	9	1	12	0	12	13	13	5,27	CH
74	2011	9	24	12	46	12	58	12	4,84	CH
75	2011	10	1	12	22	12	36	14	5,34	CH
76	2011	10	7	13	0	13	17	17	4,84	CH
77	2011	10	15	12	5	12	27	22	5,19	QS
78	2011	10	15	12	15	12	36	21	4,03	QS
79	2011	11	1	12	16	12	32	16	1,62	CH
80	2011	11	1	13	4	13	17	13	4,86	CH
81	2011	11	7	13	22	13	35	13	1,63	CH
82	2011	11	7	13	23	13	42	19	4,63	QS
83	2011	11	24	13	15	13	29	14	3,98	QS
84	2011	12	1	13	11	13	30	19	1,97	QS
85	2011	12	7	13	36	13	53	17	4,54	CHB
86	2011	12	15	13	32	13	48	16	5,48	QS
87	2012	1	1	12	44	13	2	18	5,39	QS
88	2012	1	1	13	31	13	54	23	4,66	CH
89	2012	1	24	12	7	12	30	23	5,06	QS
90	2012	2	1	12	9	12	27	18	0,79	QS
91	2012	2	1	12	14	12	32	18	2,15	QS
92	2012	2	1	12	25	12	41	16	5,64	QS
93	2012	2	1	12	38	12	50	12	4.35	QS
94	2012	2	1	13	21	13	48	27	3.91	QS
95	2012	3	1	12	19	12	29	10	1.41	CH
96	2012	3	1	13	14	13	29	15	5.05	CH
97	2012	3	7	12	20	12	43	23	1,92	QS
98	2012	3	7	12	50	13	6	16	3,98	QS
99	2012	3	7	12	56	13	10	14	1,17	QS
100	2012	4	1	12	45	13	8	23	0.94	QS

#	Date of observation			Start time		End time		Duration	Position	Type
	Year	Month	Day	Hour	Minute	Hour	Minute	[minute]	[deg]	
101	2012	4	7	12	19	12	29	10	1,60	CH
102	2012	4	24	12	35	12	48	13	1,81	QS
103	2012	4	24	13	25	13	36	11	3,97	QS
104	2012	5	1	12	14	12	31	17	1.74	CH
105	2012	5	1	12	39	12	52	13	5	CH
106	2012	5	1	12	39	12	53	14	4.39	QS
107	2012	5	7	12	5	12	23	18	4,89	CH
108	2012	5	7	12	9	12	26	17	5,11	CH
109	2012	5	15	12	5	12	24	19	1.37	QS
110	2012	5	15	13	5	13	18	13	1.96	QS
111	2012	5	24	13	34	13	49	15	0,98	QS
112	2012	6	1	12	7	12	24	17	1.65	CH
113	2012	6	1	12	20	12	34	14	4.49	CH
114	2012	6	1	12	42	12	53	11	4.43	QS
115	2012	6	7	13	25	13	42	17	5.18	CH
116	2012	6	15	12	33	12	53	20	5.06	CH
117	2012	6	15	12	37	12	49	12	0.65	QS
118	2012	6	15	12	52	13	9	17	1.45	CH
119	2012	6	24	13	13	13	24	11	4.66	CH
120	2012	7	15	12	10	12	29	19	4.77	CH
121	2012	8	1	12	28	12	41	13	4.39	CH
122	2012	8	1	12	57	13	13	16	5.27	CH
123	2012	8	1	13	28	13	48	20	4.59	CH
124	2012	8	7	12	8	12	20	12	4.86	CH
125	2012	8	7	12	14	12	29	15	0.89	QS
126	2012	8	24	12	0	12	12	12	1.63	QS
127	2012	9	1	12	3	12	19	16	1.79	QS
128	2012	9	1	13	7	13	25	18	4.97	CH
129	2012	9	7	12	0	12	12	12	4.67	CHB
130	2012	9	7	13	23	13	40	17	5.12	CH
131	2012	9	24	12	8	12	29	21	5.04	CH
132	2012	9	24	13	36	13	48	12	4.59	CH
133	2012	10	1	12	41	13	8	27	4.7	CH
134	2012	10	1	12	48	13	0	12	1.63	QS
135	2012	10	7	12	54	13	7	13	2.25	QS
136	2012	10	15	13	11	13	29	18	4.96	CH
137	2012	10	24	12	0	12	16	16	4.53	QS
138	2012	11	1	12	45	13	5	20	1.74	CH
139	2012	11	7	12	1	12	15	14	5.13	QS
140	2012	11	15	13	31	13	47	16	0.4	QS
141	2012	12	1	12	48	13	2	14	0.98	QS
142	2012	12	1	12	57	13	20	23	1.05	QS
143	2012	12	15	12	27	12	37	10	4.83	CHB
144	2013	1	7	12	8	12	19	11	2,19	CH
145	2013	1	15	12	33	12	48	15	5,96	QS
146	2013	1	15	13	29	13	51	22	5,04	CH
147	2013	1	15	13	44	13	59	15	5.25	CHB
148	2013	2	1	12	58	13	8	10	5.01	QS
149	2013	2	15	12	5	12	21	16	4.18	QS
150	2013	3	1	12	16	12	36	20	4.67	CH

#	Date of observation			Start time		End time		Duration [minute]	Position [deg]	Type
	Year	Month	Day	Hour	Minute	Hour	Minute			
151	2013	4	1	12	2	12	24	22	4.71	CH
152	2013	4	1	12	18	12	33	15	4.81	CH
153	2013	4	24	12	41	12	57	16	3.89	QS
154	2013	5	7	13	21	13	38	17	4.82	CH
155	2013	5	15	13	38	13	49	11	4.74	CHB
156	2013	5	24	12	39	12	52	13	4.69	CH
157	2013	6	1	13	37	13	52	15	4.68	CH
158	2013	6	15	12	28	12	48	20	4.19	QS
159	2013	6	15	12	55	13	19	24	2.44	CH
160	2013	7	1	12	42	12	59	17	4.73	CH
161	2013	7	7	12	11	12	27	16	5.03	QS
162	2013	7	15	13	10	13	28	18	5.37	QS
163	2013	8	1	13	12	13	24	12	4.71	CH
164	2013	8	7	12	5	12	21	16	5.8	QS
165	2013	8	7	12	38	12	47	9	4.89	CH
166	2013	8	15	12	21	12	49	28	1.12	QS
167	2013	8	24	13	3	13	13	10	4.82	CH
168	2013	9	7	12	8	12	25	17	5.08	CH
169	2013	9	7	12	51	13	12	21	1.98	QS
170	2013	9	15	13	21	13	33	12	4.23	CH
171	2013	10	1	12	35	12	49	14	1.41	QS
172	2013	10	7	12	5	12	25	20	4.08	QS
173	2013	10	7	12	54	13	6	12	4.79	CH
174	2013	10	15	12	47	13	10	23	3.46	QS
175	2013	11	7	12	16	12	33	17	3.19	QS
176	2013	11	7	12	26	12	50	24	4.17	QS
177	2013	11	7	12	29	12	42	13	2.35	CH
178	2013	11	7	12	32	12	50	18	0.53	QS
179	2013	11	15	12	21	12	32	11	4.36	QS
180	2013	11	15	12	55	13	10	15	0.92	QS
181	2013	11	24	13	5	13	17	12	5.44	QS
182	2013	11	24	13	11	13	22	11	4.7	CH
183	2013	12	1	12	26	12	44	18	0.64	CHB
184	2013	12	1	12	31	12	43	12	1.88	QS
185	2013	12	1	13	39	13	54	15	4.23	QS
186	2013	12	7	12	22	12	38	16	5.07	QS
187	2013	12	7	13	40	13	54	14	2.36	QS
188	2013	12	15	12	54	13	12	18	2.94	QS
189	2013	12	15	13	3	13	24	21	4.17	QS
190	2013	12	15	13	2	13	14	12	4.21	QS
191	2013	12	15	13	22	13	36	14	4.84	CH
192	2014	1	1	13	36	13	58	22	5	CH
193	2014	1	7	13	2	13	24	22	4.07	CH
194	2014	1	15	12	11	12	29	18	2.21	QS
195	2014	2	7	12	18	12	32	14	2.51	QS
196	2014	2	7	12	43	13	0	17	4.37	QS
197	2014	2	7	13	8	13	22	14	4.25	CH
198	2014	2	24	13	25	13	40	15	1.07	QS
199	2014	3	1	12	35	12	46	11	5.38	CH
200	2014	3	1	13	6	13	20	14	5.32	CH

#	Date of observation			Start time		End time		Duration	Position	Type
	Year	Month	Day	Hour	Minute	Hour	Minute	[minute]	[deg]	
201	2014	3	1	13	8	13	26	18	2.42	QS
202	2014	3	7	12	51	13	6	15	4.47	CH
203	2014	3	7	13	15	13	31	16	5.22	QS
204	2014	3	15	12	40	12	50	10	4.92	QS
205	2014	3	15	12	56	13	12	16	4.84	QS
206	2014	3	24	13	14	13	28	14	1.95	QS
207	2014	4	1	12	10	12	20	10	2.43	QS
208	2014	4	7	12	10	12	18	8	4.88	QS
209	2014	4	24	12	20	12	56	36	4.35	CH
210	2014	5	1	13	20	13	30	10	1.46	QS
211	2014	5	1	13	35	13	47	12	4.3	CHB
212	2014	5	15	13	23	13	39	16	0.05	QS
213	2014	5	15	12	31	12	38	7	5.55	CH
214	2014	5	24	13	0	13	21	21	3.79	QS
215	2014	6	1	12	49	13	9	20	1.42	QS
216	2014	6	7	12	18	12	39	21	5.6	CH
217	2014	6	7	12	47	13	8	21	5.61	CH
218	2014	6	15	12	45	13	0	15	0.98	QS
219	2014	6	24	13	15	13	32	17	3.84	QS
220	2014	6	24	13	17	13	33	16	2.24	QS
221	2014	7	7	12	20	12	36	16	4.78	QS
222	2014	7	7	13	39	13	58	19	4.31	CH
223	2014	7	15	12	1	12	16	15	5.46	CH
224	2014	7	15	12	8	12	30	22	2.03	QS
225	2014	7	24	12	13	12	33	20	5.36	CH
226	2014	8	1	12	30	12	41	11	4.23	CH
227	2014	8	1	12	50	13	5	15	5.43	CH
228	2014	8	7	12	5	12	23	18	3.81	CHB
229	2014	8	15	12	1	12	17	16	1.45	QS
230	2014	8	15	12	25	12	47	22	1.5	QS
231	2014	8	15	13	15	13	37	22	5.42	CH
232	2014	8	24	12	26	12	43	17	4.75	QS
233	2014	8	24	12	56	13	22	26	4.75	QS
234	2014	8	24	13	22	13	38	16	4.51	QS
235	2014	9	1	12	23	12	39	16	4.55	CH
236	2014	9	1	12	32	13	8	36	1.44	QS
237	2014	9	7	13	6	13	20	14	4.24	CH
238	2014	9	7	13	21	13	34	13	5.67	QS
239	2014	9	7	13	41	13	59	18	0.56	QS
240	2014	9	15	12	40	12	54	14	2.24	QS
241	2014	9	15	13	18	13	36	18	2.23	QS
242	2014	9	24	12	40	12	59	19	5.26	QS
243	2014	10	1	12	28	12	49	21	3.91	QS
244	2014	10	1	12	52	13	5	13	4.07	CH
245	2014	10	7	12	32	12	54	22	5.53	CH
246	2014	10	24	12	0	12	17	17	0.95	QS
247	2014	11	1	12	17	12	39	22	1.9	QS
248	2014	11	15	13	21	13	32	11	5.76	CH
249	2014	12	1	12	58	13	12	14	5.41	CH
250	2014	12	1	13	37	13	53	16	5.2	CH

#	Date of observation			Start time		End time		Duration [minute]	Position [deg]	Type
	Year	Month	Day	Hour	Minute	Hour	Minute			
251	2014	12	7	12	9	12	29	20	1.01	QS
252	2014	12	7	13	4	13	17	13	2.42	QS
253	2014	12	15	12	1	12	14	13	4.46	CH
254	2014	12	15	12	37	12	51	14	4.46	CH
255	2014	12	15	13	4	13	20	16	4.46	CH
256	2014	12	24	13	8	13	26	18	4.3	CH
257	2015	1	7	12	18	12	34	16	5.43	CH
258	2015	1	7	12	30	12	51	21	4.59	QS
259	2015	1	15	12	8	12	20	12	4.63	CH
260	2015	1	24	13	30	13	45	15	4.59	CH
261	2015	2	15	12	47	13	15	28	5.03	QS
262	2015	2	24	12	56	13	12	16	4.91	QS
263	2015	2	24	13	19	13	42	23	4.63	CH
264	2015	3	1	12	0	12	14	14	4.78	CH
265	2015	3	1	12	20	12	40	20	4.78	CH
266	2015	3	7	13	37	13	47	10	5.3	CH
267	2015	4	7	13	16	13	31	15	0.96	QS
268	2015	4	24	12	14	12	27	13	5.09	CH
269	2015	5	1	13	5	13	22	17	4.53	CH
270	2015	5	1	13	7	13	29	22	4.6	CH
271	2015	6	15	13	34	13	55	21	5.41	QS
272	2015	6	24	13	8	13	29	21	2.24	QS
273	2015	7	1	12	8	12	22	14	5.26	QS
274	2015	7	1	12	37	12	55	18	1	CH
275	2015	7	15	13	29	13	50	21	2.22	QS
276	2015	8	1	12	25	12	42	17	1.73	QS
277	2015	8	1	12	48	13	5	17	4.6	CH
278	2015	8	15	12	59	13	25	26	2.08	CH
279	2015	8	24	12	15	12	38	23	4.64	CH
280	2015	8	24	13	28	13	41	13	4.53	CH
281	2015	9	1	12	3	12	21	18	4.41	CH
282	2015	9	1	12	41	12	58	17	4.63	CH
283	2015	9	1	13	11	13	26	15	4.78	CH
284	2015	9	7	12	4	12	29	25	5.27	QS
285	2015	9	7	13	16	13	33	17	2.2	QS
286	2015	10	1	12	23	12	42	19	4.59	CH
287	2015	10	1	12	43	12	55	12	2.07	CH
288	2015	10	1	12	48	13	8	20	2.58	QS
289	2015	10	1	13	29	13	44	15	3.97	QS
290	2015	10	7	12	53	13	16	23	4.96	CH
291	2015	11	1	12	7	12	21	14	2.09	QS
292	2015	11	1	12	32	12	46	14	5.1	CH
293	2015	11	7	12	0	12	16	16	1	CH
294	2015	11	15	12	6	12	29	23	4.49	CH
295	2015	11	24	12	23	12	40	17	4.62	CH
296	2015	12	1	13	6	13	20	14	0.97	QS
297	2015	12	1	13	13	13	29	16	4.67	CH
298	2015	12	15	12	45	13	4	19	5	CH
299	2016	1	1	12	0	12	16	16	1.88	QS
300	2016	1	15	12	36	12	55	19	1.46	QS

#	Date of observation			Start time		End time		Duration	Position	Type
	Year	Month	Day	Hour	Minute	Hour	Minute	[minute]	[deg]	
301	2016	1	15	13	17	13	34	17	1.34	QS
302	2016	1	24	12	26	12	42	16	1.7	CH
303	2016	1	24	13	13	13	29	16	2.02	CH
304	2016	2	1	12	9	12	27	18	2.71	QS
305	2016	2	7	12	5	12	21	16	4.39	QS
306	2016	2	7	12	17	12	32	15	1.74	QS
307	2016	2	15	12	53	13	14	21	4.27	QS
308	2016	2	24	13	0	13	19	19	5.01	CH
309	2016	3	1	13	21	13	42	21	4.23	QS
310	2016	3	1	13	28	13	48	20	1.23	CH
311	2016	3	7	12	9	12	28	19	5.05	CH
312	2016	3	7	13	7	13	24	17	4.87	CH
313	2016	3	15	13	27	13	48	21	4.48	CH
314	2016	3	24	13	19	13	38	19	3.7	QS
315	2016	4	15	12	47	13	4	17	4.7	CH
316	2016	4	24	13	16	13	35	19	2.11	QS
317	2016	5	1	12	2	12	25	23	1.97	CH
318	2016	5	15	13	0	13	20	20	4.34	QS
319	2016	5	24	13	15	13	28	13	0.42	QS
320	2016	6	1	12	2	12	15	13	1.52	CH
321	2016	6	1	12	32	12	46	14	1.53	CH
322	2016	6	15	12	39	12	57	18	0.9	QS
323	2016	7	1	12	3	12	19	16	1.73	CH
324	2016	7	15	13	16	13	36	20	0.74	QS
325	2016	8	1	12	0	12	15	15	2.88	QS
326	2016	8	1	12	0	12	19	19	1.67	CH
327	2016	8	15	12	4	12	20	16	4.56	CH
328	2016	9	1	13	35	13	59	24	1.05	QS
329	2016	9	15	13	18	13	38	20	4.57	CH
330	2016	10	7	12	35	12	52	17	4.67	CH
331	2016	10	15	12	53	13	13	20	0.83	QS
332	2016	10	24	12	7	12	28	21	4.4	QS
333	2016	11	7	12	46	13	5	19	1.79	CH
334	2016	11	15	12	0	12	12	12	1.33	CH
335	2016	11	15	12	35	12	56	21	2.64	QS
336	2016	11	24	12	35	12	52	17	1.51	CH
337	2016	12	1	12	34	12	52	18	5.01	CH
338	2016	12	1	13	34	13	57	23	5.09	CH
339	2016	12	24	13	11	13	27	16	4.76	CH
340	2017	1	1	13	20	13	48	28	4.82	CH
341	2017	1	15	13	25	13	43	18	5.27	QS
342	2017	1	24	13	12	13	31	19	5.25	QS
343	2017	2	1	12	36	13	2	26	5.25	QS
344	2017	2	7	12	45	13	3	18	3.14	QS
345	2017	3	1	12	20	12	54	34	2.14	QS
346	2017	3	1	13	35	13	59	24	2.14	QS
347	2017	3	7	13	25	13	40	15	4.63	CH
348	2017	4	1	13	22	13	47	25	1.41	CH
349	2017	4	15	12	0	12	19	19	4.6	CH
350	2017	4	24	12	46	13	13	27	1.42	CH

#	Date of observation			Start time		End time		Duration	Position	Type
	Year	Month	Day	Hour	Minute	Hour	Minute	[minute]	[deg]	
351	2017	5	7	12	18	12	32	14	4.48	CH
352	2017	5	15	12	24	12	48	24	0.16	QS
353	2017	5	15	12	36	12	55	19	2.08	QS
354	2017	5	24	13	13	13	33	20	2.1	QS
355	2017	6	1	13	17	13	37	20	1.89	CH
356	2017	6	7	13	33	13	54	21	1.58	CH

Bibliography

Akioka, M., Kubota, J., Ichimoto, K., Tohmura, I., & Suzuki, M. 1987, *Sol. Phys.*, 112, 313

Alexander, D., & Acton, L. W. 2002, The active Sun, ed. J. A. Bleeker, J. Geiss, & M. C. E. Huber (Kluwer Academic Publishers), 1089

Anderson, J. D. 2011, Fundamentals of Aerodynamics, 5th ed., McGraw–Hill, New York, 338

Andretta, V., & Jones, H. P. 1997, *The Astrophys. Jour.*, 489, 375

Andretta, V., Telloni, D., & Del Zanna, G. 2012, *Sol. Phys.*, 279, 53

Aschwanden, M. J. 2004, Physics of the Solar Corona. An Introduction (Praxis Publishing Ltd)

Aschwanden, M. J., Nightingale, R. W., & Alexander, D. 2000, *The Astrophys. Jour.*, 541, 1059

Avrett, E. H., & Loeser, R. 2008, *The Astrophys. Jour. Supp. Ser.*, 175, 229

Babcock, H. D. 1959, *The Astrophys. Jour.*, 130, 364

Babcock, H. D., & Livingston, W. C. 1958, Science, 127, 1058

Bailey, K. D. 1994, Typologies and Taxonomies, 34

Banerjee, D., O'Shea, E., & Doyle, J. G. 2000, *Astr. and Astrophy.*, 355, 1152

Beckers, J. M. 1972, *Ann. Revw. Astr. Astrphy.*, 10, 73

Benacka, J. 2010, American Journal of Physics, 78, 616. https://doi.org/10.1119/1.3298375

Benevolenskaya, E. E. 1998a, *The Astrophys. J. Lett.*, 509, L49

—. 1998b, *Sol. Phys.*, 181, 479

Bennett, S. M., & Erdélyi, R. 2015, *The Astrophys. Jour.*, 808, 135

Bohlin, J. D., Vogel, S. N., Purcell, J. D., et al. 1975, *The Astrophys. J. Lett.*, 197, L133

Bray, R. J., Cram, L. E., Durrant, C., & Loughhead, R. E. 1991, Plasma Loops in the Solar Corona, 522

Broomhall, A.-M., Chaplin, W. J., Elsworth, Y., Fletcher, S. T., & New, R. 2009, *The Astrophys. J. Lett.*, 700, L162

Broomhall, A.-M., & Nakariakov, V. M. 2015, *Sol. Phys.*, 290, 3095

Centeno, R., Trujillo Bueno, J., Uitenbroek, H., & Collados, M. 2008, *The Astrophys. Jour.*, 677, 742

Chae, J., Wang, H., Lee, C.-Y., Goode, P. R., & Schühle, U. 1998, *The Astrophys. J. Lett.*, 497, L109

Chandra, R., Gupta, G. R., Mulay, S., & Tripathi, D. 2015, *Month. Not. Roy. Ast. Soc.*, 446, 3741

Chaplin, W. C., Elsworth, Y., Isaak, G. R., et al. 1996, The Observatory, 116, 32

Charbonneau, P. 2010, Living Reviews in Solar Physics, 7, 3

Chowdhury, P., Choudhary, D. P., & Gosain, S. 2013, *The Astrophys. Jour.*, 768, 188

Clette, F., Svalgaard, L., Vaquero, J. M., & Cliver, E. W. 2015, Revisiting the Sunspot Number, ed. A. Balogh, H. Hudson, K. Petrovay, & R. von Steiger, 35

Colino, J. M., & Barbero, , A. J. 2013, European Journal of Physics, 34, 188

Cranmer, S. R. 2009, Living Reviews in Solar Physics, 6, 3

Crowl, E. L., & Kunio, S. 1988, Lognormal distributions : theory and applications, 387

Culhane, L., Harra, L. K., Baker, D., et al. 2007, *Pub. Astr. Soc. Japan*, 59, S751

Daubechies, I. 1990, *IEEE Trans. o. Inf. Theo.*, 36, doi:10.1109/18.57199

De Pontieu, B., Erdélyi, R., & James, S. P. 2004, *Nature*, 430, 536

de Pontieu, B., McIntosh, S., Hansteen, V. H., et al. 2007, *Pub. Astr. Soc. Japan*, 59, S655

Deforest, C. E., Hoeksema, J. T., Gurman, J. B., et al. 1997, *Sol. Phys.*, 175, 393

Delaboudinière, J.-P., Artzner, G. E., Brunaud, J., et al. 1995, *Sol. Phys.*, 162, 291

Denker, C., Johannesson, A., Marquette, W., et al. 1999, *Sol. Phys.*, 184, 87

Dere, K. P., Bartoe, J.-D. F., Brueckner, G. E., et al. 1989, *Sol. Phys.*, 119, 55

Dikpati, M., Gilman, P. A., & de Toma, G. 2008, *The Astrophys. J. Lett.*, 673, L99

Doyle, J. G., van den Oord, G. H. J., O'Shea, E., & Banerjee, D. 1999, *Astr. and Astrophy.*, 347, 335

Eddy, J. A. 1977, in The Solar Output and its Variation, ed. O. R. White, 51

Elek, A., Gyenge, N., Korsós, M. B., & Erdélyi, R. 2018, in IAU Symposium, Vol. 335, Space Weather of the Heliosphere: Processes and Forecasts, ed. C. Foullon & O. E. Malandraki, 17–19

Feldman, U. 1998, *Spc. Sci. Revw.*, 85, 227

Feldman, U., & Widing, K. G. 2003, *Spc. Sci. Revw.*, 107, 665

Fletcher, S. T., Broomhall, A.-M., Salabert, D., et al. 2010, *The Astrophys. J. Lett.*, 718, L19

Foukal, P. V. 2004, Solar Astrophysics, 2nd, Revised Edition, 480

Gary, G. A. 2001, *Sol. Phys.*, 203, 71

Georgakilas, A. A., Koutchmy, S., & Alissandrakis, C. E. 1999, *Astr. and Astrophy.*, 341, 610

Golub, L., Deluca, E., Austin, G., et al. 2007, *Sol. Phys.*, 243, 63

Guerster, M., & Walter, U. 2017, PLOS ONE, 12, 1. https://doi.org/10.1371/journal.pone.0187798

Guillermier, P., & Koutchmy, S., eds. 1999, Total eclipses : science, observations, myths, and legends

Gyenge, N., Baranyi, T., & Ludmány, A. 2012, Central European Astrophysical Bulletin, 36, 9

—. 2014, *Sol. Phys.*, 289, 579

Gyenge, N., Bennett, S., & Erdélyi, R. 2015, Journal of Astrophysics and Astronomy, 36, 103

Győri, L., Ludmány, A., & Baranyi, T. 2017, *Month. Not. Roy. Ast. Soc.*, 465, 1259

Habbal, S. R., & Gonzalez, R. D. 1991, *The Astrophys. J. Lett.*, 376, L25

Hale, G. E. 1908, *The Astrophys. Jour.*, 28, 315

Hale, G. E., Ellerman, F., Nicholson, S. B., & Joy, A. H. 1919, *The Astrophys. Jour.*, 49, 153

Harrison, R. A., Sawyer, E. C., Carter, M. K., et al. 1995, *Sol. Phys.*, 162, 233

Harvey, J., Krieger, A. S., Timothy, A. F., & Vaiana, G. S. 1975, Osservazioni e memorie dell'Osservatorio astrofisico di Arcetri, 104, 50

Harvey, K. L., & Recely, F. 2002, *Sol. Phys.*, 211, 31

Hathaway, D. H. 2012, *The Astrophys. Jour.*, 760, 84

—. 2015, Living Reviews in Solar Physics, 12, 4

Hermans, L. M., & Martin, S. F. 1986, in NASA Conference Publication, Vol. 2442, NASA Conference Publication, ed. A. I. Poland

Howard, R. A., Moses, J. D., Vourlidas, A., et al. 2008, *Spc. Sci. Revw.*, 136, 67

Howe, R., Hill, F., Komm, R., et al. 2018, *The Astrophys. J. Lett.*, 862, L5

Huber, M. C. E., Foukal, P. V., Noyes, R. W., et al. 1974, *The Astrophys. J. Lett.*, 194, L115

Johannesson, A., & Zirin, H. 1996, *The Astrophys. Jour.*, 471, 510

Kaiser, M. L., Kucera, T. A., Davila, J. M., et al. 2008, *Spc. Sci. Revw.*, 136, 5

Kamio, S., Curdt, W., Teriaca, L., Inhester, B., & Solanki, S. K. 2010, *Astr. and Astrophy.*, 510, L1

Karovska, M., Blundell, S. F., & Habbal, S. R. 1994, *The Astrophys. Jour.*, 428, 854

Karovska, M., & Habbal, S. R. 1994, *The Astrophys. J. Lett.*, 431, L59

Kayshap, P., Srivastava, A. K., & Murawski, K. 2013a, *The Astrophys. Jour.*, 763, 24

Kayshap, P., Srivastava, A. K., Murawski, K., & Tripathi, D. 2013b, *The Astrophys. J. Lett.*, 770, L3

Kiss, T. S., & Erdélyi, R. 2018, *The Astrophys. Jour.*, 857, 113

Kiss, T. S., Gyenge, N., & Erdélyi, R. 2017, *The Astrophys. Jour.*, 835, 47

—. 2018, Advances in Space Research, 61, 611

Kitchatinov, L. L., & Khlystova, A. I. 2014, Astronomy Letters, 40, 663

Kjeldseth Moe, O., Engvold, O. O., & Beckers, J. M. 1975, *Sol. Phys.*, 40, 65

Koutchmy, O., Koutchmy, S., Nitschelm, C., Sykora, J., & Smartt, R. N. 1988, in Solar and Stellar Coronal Structure and Dynamics, ed. R. C. Altrock, 256–266

Krivova, N. A., Balmaceda, L., & Solanki, S. K. 2007, *Astr. and Astrophy.*, 467, 335

Krueger, A. 1979, Introduction to solar radio astronomy and radio physics

Kudoh, T., & Shibata, K. 1997, in ESA Special Publication, Vol. 404, Fifth SOHO Workshop: The Corona and Solar Wind Near Minimum Activity, ed. A. Wilson, 477

Kundu, M. R. 1965, Solar radio astronomy

Kuzin, S. V., Zhitnik, I. A., Shestov, S. V., et al. 2011, Solar System Research, 45, 162

Labonte, B. J. 1979, *Sol. Phys.*, 61, 283

Lee, D., & Deane, A. E. 2009, Journal of Computational Physics, 228, 952

Lemen, J. R., Title, A. M., Akin, D. J., et al. 2012, *Sol. Phys.*, 275, 17

Levine, R. H. 1982, *Sol. Phys.*, 79, 203

Loboda, I. P., & Bogachev, S. A. 2017, *Astr. and Astrophy.*, 597, A78

—. 2019, *The Astrophys. Jour.*, 871, 230

Loucif, M. L. 1994, *Astr. and Astrophy.*, 281, 95

Madjarska, M. S., Vanninathan, K., & Doyle, J. G. 2011, *Astr. and Astrophy.*, 532, L1

Maunder, E. W. 1903, The Observatory, 26, 329

—. 1904, *Month. Not. Roy. Ast. Soc.*, 64, 747

McGill, R., Tukey, J. W., & Larsen, W. A. 1978, The American Statistician, 32, 12. http://www.jstor.org/stable/2683468

McKinnon, J. A., & Waldmeier, M. 1987, Sunspot numbers, 1610-1985 : based on "The sunspot activity in the years 1610-1960"

Mohazzabi, P., & Shea, J. H. 1996, American Journal of Physics, 64, 1242

Moore, R. L., Tang, F., Bohlin, J. D., & Golub, L. 1977, *The Astrophys. Jour.*, 218, 286

Murawski, K., Srivastava, A. K., & Zaqarashvili, T. V. 2011, *Astr. and Astrophy.*, 535, A58

Newkirk, Jr., G., & Harvey, J. 1968, *Sol. Phys.*, 3, 321

Ofman, L., Nakariakov, V. M., & DeForest, C. E. 1999, *The Astrophys. Jour.*, 514, 441

Parenti, S., Bromage, B. J. I., & Bromage, G. E. 2002, *Astr. and Astrophy.*, 384, 303

Pedregosa, F., Varoquaux, G., Gramfort, A., et al. 2011, Journal of Machine Learning Research, 12, 2825

Penza, V., Pietropaolo, E., & Livingston, W. 2006, *Astr. and Astrophy.*, 454, 349

Pesnell, W. D., Thompson, B. J., & Chamberlin, P. C. 2012, *Sol. Phys.*, 275, 3

Pike, C. D., & Harrison, R. A. 1997, *Sol. Phys.*, 175, 457

Pike, C. D., & Mason, H. E. 1998, *Sol. Phys.*, 182, 333

Ramsey, H. E., Martin, S. F., & Harvey, K. L. 1975, in *Bull. o. t. Amer. Astr. Soc.*, Vol. 7, Bulletin of the American Astronomical Society, 424

Rosner, R., Tucker, W. H., & Vaiana, G. S. 1978, *The Astrophys. Jour.*, 220, 643

Saito, K. 1958, *Pub. Astr. Soc. Japan*, 10, 49

Scherrer, P. H., Bogart, R. S., Bush, R. I., et al. 1995, *Sol. Phys.*, 162, 129

Schwabe, H. 2004, in Some Aspects of the Earlier History of Solar-Terrestrial Physics, ed. W. Schröder, 124

Scullion, E., Doyle, J. G., & Erdélyi, R. 2010, *Mem. d. Soci. Astr. It.*, 81, 737

Shibata, K. 1982, *Sol. Phys.*, 81, 9

Shibata, K. 1997, in ESA Special Publication, Vol. 404, Fifth SOHO Workshop: The Corona and Solar Wind Near Minimum Activity, ed. A. Wilson, 103

Shibata, K., & Uchida, Y. 1986, *Sol. Phys.*, 103, 299

Shibata, K., Ishido, Y., Acton, L. W., et al. 1992, *Pub. Astr. Soc. Japan*, 44, L173

Sterling, A. C., Moore, R. L., Falconer, D. A., et al. 2016, *The Astrophys. Jour.*, 821, 100

SunPy Community, T., Mumford, S. J., Christe, S., et al. 2015, Computational Science and Discovery, 8, 014009

Tapping, K. F. 1987, *J. Geophys. Res.*, 92, 829

Thompson, W. T., & Brekke, P. 2000, *Sol. Phys.*, 195, 45

Timmerman, P., & van der Weele, J. 1999, American Journal of Physics, 1999, 538

Torrence, C., & Compo, G. P. 1998, *Bull. o. t. Amer. Met. Soc.*, 79, 61

Tousey, R. 1972, in Space Research Conference, Vol. 2, Space Research Conference, ed. S. A. Bowhill, L. D. Jaffe, & M. J. Rycroft, 1719–1737

Tousey, R., Bartoe, J. D. F., Bohlin, J. D., et al. 1973, *Sol. Phys.*, 33, 265

Tsuneta, S., Ichimoto, K., Katsukawa, Y., et al. 2008a, *The Astrophys. Jour.*, 688, 1374

—. 2008b, *Sol. Phys.*, 249, 167

Vernazza, J. E., Avrett, E. H., & Loeser, R. 1981, *The Astrophys. Jour. Supp. Ser.*, 45, 635

Waldmeier, M. 1935, Astronomische Mitteilungen der Eidgenössischen Sternwarte Zurich, 14, 105

—. 1939, Astronomische Mitteilungen der Eidgenössischen Sternwarte Zurich, 14, 470

—. 1961, The sunspot-activity in the years 1610-1960

Wang, H. 1998, *The Astrophys. Jour.*, 509, 461

Wang, J., Li, W., Denker, C., et al. 2000, *The Astrophys. Jour.*, 530, 1071

Wedemeyer-Böhm, S., Lagg, A., & Nordlund, Å. 2009, *Spc. Sci. Revw.*, 144, 317

Wilhelm, K., Curdt, W., Marsch, E., et al. 1995, *Sol. Phys.*, 162, 189

Willis, D. M., Wild, M. N., Appleby, G. M., & Macdonald, L. T. 2016, *Sol. Phys.*, 291, 2553

Wilson, R. M. 1987, *J. Geophys. Res.*, 92, 10

Withbroe, G. L., & Noyes, R. W. 1977, *Ann. Revw. Astr. Astrphy.*, 15, 363

Withbroe, G. L., Jaffe, D. T., Foukal, P. V., et al. 1976, *The Astrophys. Jour.*, 203, 528

Wolf, R. 1850, Astronomische Mitteilungen der Eidgenössischen Sternwarte Zurich, 1, 3

Worden, J. R., White, O. R., & Woods, T. N. 1998, *The Astrophys. Jour.*, 496, 998

Wuelser, J.-P., Lemen, J. R., Tarbell, T. D., et al. 2004, in *Proc. SPIE*, Vol. 5171, Telescopes and Instrumentation for Solar Astrophysics, ed. S. Fineschi & M. A. Gummin, 111–122

Xia, L. D., Popescu, M. D., Doyle, J. G., & Giannikakis, J. 2005, *Astr. and Astrophy.*, 438, 1115

Yamauchi, Y., Moore, R. L., Suess, S. T., Wang, H., & Sakurai, T. 2004, *The Astrophys. Jour.*, 605, 511

Yokoyama, T., & Shibata, K. 1995, *Nature*, 375, 42

—. 1996, *Pub. Astr. Soc. Japan*, 48, 353

Young, P. R., Klimchuk, J. A., & Mason, H. E. 1999, *Astr. and Astrophy.*, 350, 286

Zaqarashvili, T. V., Carbonell, M., Oliver, R., & Ballester, J. L. 2010, *The Astrophys. J. Lett.*, 724, L95

Zirin, H. 1975, *The Astrophys. J. Lett.*, 199, L63